2002 SUMMER HILL GRAVITY SURVEY

FINAL REPORT

PART B : PROCESSING / INTERPRETATION

PEL 57, OTWAY BASIN, SOUTH AUSTRALIA

Origin Energy Resources Limited
ABN 66 007 845 338
John Oxley Centre, 339 Coronation Drive
MILTON QLD 4064

December 2003

TABLE OF CONTENTS

1 INTRODUCTION

This report covers the processing and initial interpretation of the Summer Hill Gravity Survey data which was acquired in PEL 57 (South Australia) and neighbouring PEP 151 (Victoria) in two phases during 2002 (**Figure 1**).

Phase 1 of the survey was conducted in May 2002 within PEL 57. Phase 2, located within PEL 57 and PEP 151 was recorded during October-November 2002 and had been necessitated by delays with the granting of Exploration Licence PEP 151 to Essential Petroleum Resources (Operator).

Stewart Geophysical Consultants P/L carried out the processing and interpretation of the Summer Hill gravity data.

2 SURVEY OBJECTIVES

The Summer Hill Gravity Survey was designed to provide high resolution gravity information over a Waarre Sandstone play located in the southern part of PEL 57 (South Australia) with possible extension into the western portion of PEP 151 (Victoria).

Previously recorded seismic data identified a potentially significant structure at the Waarre Sandstone level. Regional gravity data highlights the Summer Hill Lead as a significant gravity anomaly, and this survey was aimed to provide confirmation of structural closure and to identify the approximate location of the crest of the structure.

3 SURVEY LOCATION

The survey grid straddles the South Australian-Victorian border and is located approximately 27 km southeast of Mt Gambier. The coastline provided the southern limit to the survey. A small portion of the grid extended into the Lower Glenelg National Park.

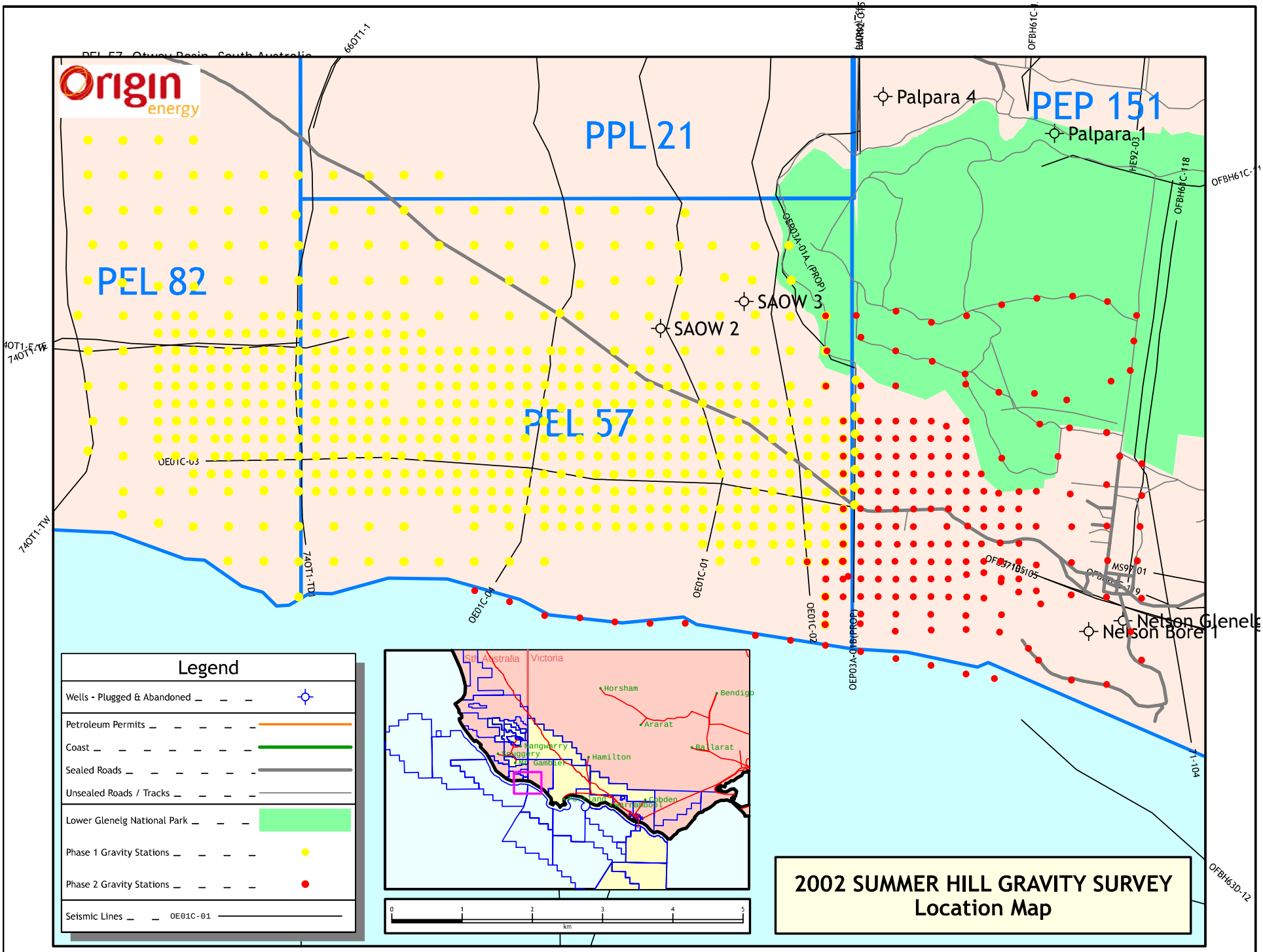

Figure 1 – 2002 Summer Hill Gravity Survey Location Map

Greenfields:\PEL57\OT057 - O Operations\2002 Summerhill Gravity\Summerhill Gravity Processing Interp – Final Report.doc

4 DATA PROCESSING / INTERPRETATION

Data processing and interpretation of the Summer Hill Gravity Survey data was carried out at the end of each phase of acquisition and incorporated all pre-existing regional gravity data. This work is detailed in **Appendix 1** and **2**.

Key results from the processing and interpretation are :

- The 2002 Summer Hill Gravity Survey has defined a relatively strong gravity anomaly associated with the Summer Hill prospect in PEL 57.

- The gravity data suggests that the majority of the Summer Hill structure lies within PEL 57 and extends up to about 1 km into neighbouring PEP 151.

- As well as identifying the Summer Hill prospect, the gravity data has also enabled possible structural features to be inferred in the area. For example, the dataset shows several lineations in a roughly northwesterly orientation which intersect the anomaly and may be representative of deeper structure or faulting.

- A tentative analysis of the magnetic depths indicates that basement depths away from the prospect may reach 6 km, although magnetic basement is probably somewhat shallower (3.5 to 4 km) in the vicinity of the structure.

- More detailed interpretation of the gravity involving complex forward modelling may be carried out, utilising information from the existing seismic data where possible to constrain solutions. Conversely, the existing seismic should be reinterpreted with a view to incorporating structural trends identified from the gravity data.

5 CONCLUSIONS

The 2002 Summer Hill Gravity Survey successfully provided high resolution gravity data over the Summer Hill Waarre Sandstone lead which is now characterised as a relatively significant gravity anomaly. The data indicates that the majority of the lead as well as the interpreted structural crest lies within PEL 57, with minor extension of the structure into neighbouring PEP 151.

APPENDIX 1

PROCESSING CONTRACTORS REPORT (PHASE 1)

Stewart Geophysical Consultants P/L

Potential Field and Radiometric data over the Summer Hill Prospect, southeast South Australia

prepared for

Origin Energy Resources Ltd.
GPO Box 148
Brisbane
Queensland 4001

by

Stewart Geophysical Consultants Pty. Ltd.
44 Harrow Road
College Park
South Australia 5069
Australia
Phone/Fax: 61-8-8363 3635
Email: stewgeop@senet.com.au

May 2002

Contents

List of Figures

Potential field and radiometric data over the Summer Hill prospect, southeast South Australia

Scope of the report

The main aim of this analysis is to merge the new terrain-corrected gravity survey with existing data, including processing to define local variations which may be of interest in structural interpretation. In addition, available airborne magnetic and radiometric data have been reviewed to provide additional information on regional and local trends. Some enhanced grids were derived in order to highlight features which may be of structural significance. The analysis has also involved a preliminary investigation of basement structure using automatic depth estimation methods applied to the magnetic data. It is not intended to provide a comprehensive interpretation of this region which would require a considerable amount of additional information, especially if techniques such as forward modelling were to be employed.

Introduction

There is only a limited amount of seismic information available for the area of the prospect, but the existing gravity data, although fairly sparse, indicate that the structure is associated with a well-defined gravity anomaly. Hence a new gravity survey has been conducted to provide more detail, and these data have had terrain corrections applied here and have been merged with the previous data to provide an improved data set for analysis. Several derivative products have also been generated showing additional features that can be correlated with structure.

Complete magnetic and radiometric coverage exists for the region, including part of the offshore area, from data sets available from the South Australian and Victorian databases. These have also been processed and merged, and then used to enhance features which may assist in exploration of the prospect. This includes near surface effects which could be associated with hydrocarbons, delineation of fault trends, as well as an attempt to define the pattern of magnetic basement depths. Radiometric data can reveal detailed variations in the surface geology, and may also enable boundaries such as faults to be located more accurately. In addition, radiometric anomalies are sometimes associated with the presence of hydrocarbons. Hence the radiometric data which were acquired with the airborne magnetics have also been processed and merged, and have been used to generate images which highlight changes in the surface lithology. Radiometric ratio images have also been generated to determine whether any anomalies are associated with the prospect.

The UTM coordinates used for all the mapping here are given as AMG zone 54 values, as the existing data sets are generally based on this datum. All gravity values are in milligals. Most of the maps are presented as colour bitmaps, where the size of the text is related to the pixel or grid cell size. The UTM coordinate ticks are mainly at 5 or 10 km intervals, and the location of any pixel can be found readily on the screen by using the cursor to count the numbers of pixels from a plotted coordinate mark. Where shading has

been used for the coloured diagrams the illumination is from the northeast for most of the images, while monochrome plots do not have shading. Generally the detail and colour contrasts are better when viewed on the screen than on the paper prints given in this report, and hence the bitmap image files are included as digital products with this report.

Gravity data

The regional distribution of the existing gravity data from the AGSO, South Australian and Victorian databases is shown in Figure 1, which includes 5357 stations. Data were used from all these sources in order to include as many stations as possible, and some adjustments were carried out to reduce the more obvious misties in the values. Duplicate points were deleted when the data were merged, and a 200 m grid of the Bouguer gravity for the area is given in Figure 2. The station distribution around the prospect area is shown in more detail in Figure 3, which contains 1145 points, and the corresponding 100 m gravity grid is plotted in Figure 4. The horizontal gradients computed with anisotropic operators 1 km and 2 km wide are shown in Figures 5 and 6 respectively. The residual obtained with a 2 dimensional Hamming operator 10 km wide is given in Figure 7. There are still some traces of local misties in the data, which is quite common where different gravity surveys or data traverses overlap, but these can be rather difficult to eliminate completely.

Despite the fairly sparse coverage in places some trends and local maxima can be seen in these derivative plots. No colour scales are given on the derivative plots since non-linear scales are employed for optimum colour stretch, but high values are towards the red end of the spectrum. Maxima in the gradient tend to coincide with lateral changes in density, such as may occur at faults or contacts, while local residual maxima may correspond to structural highs. The Bouguer gravity for a small area 8 by 17 km around the prospect is shown in Figure 8, which also includes the station locations. The residual and horizontal gradient for this area are given in Figures 9 and 10. These plots suggest that a local gravity maximum is associated with the prospect, which is also bounded near its northern margin by a prominent gradient trend (a fault). However, these features are obviously poorly defined by the existing distribution of gravity stations, which are completely lacking for about 3 km to the east of the State boundary.

The new gravity survey covers an area from approximately 485000 to 497000 m E, and 5788000 to 5795000 m N, in the extreme southeastern corner of South Australia. Although the prospect possibly extends for several kilometres into Victoria, gravity data have not yet been obtained there. The stations were nominally on a 500 by 500 m grid, with part of the area on a smaller 250 by 250 m spacing. A total of 557 stations were acquired, of which one (a base station) was about 25 km to the northwest of the actual survey area. Hence this point (Line 0, Station 9191) was not used for mapping, although it is included in the data set. The locations of the remaining 556 stations are plotted in Figure 11.

Terrain corrections were applied to the gravity survey, since even small corrections of a few tenths of a milligal or less may be significant when the anomalies being studied are only of the order of one or two milligals. A digital terrain model (DTM) was generated using data from the two airborne surveys described further on in the section on the magnetic data. The line or profile data were levelled and the 50 m grids were then

merged to produce regional DTM grid. Due to the survey datum employed, the grid was shifted so that the mean height of the DTM over the marine area was set at zero, and the resulting grid is shown in Figure 12. The volcanic area around Mt. Gambier towards the northwest of Figure 12 is not defined properly, as the radar and barometric altimeter values are not consistent in this region, and there are also offsets along the join of the two data sets. Errors probably occur elsewhere within the South Australian data set, since this DTM used barometric rather than GPS altitude as a reference. The Victorian part of the DTM used GPS heights as a reference and should be more reliable. The DTM for a more localised area is shown in Figure 13, which also includes the locations of the 4 seismic lines over the prospect. It can be seen that while the topography near the prospect is fairly subdued there are several features which could affect the gravity values. The expected gravity terrain corrections were estimated at 100 m intervals across this grid for a density of 2.3 gm cm^{-3} and are shown in Figure 14. The largest terrain corrections, up to about 0.4 milligal occur along the river near the State border, due to the steep topography in that area, but otherwise tend to be much smaller in the region of the present gravity survey.

While many of the new gravity station elevations were within a few metres of the DTM heights, in some places the DTM was more than 10 m lower than the gravity heights, due to inaccuracies in the South Australian airborne data. This would lead to significant and quite erroneous terrain corrections for the gravity if only the original merged DTM grid were to be used for the corrections. Hence the heights from the new gravity stations were used to create a more reliable elevation grid in the survey area, and this was then merged with the regional grid, as shown in Figure 15 (cf. Figure 13). The terrain corrections were then calculated exactly at each of the new station locations and used to give a final corrected Bouguer value for merging and gridding. Generally the corrections were only a few hundredths of a milligal, with a maximum of about 0.1 milligal, as expected from Figure 14.

A density of 2.67 gm cm^{-3} was used for the initial Bouguer reduction of the gravity data. While this density is often employed for routine gravity work, it is more appropriate to use a lower value in sedimentary environments. Hence gravity data sets, including terrain corrections, and plots were also generated for Bouguer densities of 2.40, 2.00 and 1.70 gm cm^{-3}. These would correspond to a typical sedimentary rock, poorly consolidated or weathered sediments, and unconsolidated material such as sand. The terrain-corrected Bouguer values were gridded at a 50 m interval using minimum curvature routines, and are plotted in Figures 16 through 19, which include the grid for a density of 2.67 gm cm^{-3}. Although there are no large variations in the topography, a change in the Bouguer density has a noticeable effect on the patterns observed in the gravity plot. There are significant lineations in the gravity plots, which may be related in part to topographic effects. Some of the ridge crest locations from the DTM are also plotted on the Bouguer grids in Figures 20 through 23. For the higher densities there is an obvious correlation between the gravity troughs and topographic maxima, which becomes less for the lower densities. While no single density appears to offer a perfect solution, a density of 1.7 to 2.0 gm cm^{-3} yields acceptable Bouguer corrections, and most of the plots are shown using these two values. Note that there are some quite pronounced linear features in the gravity which remain regardless of density changes, and are therefore presumably not due to topographic variations.

The corrected data were then merged with the existing regional data set. Due to misties between the new and old gravity stations, a total of 48 of the old points were discarded within the area of the new data, and the locations of the merged data are plotted in Figure 24, which contains 1114 stations. The old data were shifted by –0.6 milligal in Bouguer value in order to tie with the new survey. A 50 m grid of the merged data for a density of 2.0 gm cm^{-3} is shown in Figure 25. In order to illustrate the anomaly over the prospect, the regional trend was removed from the grid. The residual grid was created by subtracting a grid smoothed with a two-dimensional Hamming operator from the original grid, where the width of the operator was 25 km, which effectively retains wavelengths up to about 50 km. This residual gravity plot (Figure 26) enables the local features and limits of the prospect anomaly to be seen more clearly. Unfortunately the 3 km gap in gravity coverage to the east of the state border does not allow the eastern part of the anomaly to be defined properly, although the grid suggests that the anomaly may continue as far eastwards as 499000 m E. The Bouguer and residual grids for a density of 1.7 gm cm^{-3} are shown in Figures 27 and 28.

The Bouguer grid and residual for just the prospect area are shown in Figures 29 and 30 for 1.7 gm cm^{-3}, and in Figures 31 and 32 for 2.0 gm cm^{-3}. The residual grid used for Figure 32 is also shown in Figure 33, with the illumination from the southeast in order to highlight northeasterly trends in the data. While some linear features can be seen in Figure 33, they tend to be less prominent than the generally northwesterly trends in Figure 32. This suggests that the major faults tend to have a west to northwest orientation. The Bouguer and derivative plots enable some limits to be placed on the structure, including possible fault patterns. The horizontal gradient of the residual gravity was obtained using an anisotropic operator 500 m wide in order to enhance the local changes in slope of the gravity field. Ideally a maximum in the gradient should occur over a lateral change in density, such as at a fault. In the gradient plot for a density of 2.0 gm cm^{-3} in Figure 34 a number of linear trends can be seen. Some of the smaller features may be due to near-surface changes in lithology or remaining topographic effects, but the better defined trends may represent structures such as faults. The gradient maximum along the coastline should be treated with some caution, as it may be caused by a remaining level shift between the new survey and the older data.

Several of the strongest lineations located in the gradient grid have also been plotted on the residual in Figure 35. A northwesterly trend at about 495000 m E appears to coincide with a marked change in the amplitude of the anomaly. On the Waarre time interpretation map, the western limit of the main anomaly has been placed at a NNE-trending fault at about 494500 m E, but there appears to be little evidence for such a fault in the gravity data. Similarly, the expected strong east-west fault along the northern edge of the prospect from the seismic interpretation does not have any pronounced expression in the gravity derivative plots, although the gravity anomaly does have a general east-west trend. Of course if the density contrast across a fault is minimal in the shallower parts of the section, then the gravity gradient will also be low, and hence the fault may not be identified in these grid enhancements. It is notable that there are some quite sharp variations in amplitude of the anomaly, albeit of only a fraction of a milligal. These indicate that significant lateral changes in density, perhaps due to faulting, occur even in the shallow parts of the sedimentary section. Finally, some of the lineations interpreted from the magnetic data further on in this report are plotted on the gravity residual in

Figure 36. Some of these coincide with gravity trends or boundaries, which suggests that they are real, and could even be evident in seismic sections.

The maximum amplitude of the anomaly is of the order of 2 milligals relative to the surrounding areas. If we assume that the density contrast between the uplifted sediments of the prospect and the adjacent sediments at the same depth is 0.1 gm cm^{-3}, then a 2 km wide uplifted two-dimensional block 2000 m high with a depth to its upper surface of 1000 m would give an anomaly of about 2.5 milligals over its centre. This is similar to that observed, but no useful interpretation of the gravity involving detailed forward modelling could be carried out without additional information, such as that from seismic data, to constrain solutions.

Magnetic data processing

The prospect area is covered by existing magnetic surveys, and these have been used to produce a regional grid for analysis. Part of the 200 m total magnetic intensity (TMI) grid for South Australia was converted to zone 54 coordinates and regridded at a 100 m interval, to give Figure 37. This grid contains rather poor detail, and also suffers from spurious trends in some areas, as shown in the residual plot in Fig 38. The area is covered by a 1993 survey (P1) with 400 m flight line spacing, flown at an altitude of 60 m in a north-south direction, but the existing grid also suffered from gridding artefacts and hence had to be created again. The profile data were also available, and could therefore be used to generate an improved grid. The data required complete re-levelling, but this was achieved satisfactorily without losing any of the fine detail, after which the IGRF field was removed. The Victorian data was part of a large regional survey flown in 1999 which was available from the Victorian Department of Natural Resources and Environment. The flight lines in this area were in an east-west direction at 200 m spacing and at 80 m altitude, and extend about 2 km to the west of the State border. These data only required minimal additional levelling. The levelled South Australian and Victorian grids were then merged using proprietary methods to give a regional 50 m TMI grid, as shown in Figure 39, where the join between the grids is reasonably seamless in most places. Reduction to the pole (RTP) was then carried out using standard Fourier methods to give Figure 40, in which the magnetic anomalies should now correspond approximately with the locations of the sources. Non-linear colour scales have been used for these plots. The triangular gap in coverage extending up to the join of the State border and the coastline was filled in with a trend surface prior to the RTP process in order to minimise edge effects near the prospect area. This expanded grid was also used for the depth estimation routines to reduce the effects of steps in data values at the edge of the grid.

The magnetic grids are now shown in more detail for an area 35 km square, where the TMI and RTP grids are given in Figures 41 and 42 respectively. The data contain many short wavelength anomalies which are due to near-surface and possibly intra-sedimentary sources. In order to enhance these anomalies, and reveal some of the more subtle structural changes, several derivative enhancements are also presented. The TMI residual obtained with a two-dimensional operator 1000 m across is given in Figure 43, and the RTP residual is shown in Figure 44. These effectively retain wavelengths or anomalies which are less than about 2 km across, and the short wavelength residuals appear very similar for both grids. The RTP residual is also given as a monochrome plot

in Figure 45. A longer-wavelength version of the RTP residual using an operator 2500 m across is shown in Figure 46. The locally high values are light or red in these plots, and it is often easier to discern details in the grey-scale rather than the colour residual plots. The horizontal gradient of the RTP grid is also shown in Figure 47, although this does not reveal regional trends so clearly as the other derivatives. Note that there is a change of texture, in both amplitude and trend, across the derivative plots due to the different line direction and spacing, as well as flight altitude, between the two surveys used in the magnetic compilation. It is difficult to avoid these effects if we wish to retain as much high frequency information as possible in the grid, and of course this can only really be reduced by a closer line spacing in the data. Many of the very localised high-amplitude spots in these derivative plots may be due to cultural effects, and some of the linear trends are due to railways or power lines. However, there are numerous trends which are caused by outcrop or drainage patterns, surface accumulations of magnetic material or fault traces. The very high amplitude areas at the left and upper left of these plots are due to volcanic lithologies.

A filter to highlight regions with very shallow or regolith magnetic sources is used to give the plot in Figure 48, which retains some of the features of the residual maps in Figures 43 through 47 while minimising the more regional geological trends. It has been proposed that an ascending hydrocarbon plume can cause excess concentrations of magnetite at shallow depths, which may then lead to observable high-frequency magnetic anomalies (Donovan et al., 1979; Henderson et al., 1984; Machel and Burton, 1991; Saunders et al., 1991). The “regolith” enhancement in Figure 48 is designed to highlight any such area of shallow magnetic sources. Most of the anomalous zones or points can be related to known geology or cultural features, while there do not appear to be any abnormal areas of shallow magnetic sources in the vicinity of the prospect.

The RTP magnetic grid is also shown in Figure 49 for an area of 8 by 17 km around the prospect. The long-wavelength residual of the RTP is given in both colour and monochrome in Figures 50 and 51, while the short-wavelength residual is shown in Figures 52 and 53. Some of the linear features may be related to fault traces, and it would be worthwhile posting the locations of faults from seismic sections on these plots to determine if there is any correlation. If faults extend upwards to the shallower parts of the section, there may be sufficient magnetic material within the sediments to give some observable effects in the residual plots. Some of the magnetic lineations appear to extend over at least several kilometres, and hence may assist in correlating faults across the seismic sections, which are rather few for this area. Trends can be picked from the residuals, especially by viewing the plots obliquely, and some of these have been marked in Figure 54. The data line orientation and spacing will affect the definition of trends in some directions, and some of these may be related to topography. It is also easy to pick more trends than may be warranted by the data quality, but with care it should be possible to correlate some of the lineations with faults or real structural features.

The regolith operator is also shown in Figure 55 in order to highlight the highest spatial frequencies due to sources of near-surface origin. It is likely that most of the point anomalies in this plot are cultural in nature, while the low-level regional trends are due to the near surface lithology and do not appear to be associated particularly with the prospect area.

Magnetic depth estimation

Forward modelling of the magnetic field is quite tedious and can yield fairly ambiguous results without additional constraints on the interpretation. However, since the greatest magnetic susceptibility contrast is generally between the largely non-magnetic sediments and an often much more magnetic basement, it may be possible to obtain some idea of basement depth from inversion methods. Some techniques such as Werner deconvolution are quite dependent on the type of magnetic model assumed in the analysis and can produce rather nebulous results, especially where there are multiple sources. Model-based inversion schemes may not produce any depth estimates at all if there are no strong anomalies. Therefore two-dimensional spectral analysis has been used here with the magnetic data in order to outline the basement configuration, since even low-amplitude anomalies can still yield useful results. This is based on methods which follow the theory of Spector and Grant (1970), and is not very sensitive to the actual geometry of each source. In spectral analysis the frequency content of the potential field (gravity or magnetics) is related to the depth to the source, and depths are derived from the slope of straight segments of the power spectrum, which is obtained here by folding the two-dimensional spectrum into one dimension. The process has been automated to enable many depth estimates to be derived across a complete grid area, which is not really practicable in a manual interpretation of power spectra. The depth picking process from the power spectrum is also automated and permits a number of depth values, possibly corresponding to different sources, to be obtained at each location. Data within a finite window are used to obtain the spectrum, which therefore represents the effect of an ensemble of sources and hence may limit the definition of small lateral changes in structure. In theory the width of the spectral window has to be at least four times the maximum source depth, although in practice it has been found that it should probably be at least 6 to 8 times the depth, which can result in a further reduction in lateral resolution. However, due to the tapering procedures used to condition the data within each spectral window, the actual depths found tend to be influenced more by sources towards the centre of the window, which therefore enables lateral changes in depth to be observed over distances which are somewhat smaller than the spectral window width.

While near-surface and probably intra-sedimentary magnetic sources exist, from the original line spacing it is unlikely that sources shallower than about 200 m will be resolved satisfactorily by two-dimensional spectral analysis. The maximum spatial frequency used in the power spectra was limited to 0.001 cycle m^{-1} for a spectral window width of 10000 m and 0.0005 cycle m^{-1} for greater windows. Thus most of the high-frequency end of the power spectrum is not used for depth estimation, as this is dominated by numerous very shallow sources or noise effects and may even yield spurious deeper values due to irregularities in the slope of the spectrum. The regional RTP magnetic grid (Figure 40) was employed to place the larger depth values reasonably close to their true position, and also provides a buffer zone around most of the survey to reduce edge problems during spectral analysis. The grid with the null area near the prospect filled in was used to avoid the strong edge effects which would otherwise occur in this area.

The spectral analysis was carried out with a series of increasing windows, in order to define the relatively shallow sources through to the deeper regions or basement. In each

case, depths were found at 1 km intervals across the grid, and several thousand values were obtained for each analysis. The deepest value at each point then gave a "basement" surface for that window. Typically if the greatest depth found at a point is less than about one-tenth of the window size then it is possible that this represents an actual source depth. Depths which are apparently greater, down to around a fifth of the window width, may not have the correct depth value but do indicate that deeper sources exist and that the spectral window should be expanded to resolve these. Thus by repeating the analysis with increasing window sizes and plotting the greatest depths at each stage it is possible to follow the improved definition of the deeper sections of the basin. There is a loss of lateral resolution for the larger windows, but in practice this has often proved to be quite a reliable method of outlining the main variations in the basement geometry. None of the depths shown here has been corrected for the nominal survey altitudes of 60 or 80 m.

The depths obtained for spectral window sizes of 10000, 20000, 30000 and 40000 m are plotted in Figures 56 through 59 respectively. Each depth point is plotted as a pixel of finite size rather than as a continuous grid since this gives a better idea of the variations and minimises the effects of spurious or abnormal local values. Scattered values which are quite different from surrounding depths may be due to very strong local anomalies, or else due to interference or noise which has affected the low-frequency end of the power spectrum. Sometimes slopes which are characteristic of deep sources can be inferred visually from the power spectrum, but even after conditioning of the spectrum the routine which picks the depths may not be able to resolve the depth with sufficient precision to give a usable value. For large windows additional depths may be determined below the supposed basement surface due to intra-basement sources, and hence some care needs to be used in analysing the results.

For the smallest spectral window (Figure 56) a large number of shallow depths have been picked around the two volcanic areas towards the western edge of the area. Similarly, the shallow depths along the eastern edge may be due to the influence of the strongly magnetic area which can be seen at about 520000 m E in the TMI map in Figure 39. With increasing window sizes the local effects of near-surface sources become less apparent and regional variations become more prominent. The influence of the strong shallow sources just to the east of the map area also tends to extend further to the west. The colour scale is different for each spectral depth plot in order to optimise the use of colours for each range of depth values. The data indicate that there are two main basins to the west of 500000 m E separated by a basement high at about 5800000 m N. The basin depths may go down to around 6000 m, with the high at about 3500 m depth. There is a loss of lateral resolution for the larger windows, the sizes of which become appreciable compared to the dimensions of the depth plots. This may also lead to a slight shift in the locations of the depth extremes. However, the data do suggest that the prospect lies on the edge of a NW to NNW trending structural high, with a depth of perhaps 3500 to 4000 m, adjacent to a fairly deep basin. It is unfortunate that the magnetic data has a gap close to the prospect area, which may affect some of the depth results nearby. There appears to be a third basin about 10 km to the east of the border.

Although these diagrams give an idea of the regional variations in basement depth, it is also useful to view the depth solutions as cross sections. The depths obtained with a 30000 m wide spectral window are presented on a series of three west-east sections in Figures 60 through 62 at intervals of 5 km in a north-south direction. Each section is 47

km long, and extends from 473000 m E to 520000 m E, and down to a depth of 5000 m. Data from three adjacent rows of depth solutions (1 km apart) are plotted on each section in order to accentuate the trends. The width of each section is the same as the depth maps. It can be seen that despite the relatively large spectral window the method may resolve appreciable variations in depth over distances of only 10 km. Many of the shallow depths are probably influenced by local structure and noise, but some patterns within the sedimentary section can be observed which may be due to magnetic content within the sediments. Similar cross sections are also given in Figures 63 through 65 for a spectral window of 40000 m. There has been some further loss of lateral resolution for this larger window, and hence the depths for the 30000 m window may give a better idea of the basement variations.

As a check on the depths obtained from spectral analysis, depth estimates were carried out using the "half-slope" method of Peters (1949). In this process, the maximum gradient of an anomaly is found, and the horizontal distance between the two points where the gradient is half this value is then measured to give an indication of the depth to the source. This distance is divided by a factor varying from 1.2 for dikes to 2.0 for contacts to give a good approximation to the actual depth. Since the exact nature of the source is often not known, or if there are many sources, a divisor of 1.6 is often used. Although the method is simple in principle and was one of the earlier inversion techniques, it is in fact based on sound theory and can yield reliable results. The method is frequently used graphically for quick depth estimates on just a few anomalies, and has been automated for use with both profile and gridded data. Tests on model data, including multiple sources, indicate that it can give quite accurate results, and with real data these can compare well with depths from other techniques such as Werner and Euler deconvolution.

Half-slope depths were obtained along the columns of the grid rather than from the original data profiles. Many of the geological and anomaly trends are not normal to the flight line direction or the grid rows or columns, and hence the half-slope method tends to over-estimate depths here. In the present analysis a depth value is generally obtained each side of an anomaly peak or trough. Depth points tend to cascade downwards away from the point immediately above the source (as in Euler deconvolution), and a large number of depths are found across the grid, typically several thousand in the present analysis. Hence the shallowest values within small fixed regions of finite size were retained as the depth estimates. While there is a strong regional gradient in the magnetic data, there are relatively few prominent localised anomalies which can be used to give depth estimates. The residual was first obtained along each grid column in order to remove the regional trends and enhance the local variations in the data. A Hamming operator 40 km long was used to derive the residual, which retains wavelengths up to about 80 km. The method will find depths from even very localised near-surface anomalies, including noise, to the exclusion of the required deeper sources. The residual profiles were therefore smoothed with a Hamming operator 4000 m wide prior to depthing. The depth estimates are shown in Figure 66, and may be compared to those in Figures 58 and 59. The half-slope depths also exceed 6000 m in places, while more shallow areas can be seen in the vicinity of the volcanics and towards the eastern part of the plot.

Radiometric data

Over the years there have been numerous studies to determine whether measurable near-surface effects occur above hydrocarbon accumulations, so that non-conventional geophysical or geochemical surveys can be used for exploration (e.g. Duchscherer, 1980; Schumacher 2000. A variety of mechanisms have been proposed for the origin of the observed geophysical anomalies, which include magnetic, radiometric and electrical effects. These do not appear to be well understood at present, and are probably highly dependent on local conditions. In many locations no anomalies are observed, but if the application of non-conventional methods yields useful results in only some areas they should still be considered due to the availability of the appropriate data in many regions and their relatively low cost. Positive results may serve to highlight locations for more detailed investigation (e.g. Saunders and Terry, 1985; LeSchack, 1994) and can often provide a useful overview of substantial areas with minimal effort.

The existence of radiometric anomalies over some fields has been known for many years (e.g. Armstrong and Heemstra, 1972a, 1972b). Both radiation lows (Kilmer, 1983) and maxima (Morse and Zinke, 1995) have been associated with the occurrence of petroleum, and halo patterns may be observed due to cementation above the centre of the source (e.g. Duchscherer, 1981). With the advent of high-quality airborne radiometric data in recent years, there has been continued interest in the possible correlation of radiometric anomalies with petroleum occurrences (e.g. Saunders et al., 1987, 1993, 1994). Recent work in the Gippsland Basin (Stewart et al., 2002) identified a prominent radiometric anomaly about 3 km across near Sale which is associated with anomalous surface hydrocarbon concentrations, as shown by subsequent soil analyses. This lends some encouragement to the further use of radiometrics in hydrocarbon exploration.

The South Australian and Victorian airborne radiometric data were gridded at a 50 m interval, and some levelling was applied to the grids to reduce aliasing noise. The two surveys were then merged for each element (potassium, uranium, thorium and total count) to produce grids covering the whole area of interest. The uranium levels for the South Australian data were multiplied by a factor of 0.62 prior to merging to obtain similar levels to the Victorian data. Since uranium tends to have very low count rates, with a consequently poor signal to noise ratio, calibrations for this element may be in error which necessitates some adjustment in merging different data sets. The plots of potassium, uranium, thorium and total count are given in Figures 67 to 70 respectively. A ternary plot for potassium (red), thorium (green) and uranium (blue) is shown in Figure 71, where areas with higher count rates are lighter in colour. Areas covered by water have low activity and appear black in ternary plots. It should be remembered that the observed radiometric values originate from the surface lithology, which may even be a thin veneer of alluvium, and do not necessarily represent the underlying geology. Generally there is much more detail evident in radiometric images than would normally be shown from geological mapping.

Anomalous concentrations of uranium in particular are supposed to be indicative of local alteration associated with hydrocarbon plumes, and hence we have to enhance these from the possibly much greater effects due to changes in the regional geology. Typically ratios of the radiometric components are used to minimise the effects of changes in lithology. Saunders (1994) used the ratio of uranium to potassium, normalised on thorium, in order

to derive local anomalies, and applied the method to the Portland quadrangle in the Otway Basin. The process was repeated for the Portland area using the present data set, but there did not seem to be any convincing correlation of the data with known hydrocarbon occurrences. This technique has been included here, since it has been given some prominence in the literature. However, recent studies suggest that the ratio of uranium to thorium would prove a more useful indicator of surface alteration in the presence of hydrocarbons, and hence the results based on the ratio (uranium squared)/thorium are also shown here. Variations in potassium tend to be largely influenced by geological effects which are unrelated to the presence of hydrocarbons.

Radiometric ratios are given for Saunders' algorithm and U^2/Th in Figures 72 and 73 respectively. Colour scales are not given since they do not serve much practical purpose in the plots, although the desired high anomalies should appear towards the red end of the spectrum. The 50 m grids for each element were first smoothed with a 2-dimensional Hamming filter 500 m across before the ratios were obtained, to enable the anomalies to be seen more clearly. It is unlikely that any significant anomalies will have been eliminated in this process. The results from Saunders' algorithm (Figure 72) appears to be rather similar to the inverse of the potassium plot (Figure 67), with no significant anomalies near the prospect area. The U^2/Th variations (Figure 73) are less obviously related to any single element, and include a local maximum in the ratio over the prospect. There are also some textural differences between the data from the two surveys, possibly due to acquisition parameters and instrument calibrations. Ratio values over water are essentially noise, since the radiometric response there should ideally be zero.

The potassium, uranium, thorium and total count are plotted in Figures 74 to 77 for a localised area 8 by 17 km around the prospect, and the ternary plot is shown in Figure 78. There is considerable detail in these plots, most of which is presumably associated with variations in the surface lithology. In fact the correlation of the separate elements and the total count with elevation for the prospect area is about 0.5, which indicates that care should be used in interpreting the radiometric plots in terms of structure. Correlations with the DTM were also obtained for the radiometric ratios, and for Saunders' algorithm the correlation was around –0.5, which suggests that topographic effects are still important. For U^2/Th, shown in Figure 79, the correlation with the DTM is only 0.17 using the smoothed grids, and –0.03 with unsmoothed data, which indicates that the U^2/Th value may reflect effects which are largely uncontrolled by the topography. This ratio appears to show an anomaly about 1 km in north-south extent which lies over the prospect at about 5790000 m N and extends to about 5 km west of the State boundary. The anomaly occurs in both the South Australian and Victorian data sets, but does not appear to extend east of the border.

The radiometric ratio anomaly is also shown in Figure 80 with the lineations from the magnetic residual in Figure 54 as an overlay. It can be seen that there is quite a remarkable coincidence between the anomaly and part of the local gravity maximum (cf. Figure 36), as well as the bounding lineations (possibly faults) which can be inferred from the gravity and magnetic data. The anomaly appears to terminate in the west at about 492000 m E. While the source of the radiometric anomaly is open to speculation, its coincidence with the structure is interesting.

Conclusion

The recent gravity survey gives greatly improved definition of the anomaly associated with the prospect, and enables some possible structural features to be inferred from the derivative enhancements of the gravity grid. The anomaly extends at least 5 km in an east-west direction, and the gravity data show several lineations in a roughly northwesterly orientation which intersect the anomaly. Since these are quite sharply defined, they must be of relatively shallow origin, but may represent deeper structure or faulting. The anomaly maximum becomes lower at about 495000 m E in the west, but its eastward extent can not be defined due to the lack of data in that direction. The large east-west fault which is expected to form the northern boundary to the prospect is not evident in the gravity data, although there are a number of trends in other directions in the gradient plots. Ideally these features should be checked against other data, especially to determine whether they have any expression in the shallower parts of the seismic sections. The seismic lines are plotted on the gravity residual in Figure 81. This suggests that the approximately NNE-trending fault which intersects dip line OE01C-01 shown on the Waarre time interpretation map in fact has an incorrect orientation, and should be northwesterly. Since there are obviously a number of faults through the area and very few seismic lines, it is not surprising that some of the fault correlations may be incorrect. This effect has been observed elsewhere even when many seismic lines exist, but where detailed gravity coverage is also available as a check on interpretation. The existing strike line (OE01C-3) is not very far from the crest of the anomaly, but another strike line about 500 m further north would probably be closer to the maximum.

While there are no prominent magnetic sources near the prospect, apart from those which are probably cultural in origin, a number of linear features can be seen in the magnetic derivatives which may represent structural trends. Some of these can be correlated with features in the gravity field, and hence may assist in the interpretation of the area. A tentative analysis of the magnetic depths indicates that basement depths away from the prospect may reach 6 km, although basement is probably somewhat shallower (3.5 to 4 km) in the vicinity of the structure. A well-defined radiometric anomaly is associated with the gravity maximum and can also be correlated with the magnetic lineations, although the cause of the radiometric feature is open to speculation.

In summary, the new gravity survey provides a much clearer idea of the outline of the prospect, and also enables some structural features to be inferred. When additional gravity data can be acquired in Victoria the eastward extent of the anomaly should become more apparent. The available magnetic and radiometric data have also yielded information which may help in structural interpretation, as well as highlighting a radiometric anomaly of possible exploration interest.

References

Armstrong, F.E. and Heemstra, R.J. 1972a. Radiometrics proposed for exploration. Part 1.
Oil and Gas J., vol. 70, pp. 88-97.

Armstrong, F.E. and Heemstra, R.J. 1972b. Radiometrics proposed for exploration. Part 2.
Oil and Gas J., vol. 70, pp. 152-161.

Donovan, T.J., Forgey, R.L. and Roberts, A.A. 1979. Aeromagnetic detection of diagenetic magnetite over oil fields.
Am. Assoc. Petrol. Geol. Bull., vol. 63, pp. 245-248.

Duchscherer, W. 1980. Geochemical methods of prospecting for hydrocarbons.
Oil and Gas J., vol. 78, pp. 194-208.

Duchscherer, W. 1981. Nongasometric geochemical prospecting for hydrocarbons with case histories.
Oil and Gas J., vol. 79, pp. 312-327.

Henderson, R., Miyazaki, Y. and Wold, R. 1984. Direct indication of hydrocarbons from
airborne magnetics.
Exploration Geophysics, vol. 15, pp. 213-219.

Kilmer, C. 1983. Radiation lows over productive areas seen as soil geochemical phenomenon.
Oil and Gas J., vol. 81, pp. 179-182.

LeSchack, L.A. 1994. Ground-based magnetic horizontal gradient intensity and radiometric surveys, a cost-effective hydrocarbon exploration tool: Three case histories in western Canada.
CSEG Recorder, October 1994, pp. 7-13.

Machel, H.G. and Burton, E.A. 1991. Causes and spatial distribution of anomalous magnetization in hydrocarbon seepage environments.
Am. Assoc. Petrol. Geol. Bull., vol. 75, pp. 1864-1876.

Morse, J.G. and Zinke, R. 1995. The origin of radiometric anomalies in petroleum basins - a proposed mechanism.
Oil and Gas J., vol. 93, pp. 36-38.

Peters, L.J. 1949. The direct approach to magnetic interpretation and its practical application.
Geophysics, vol. 14, pp. 290-320.

Saunders, D.F., Branch, J.F. and Thompson, C.K. 1994. Tests of Australian aerial radiometric data for use in petroleum reconnaissance.
Geophysics, vol. 59, pp. 411-419.

Saunders, D.F.. Burson, K.R. and Thompson, C.K. 1991. Observed relation of soil magnetic susceptibility and soil gas hydrocarbon analyses to subsurface hydrocarbon accumulations.
Am. Assoc. Petrol. Geol. Bull., vol. 75, pp. 389-408.

Saunders, D.F., Burson, K.R., Branch, J.F. and Thompson, C.K. 1993. Relation of thorium-normalized surface and aerial radiometric data to subsurface petroleum accumulations.
Geophysics, vol. 58, pp. 1417-1427.

Saunders, D.F. and Terry, S.A. 1985. Onshore exploration using the new geochemistry and geomorphology.
Oil and Gas J., vol. 83, pp. 126-130.

Saunders, D.F., Terry, S.A. and Thompson, C.K. 1987. Test of National Uranium Resource Evaluation gamma-ray spectral data in petroleum reconnaissance.
Geophysics, vol. 52, pp. 1547-1556.

Schumacher, D. 2000. Surface geochemical exploration for oil and gas: New life for an old technology.
Leading Edge, vol. 19, pp. 258-261.

Spector, A. and Grant, F.S. 1970. Statistical models for interpreting aeromagnetic data.
Geophysics, vol. 35, pp. 293-302.

Stewart, I.C.F., Dickson, B.L., Taylor, G.M., Deuter, M.J., Annells, R.J. and Mulready, J.N. 2002. Coincidence of radiometric anomaly with surface petroleum near Sale, East Gippsland, Victoria.
Petroleum Exploration Society of Australia J., in press.

List of digital products (data, grids and images)

All grids are in ERMapper format, with a binary grid and an ASCII (*.ERS) header file.

1) SUMMER.DOC
   Word document of text of Summer Hill potential field report.

2) GRAVSURV.DAT
   ASCII file of gravity data from new survey, including terrain corrections.
   25 fields (see format listing)

3) GRAVMERG.DAT
   ASCII file of merged gravity data, densities 1.7 and 2.0 gm cm^{-3}

4) BOUG20.ERS
   Grid of merged gravity, 50 m interval, density 2.0 gm cm^{-3}

5) BOUG17.ERS
   Grid of merged gravity, 50 m interval, density 1.7 gm cm^{-3}

6) B20RES.ERS
   Grid of gravity residual, density 2.0 gm cm^{-3}

7) B17RES.ERS
   Grid of gravity residual, density 1.7 gm cm^{-3}

8) B20GRAD.ERS
   Grid of gravity horizontal gradient, prospect area, density 2.0 gm cm^{-3}

9) B17GRAD.ERS
   Grid of gravity horizontal gradient, prospect area, density 1.7 gm cm^{-3}

10) TMI.ERS
    Regional merged Total Magnetic Intensity grid, 50 m interval

11) RTP.ERS
    Regional merged Reduced to the Pole magnetic grid, 50 m interval

12) RTPRES1.ERS
    Residual grid of RTP magnetics, short-wavelength operator, prospect area

13) RTPRES2.ERS
    Residual grid of RTP magnetics grid, long-wavelength operator, prospect area

14) POTASIUM.ERS
    Potassium grid for prospect area

15) URANIUM.ERS

Uranium grid for prospect area

16) THORIUM.ERS
Thorium grid for prospect area

17) TCOUNT.ERS
Total Count radiometric grid for prospect area

18) RATIO.ERS
Grid of radiometric U^2/Th ratio for prospect area

19) FIGURE*.BMP
Bitmap images of the coloured diagrams in this report

20) FIGURE*.HGL
Line diagrams in HPGL format

Five files of the original survey data are in the directory named SURVEY.

Format of ASCII gravity data set, new survey (GRAVSURV.DAT)

All coordinates are based on the ANS (AMG) spheroid. Gravity values are in milligals

Line number	I8
Station number	I8
Easting (metres)	F12.1
Northing (metres)	F12.1
Longitude	F12.7
Latitude	F12.7
Elevation (metres)	F10.3
Drift	F10.3
Corrected meter gravity	F10.3
Observed gravity	F12.3
Anomalous gravity	F10.3
Free-Air correction	F10.3
Bouguer correction (2.67 gm cm^{-3})	F10.3
Bouguer anomaly (2.67 gm cm^{-3})	F10.3
Terrain correction (2.67 gm cm^{-3})	F10.3
Corrected Bouguer (2.67 gm cm^{-3})	F10.3
Bouguer (2.4 gm cm^{-3})	F10.3
Terrain correction (2.4 gm cm^{-3})	F10.3
Corrected Bouguer (2.4 gm cm^{-3})	F10.3
Bouguer (2.0 gm cm^{-3})	F10.3
Terrain correction (2.0 gm cm^{-3})	F10.3
Corrected Bouguer (2.0 gm cm^{-3})	F10.3
Bouguer (1.7 gm cm^{-3})	F10.3
Terrain correction (1.7 gm cm^{-3})	F10.3
Corrected Bouguer (1.7 gm cm^{-3})	F10.3

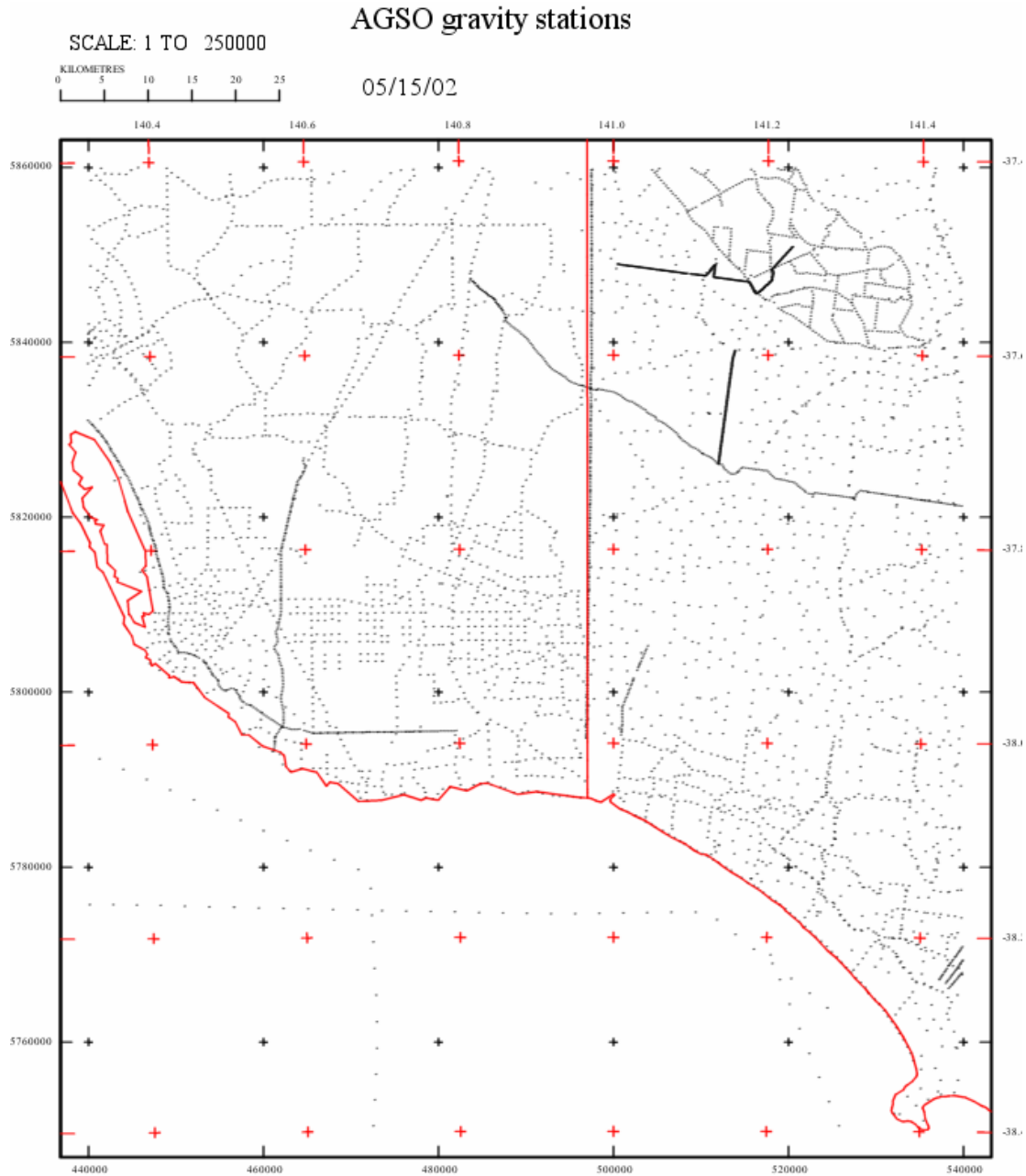

Figure 1 – Gravity Stations in Southeast South Australia and Western Victoria

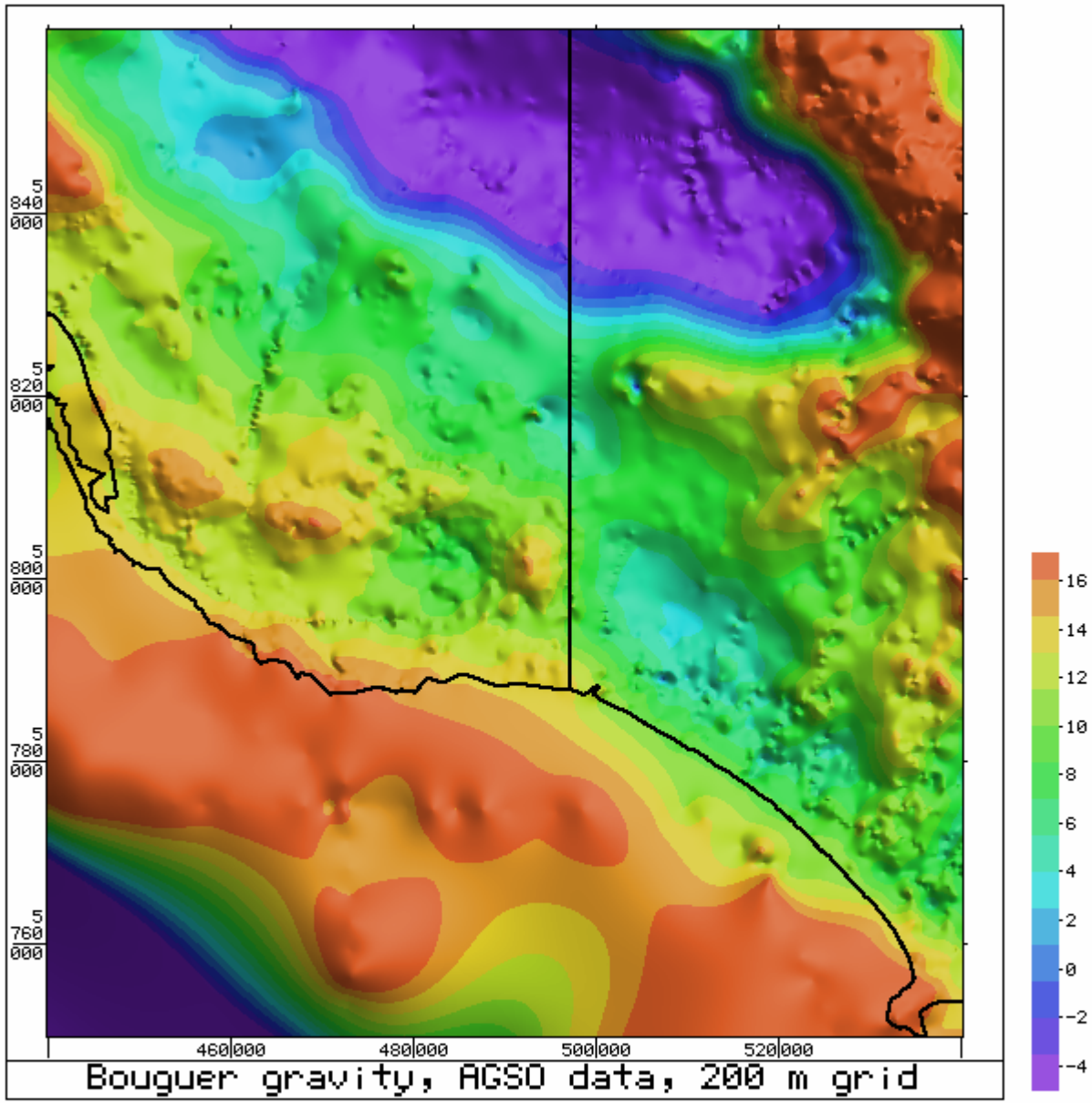

Figure 2. Bouguer gravity, existing data

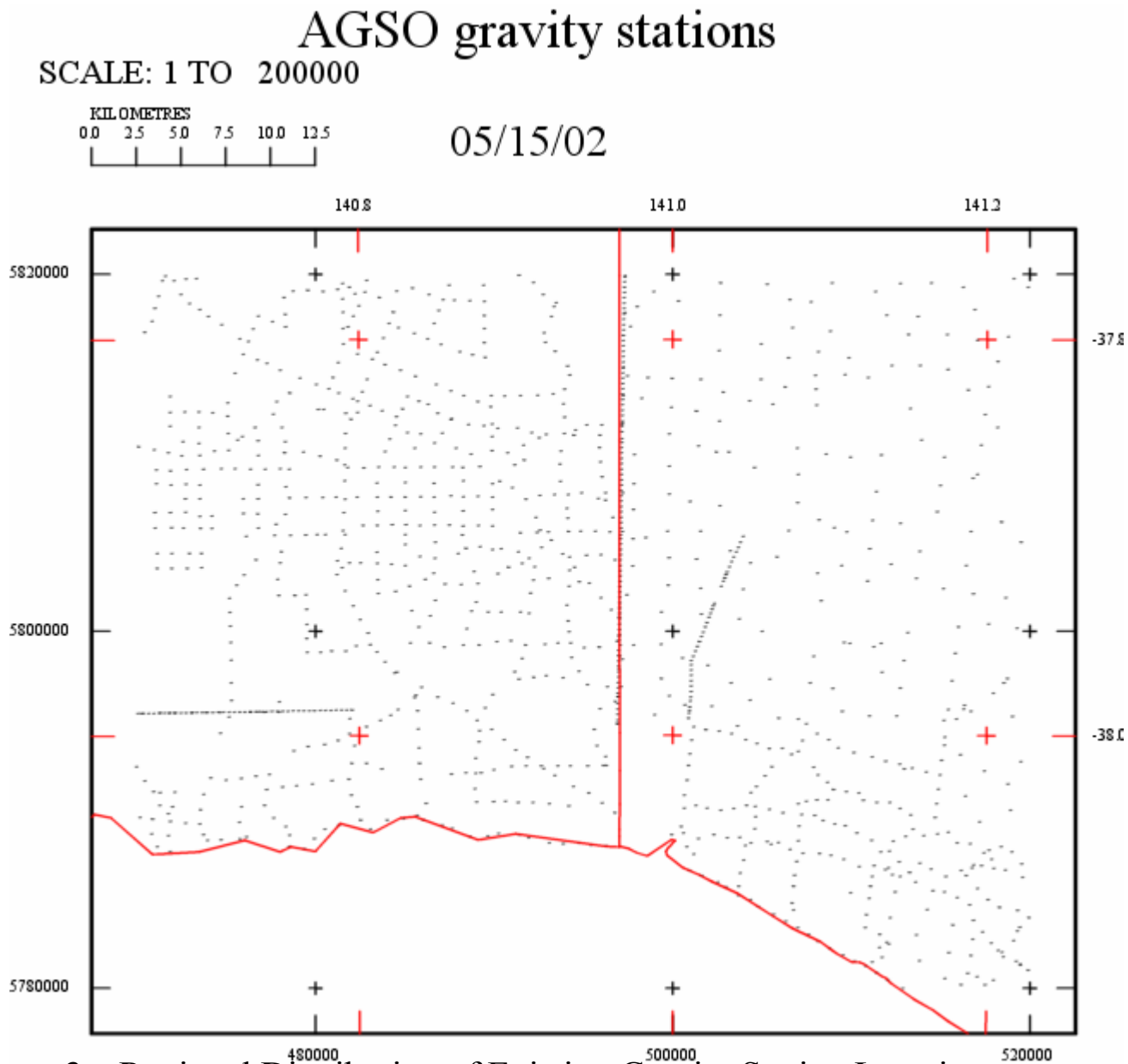

Figure 3 – Regional Distribution of Existing Gravity Station Locations

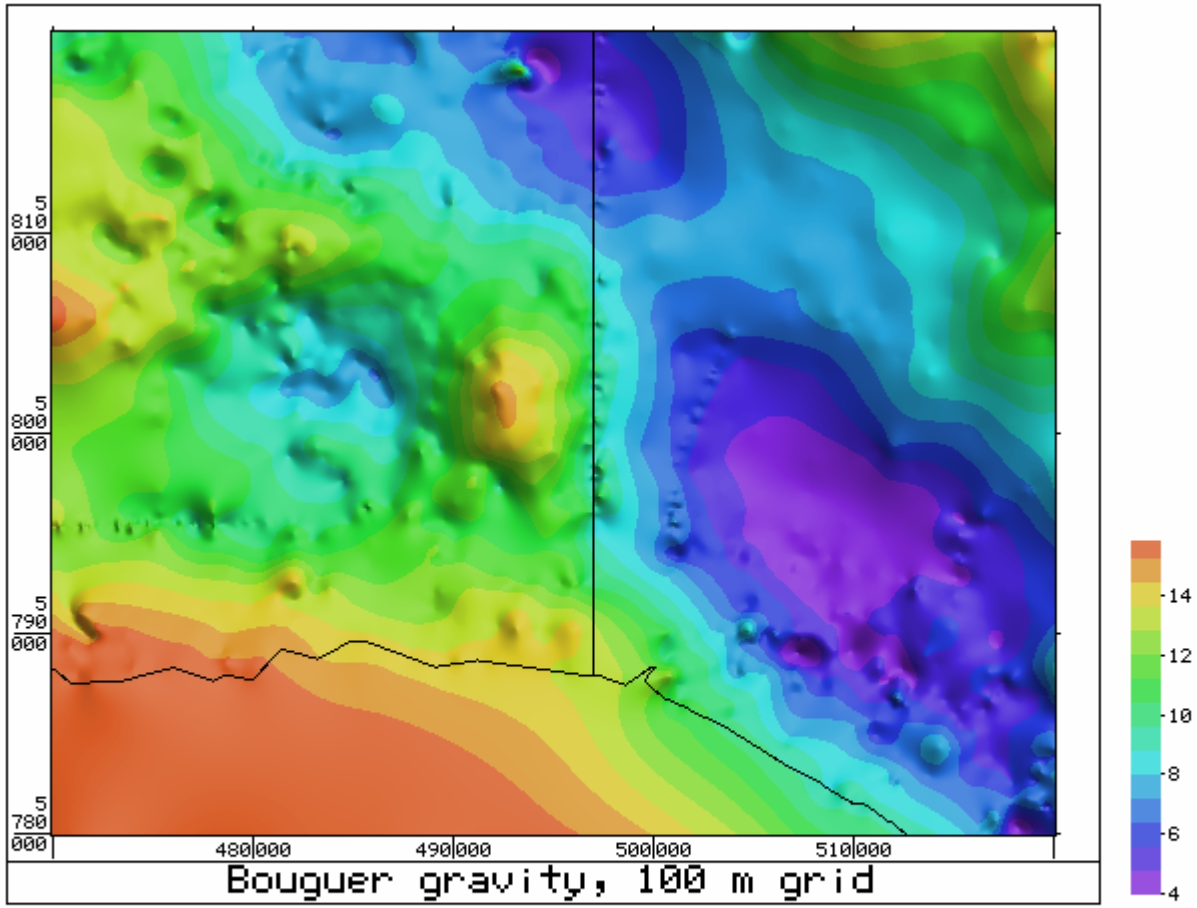

Figure 4. Bouguer gravity, existing data

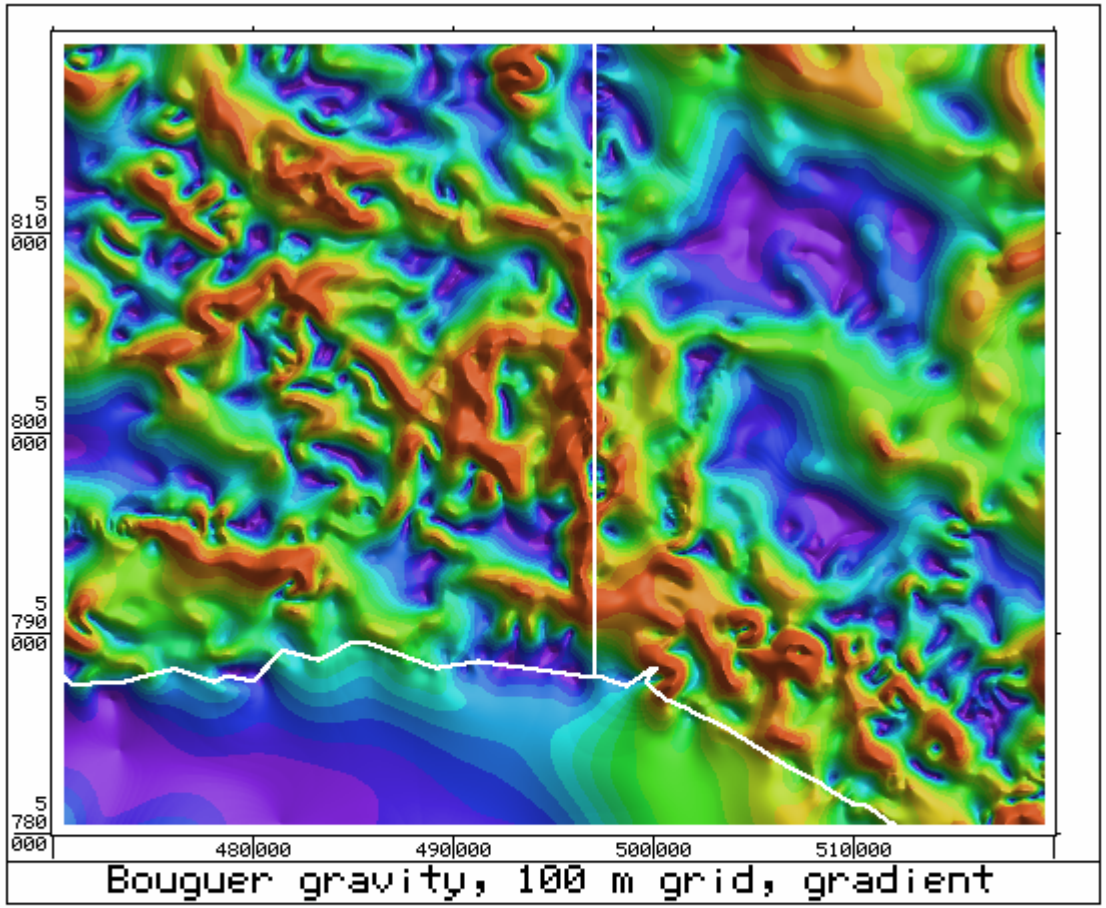

Figure 5. Bouguer gravity, existing data
Horizontal gradient, 1 km operator

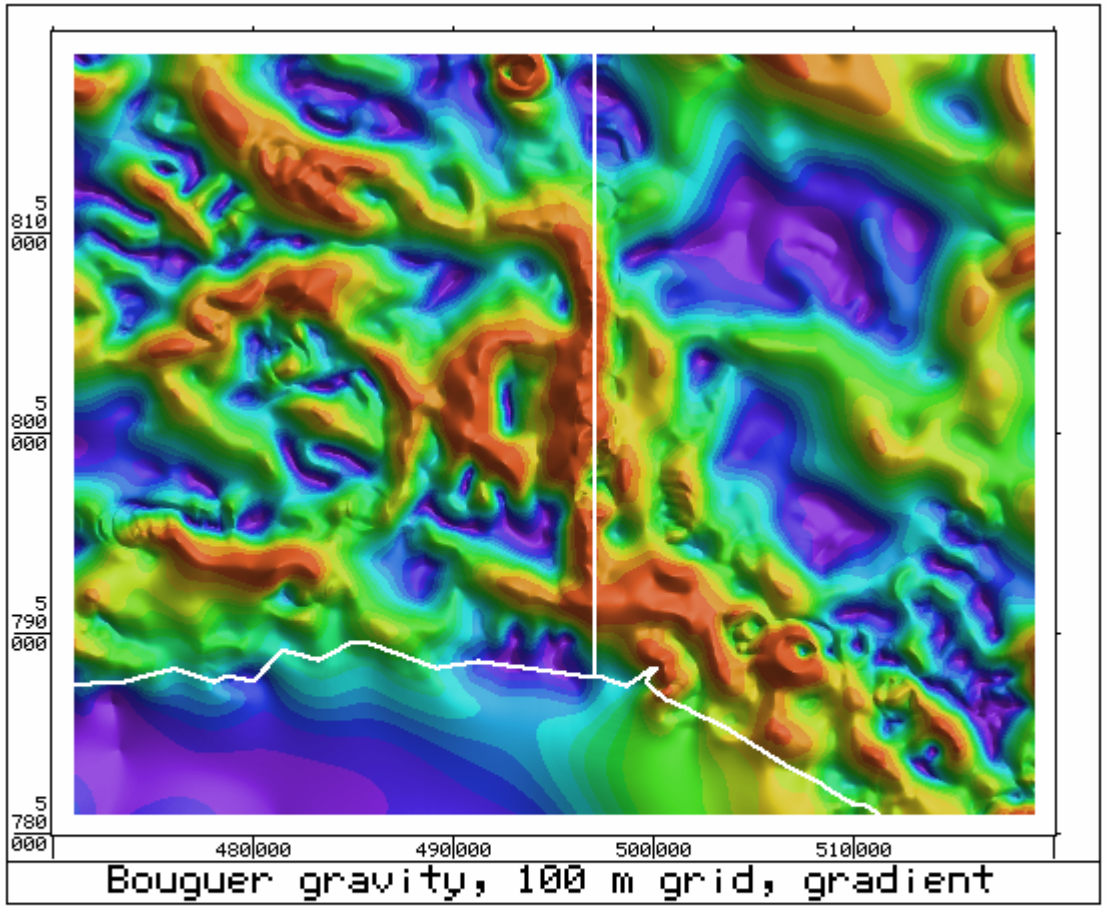

Figure 6. Bouguer gravity, existing data
Horizontal gradient, 2 km operator

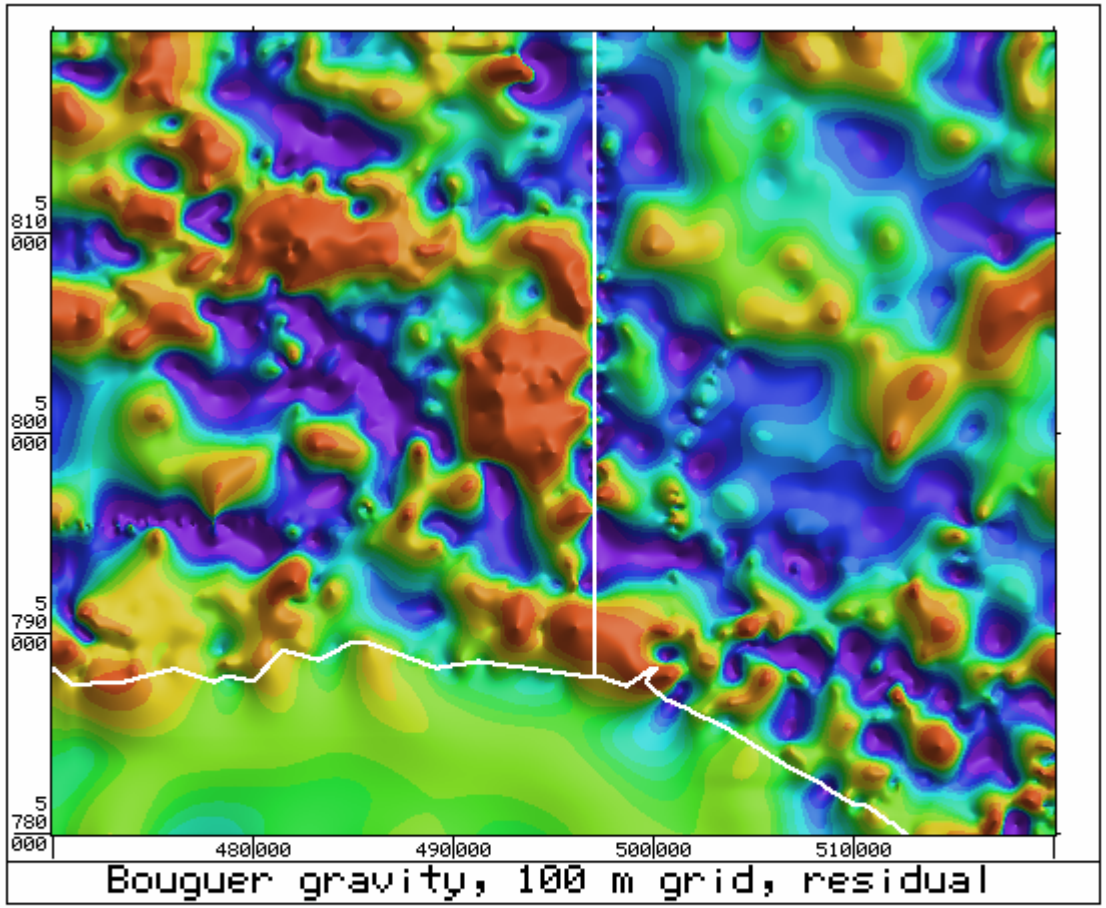

Figure 7. Bouguer gravity, existing data
Residual, 10 km operator

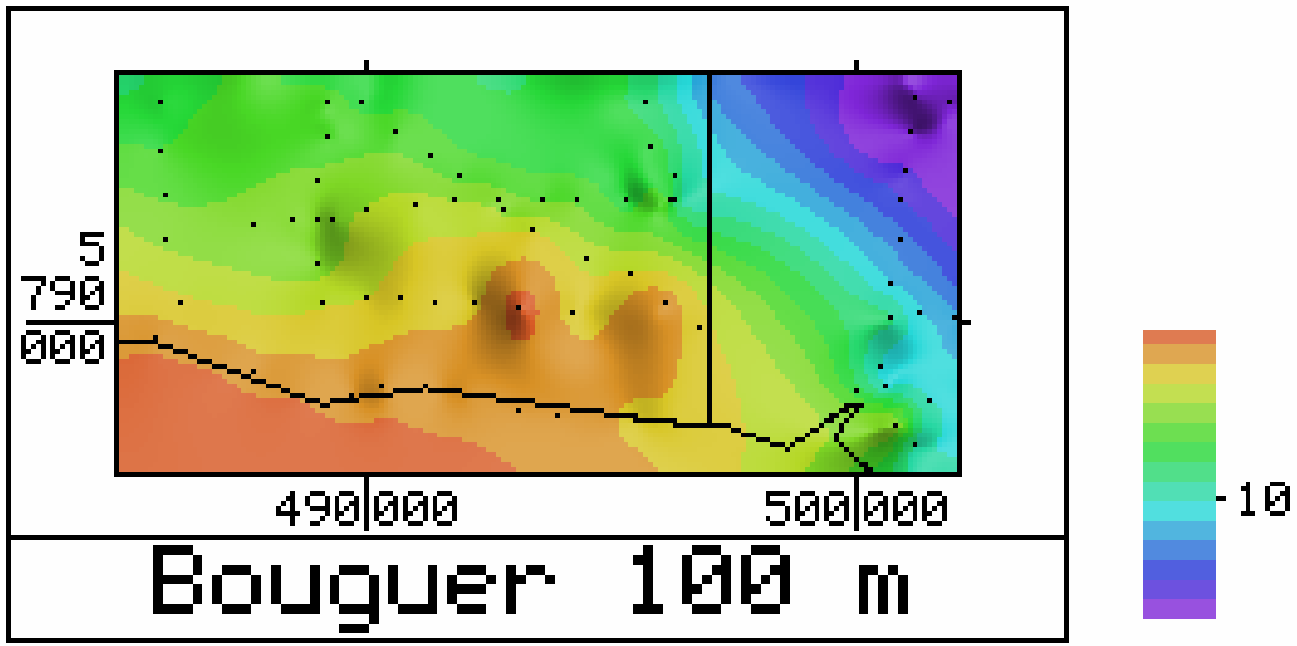

Figure 8. Bouguer gravity, with existing stations, survey area.
Colour interval 0.5 milligal

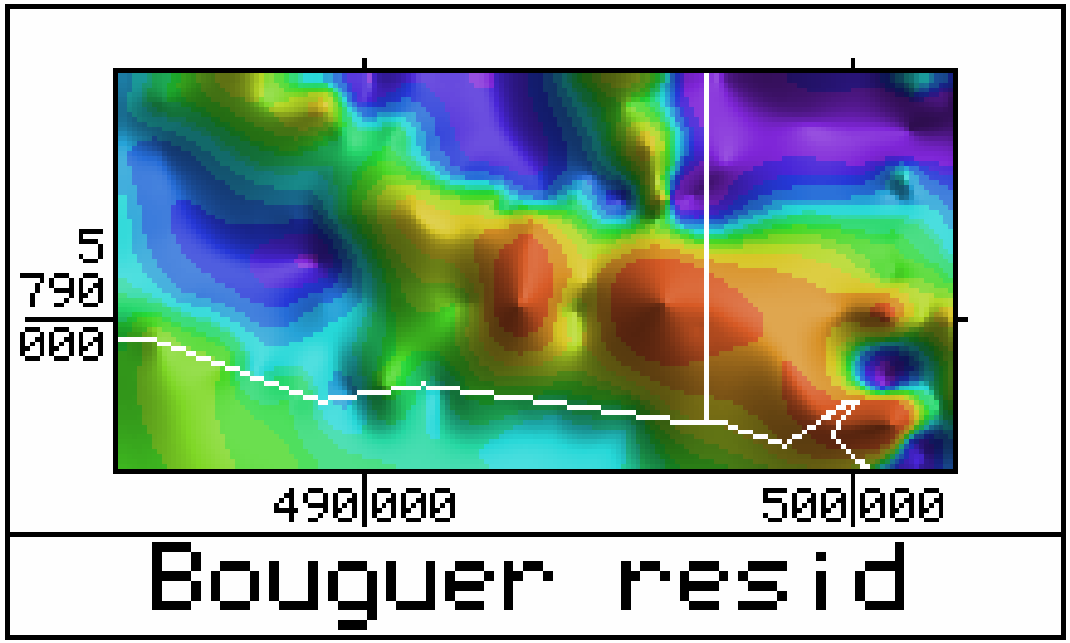

Figure 9. Gravity residual, existing data, survey area

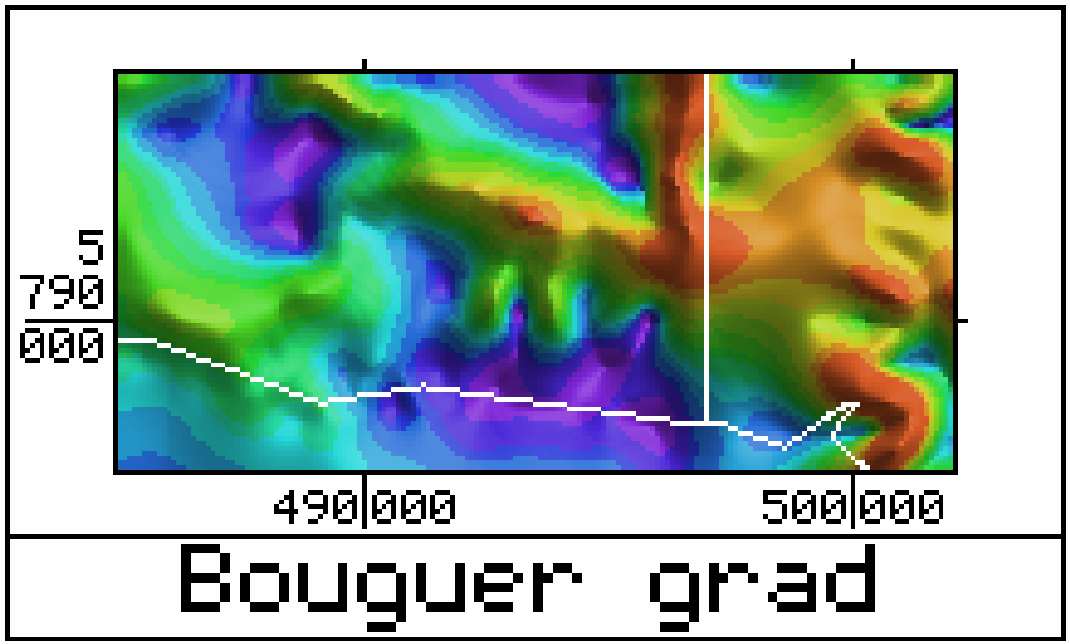

Figure 10. Gravity gradient, existing data, survey area

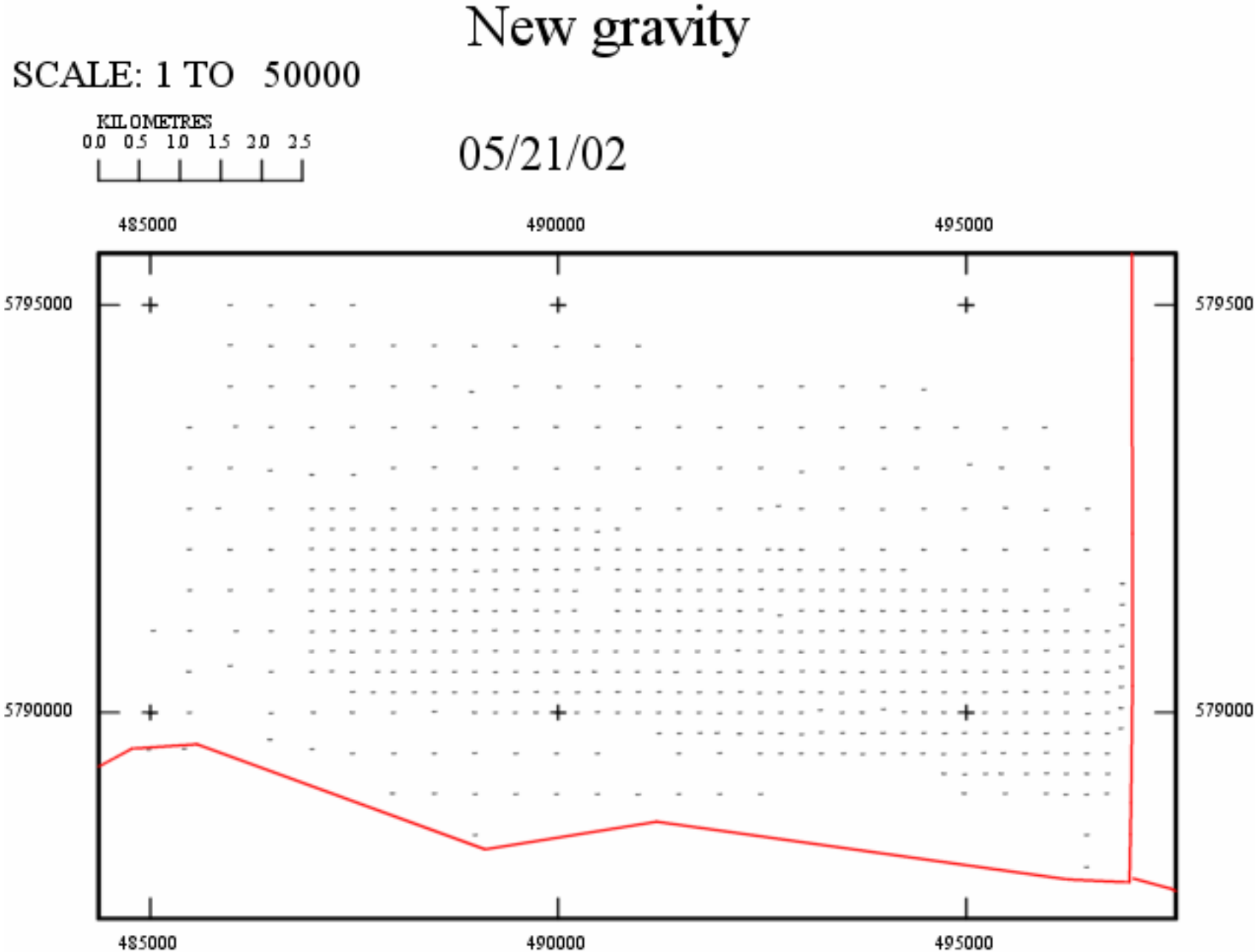

Figure 11 – Gravity Station Locations – New Survey

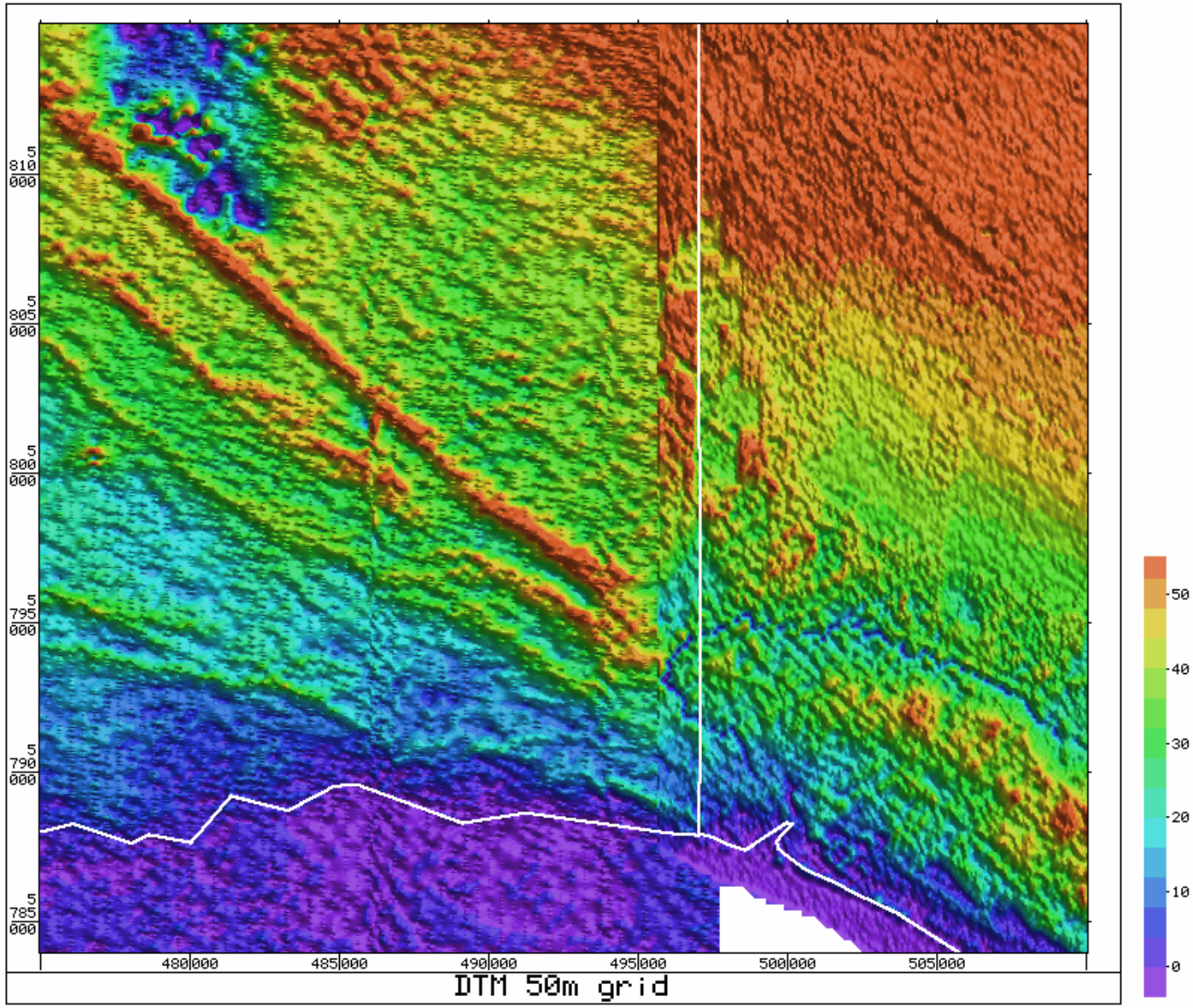

Figure 12. Digital Terrain Model from airborne data

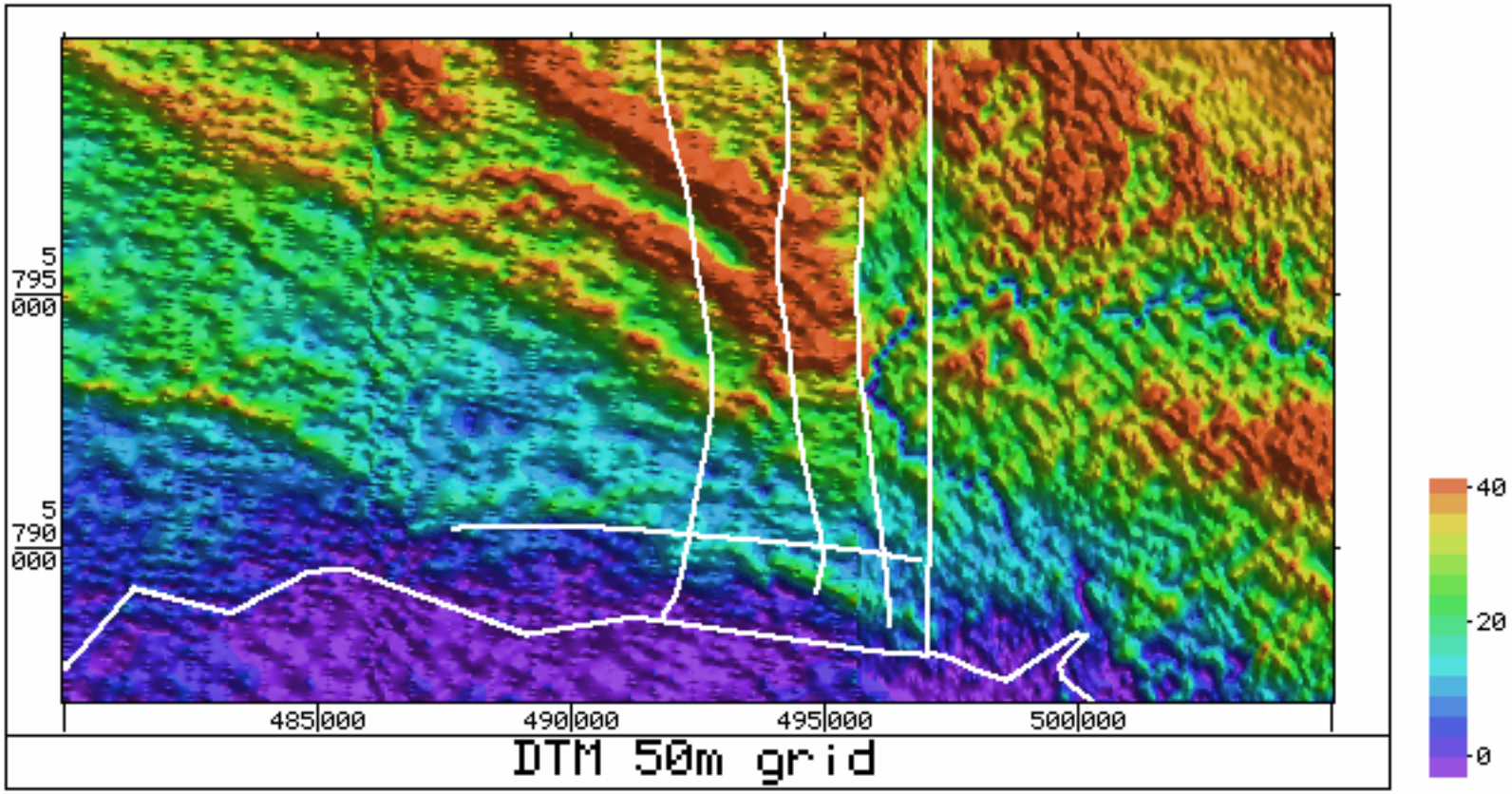

Figure 13. Digital Terrain Model from airborne data, showing location of 4 seismic lines

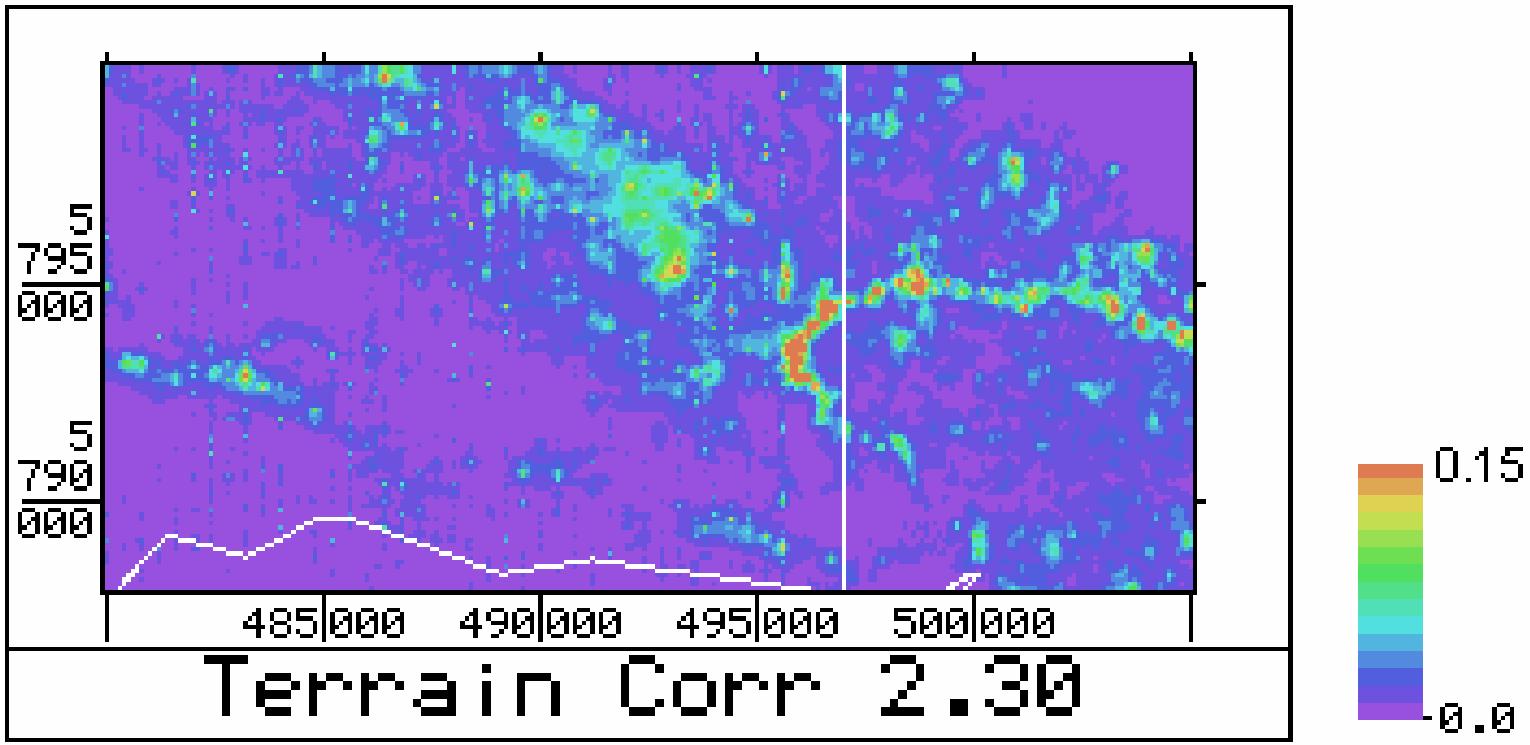

Figure 14. Gravity terrain corrections from DTM

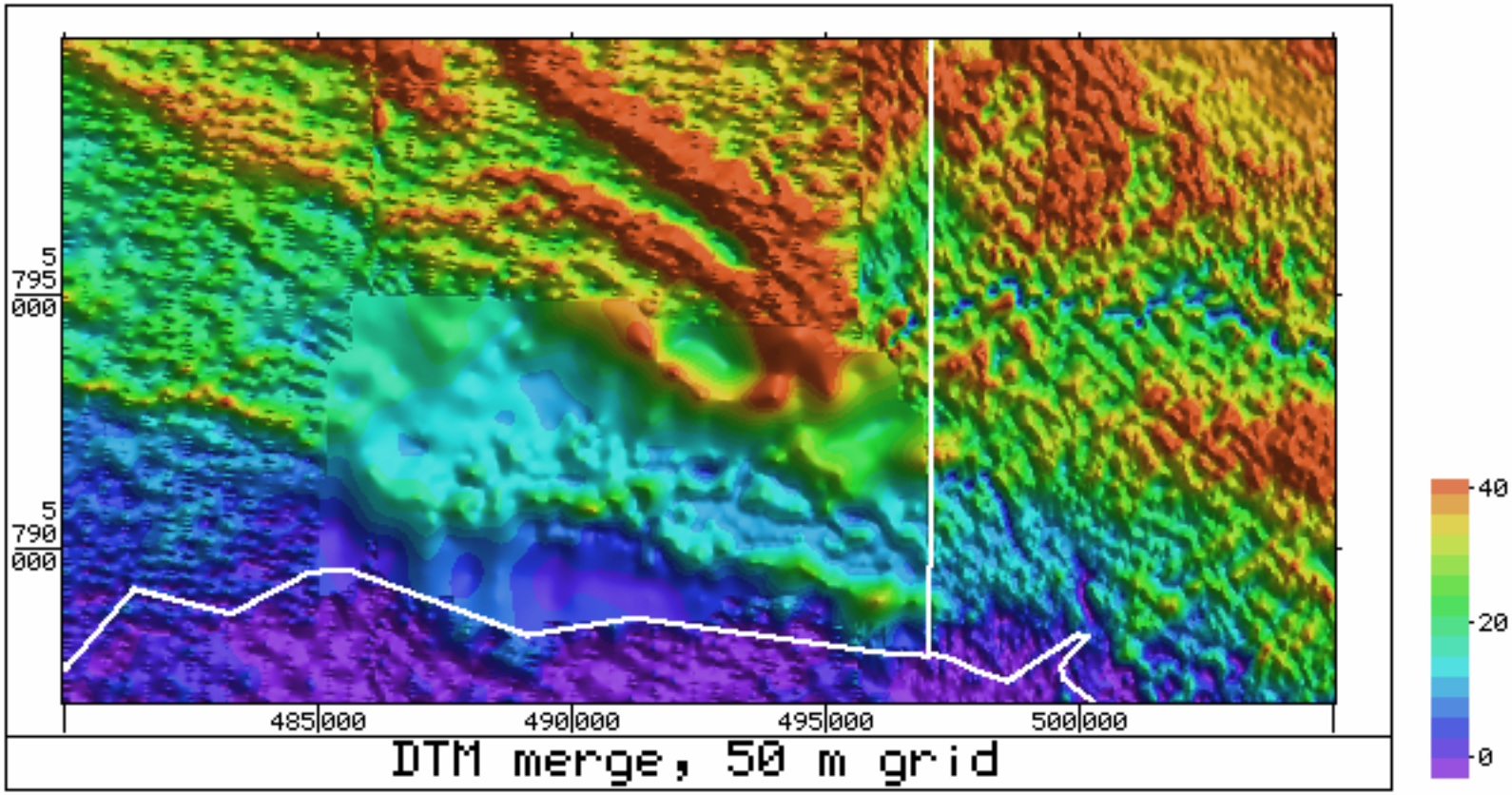

Figure 15. DTM, merged airborne and gravity elevations

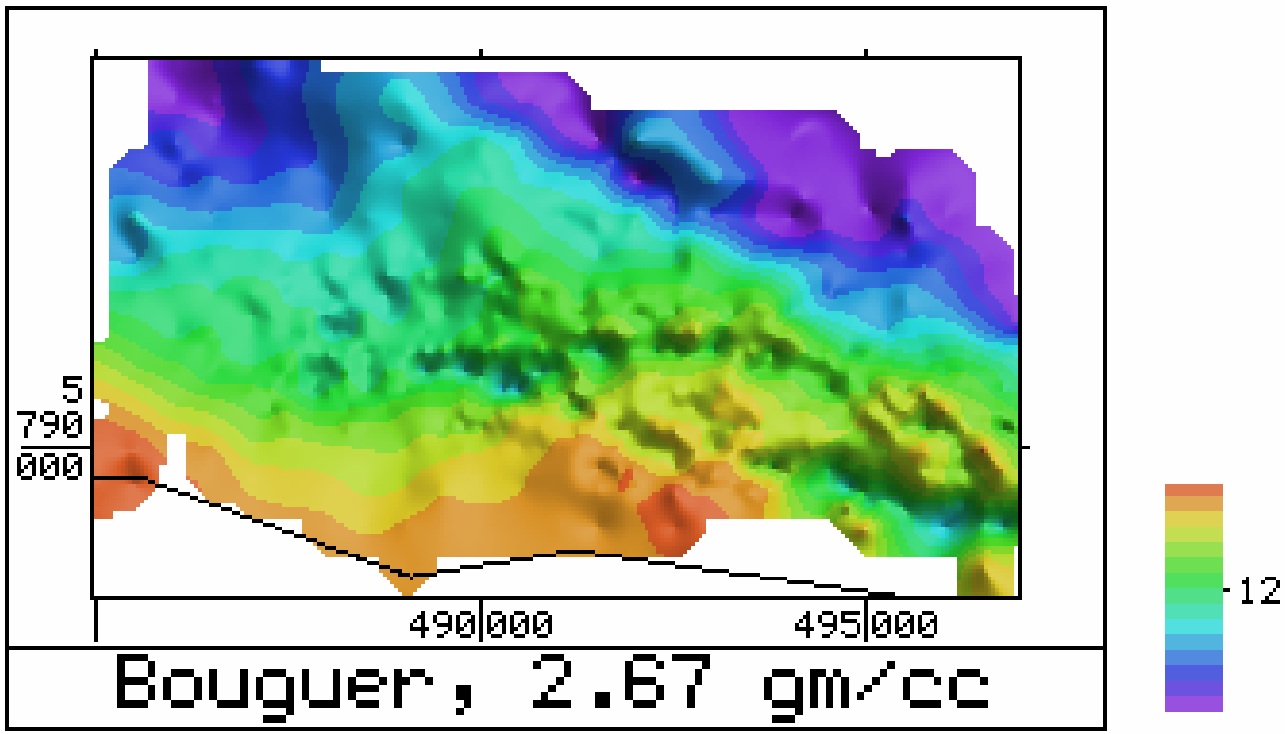

Figure 16. New survey, density 2.67 gm/cc
Colour interval 0.2 milligal

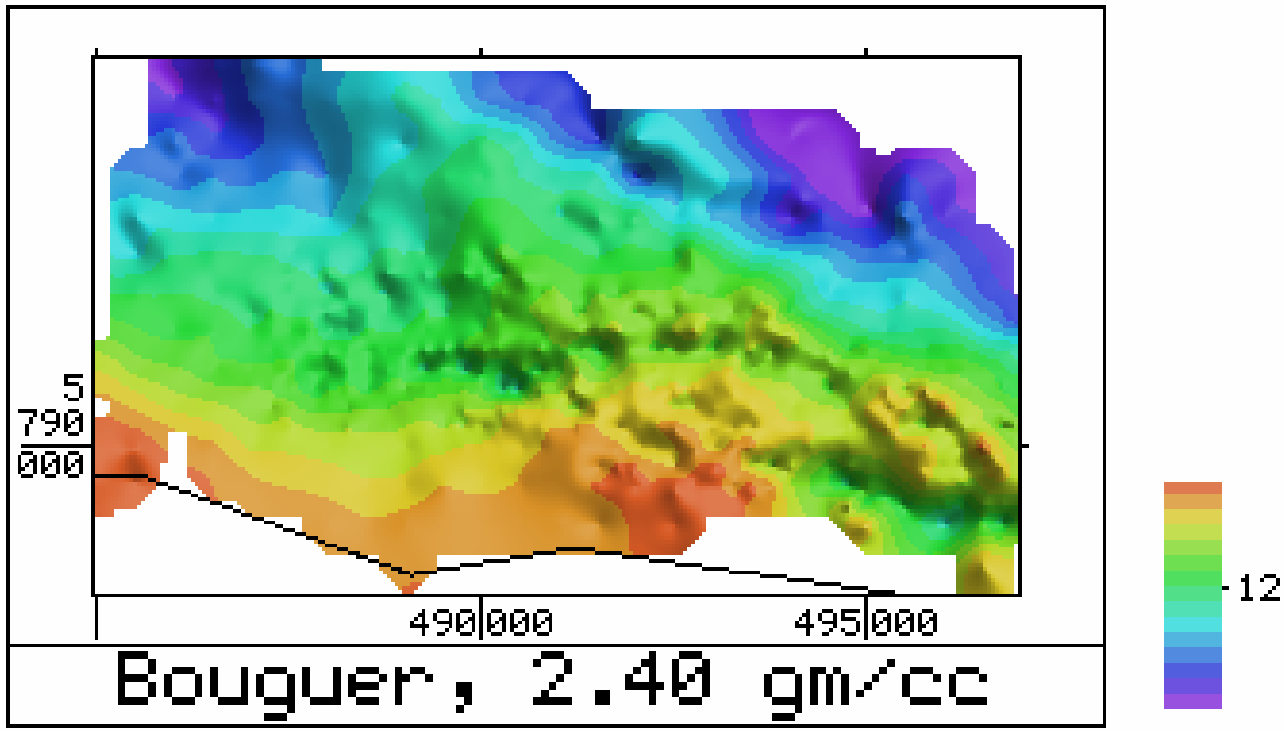

Figure 17. New survey, density 2.4 gm/cc
Colour interval 0.2 milligal

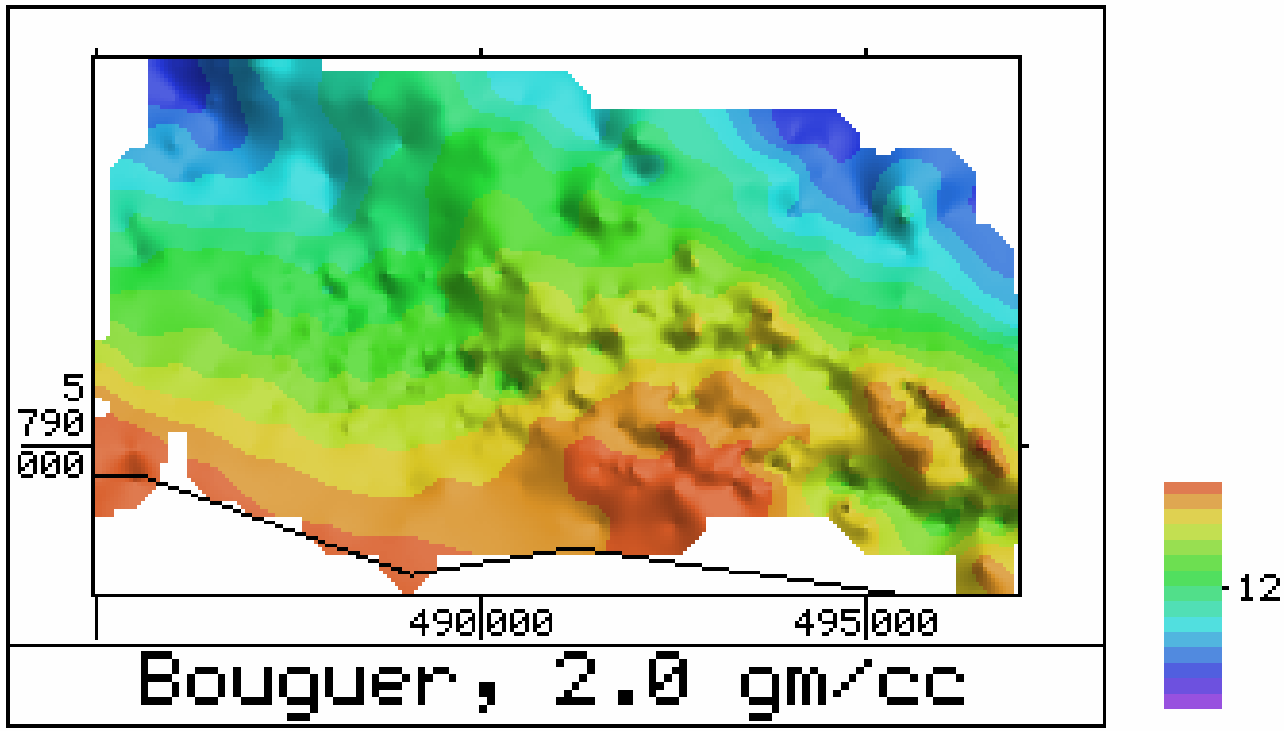

Figure 18. New survey, density 2.0 gm/cc
Colour interval 0.2 milligal

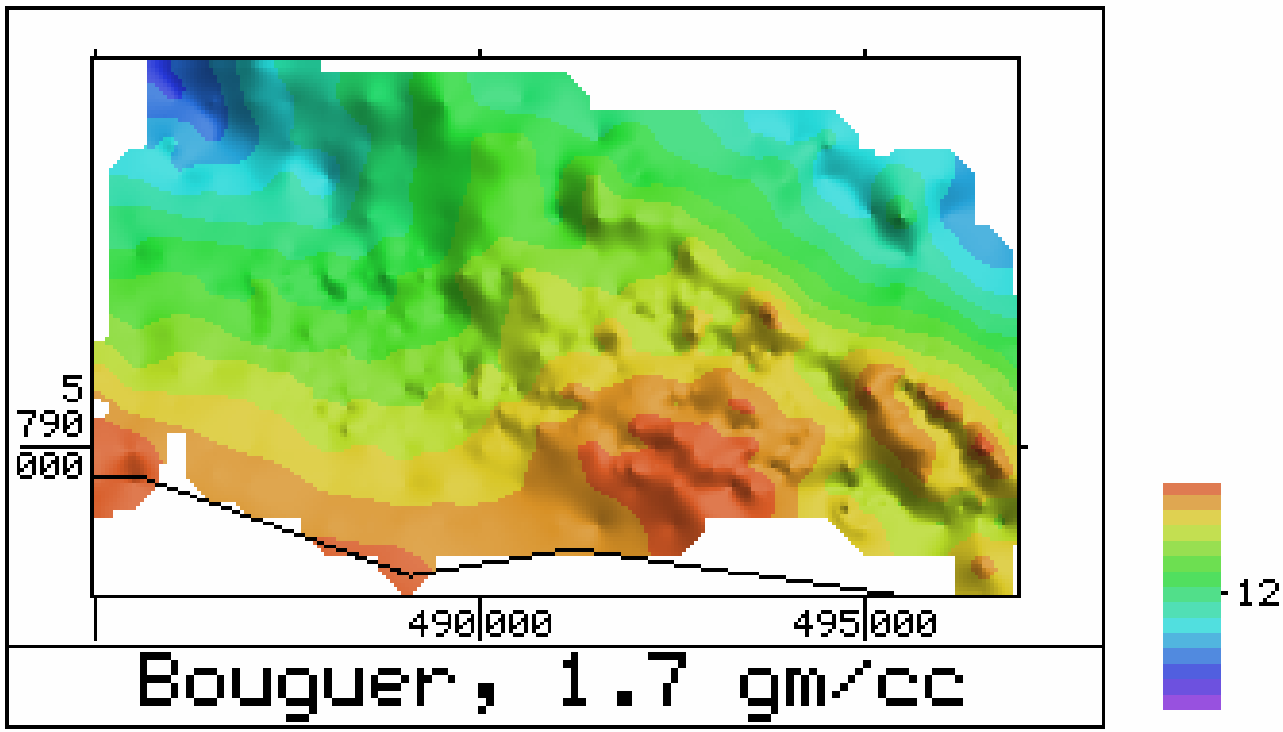

Figure 19. New survey, density 1.7 gm/cc
Colour interval 0.2 milligal

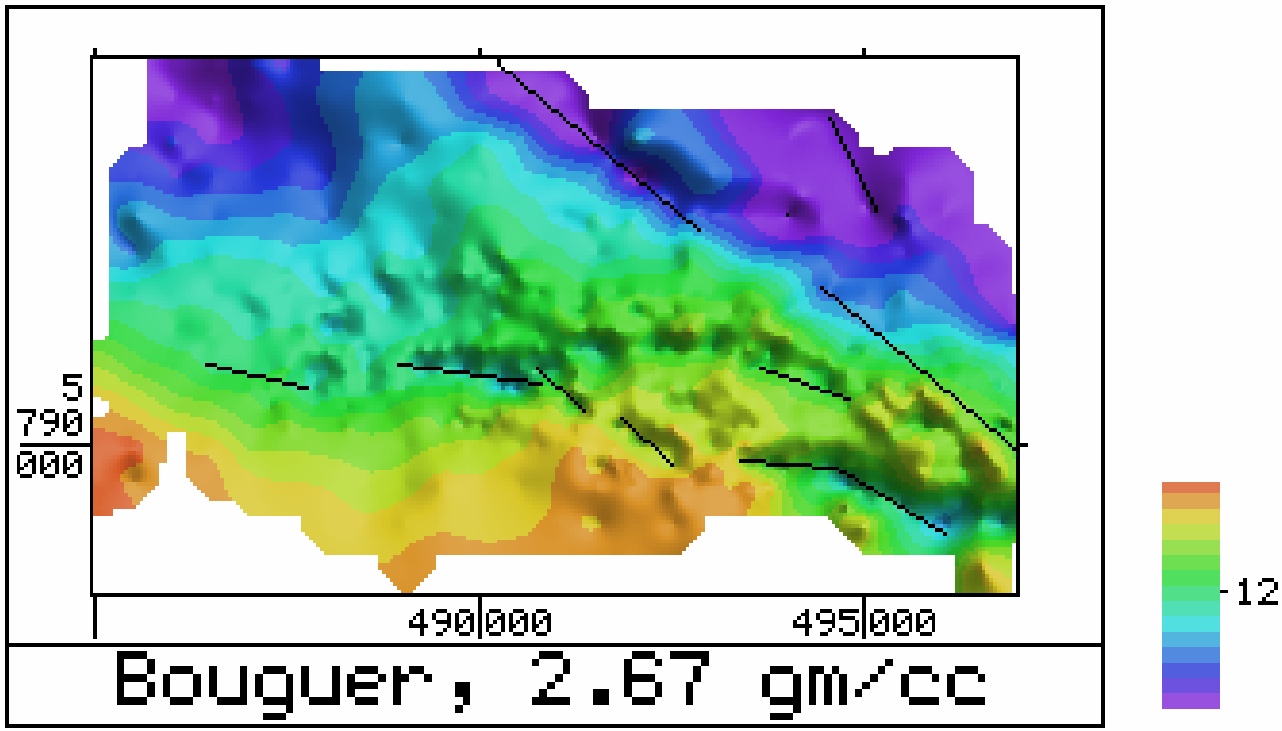

Figure 20. New survey, density 2.67 gm/cc, showing elevation peaks

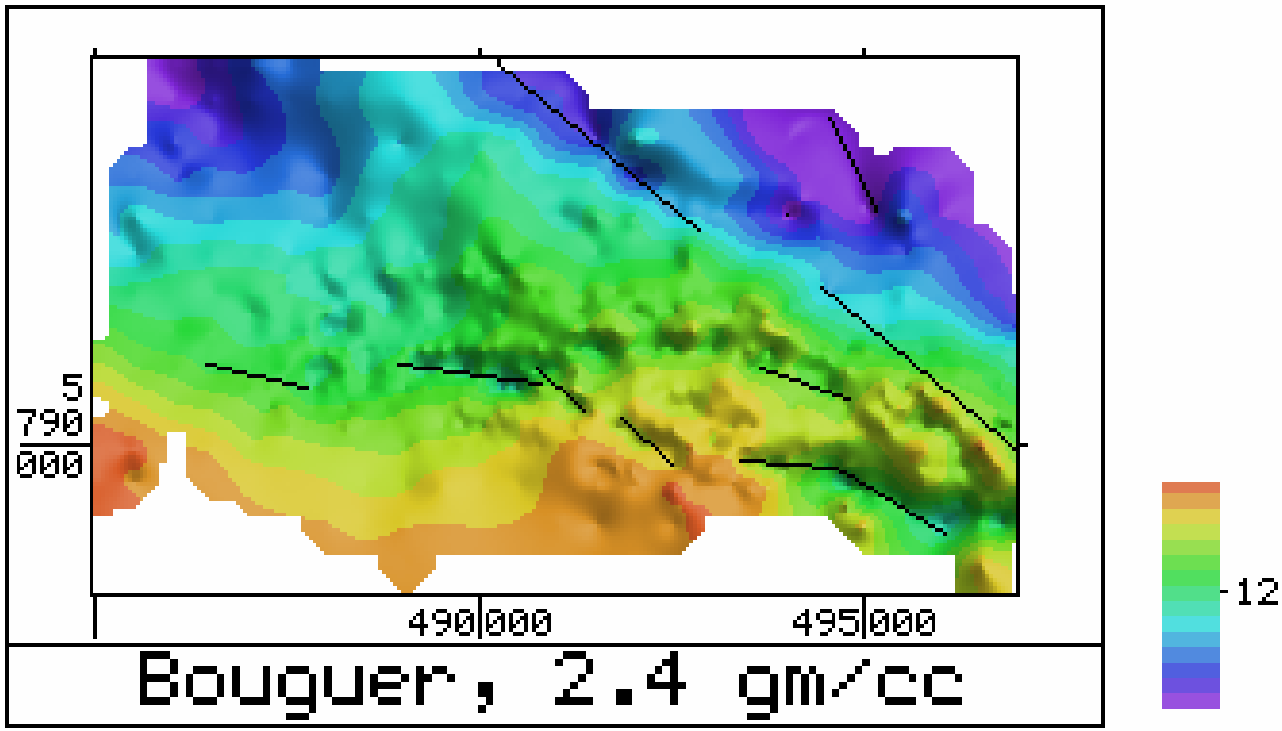

Figure 21. New survey, density 2.4 gm/cc, showing elevation peaks

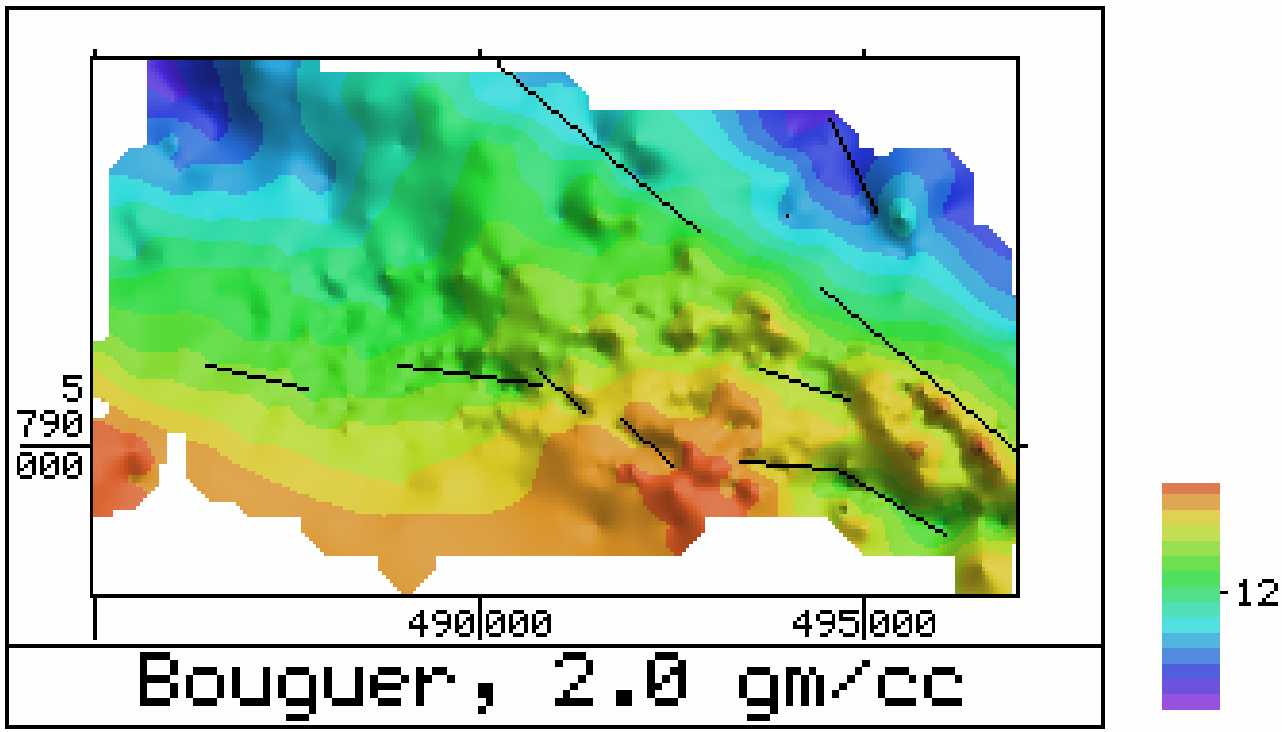

Figure 22. New survey, density 2.0 gm/cc, showing elevation peaks

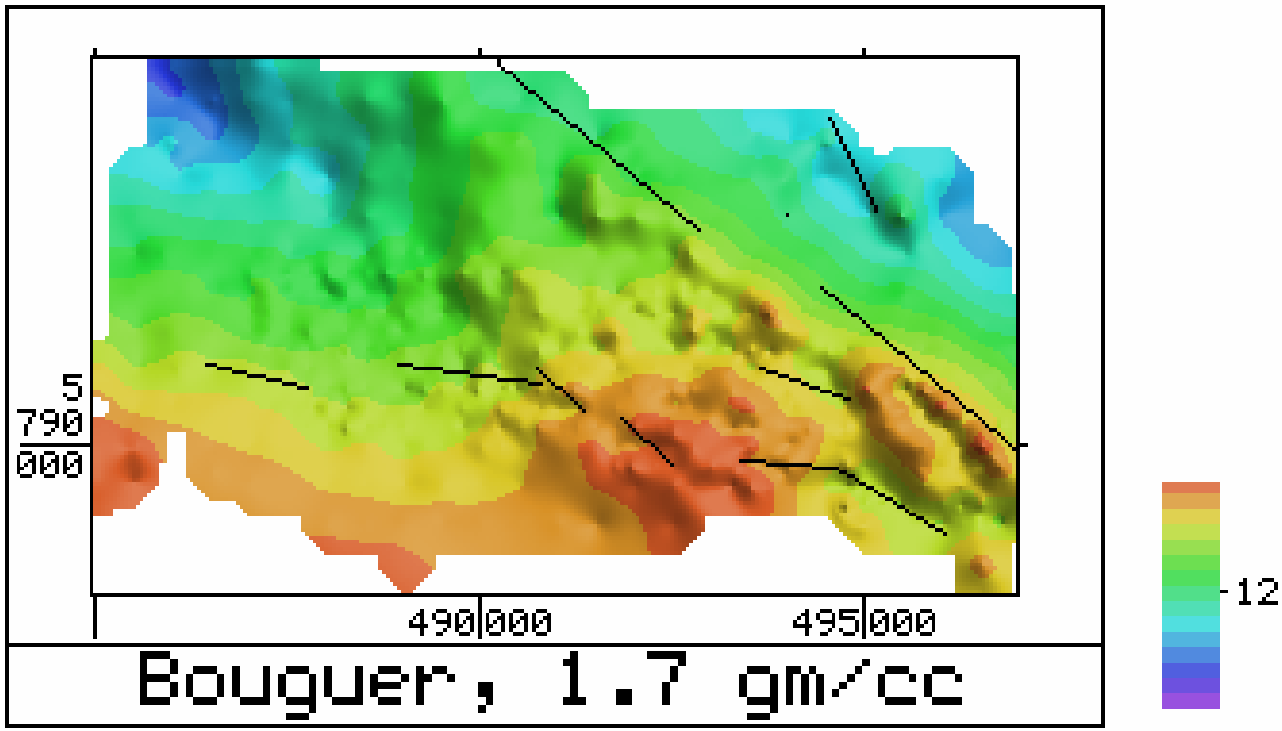

Figure 23. New survey, density 1.7 gm/cc, showing elevation peaks

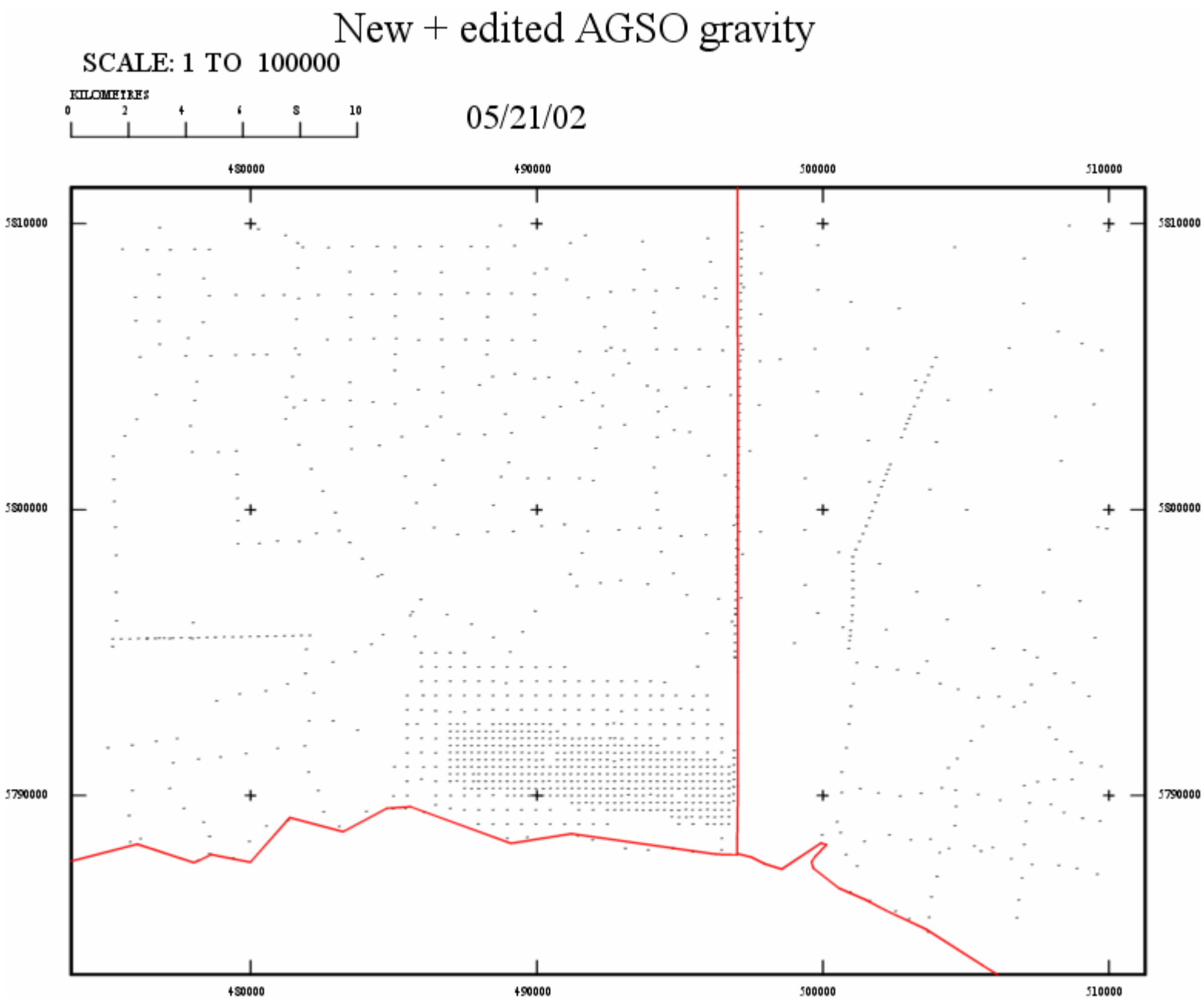

Figure 24 – Gravity Stations Locations, Merged Survey & Existing Data

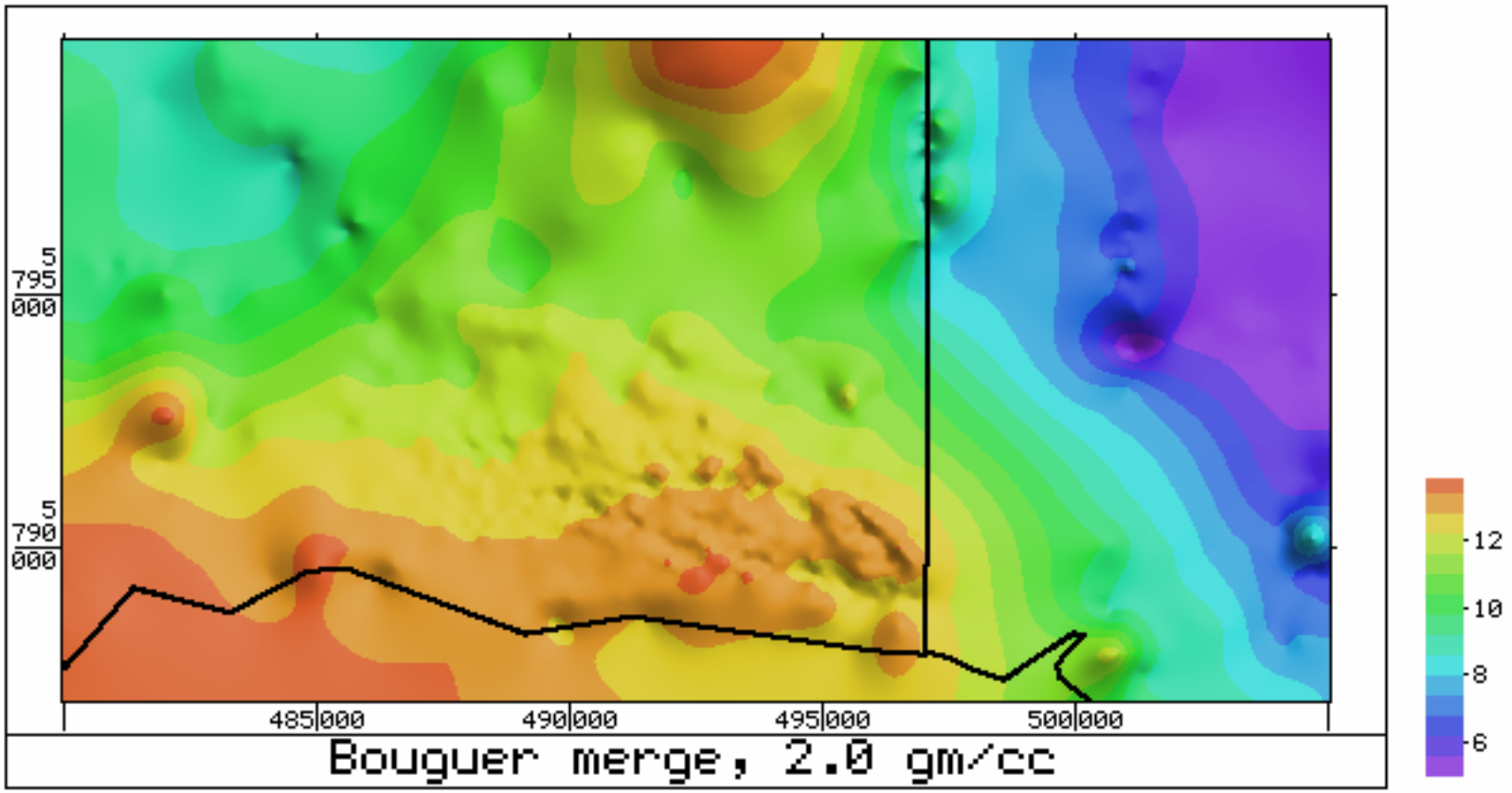

Figure 25. Merged Bouguer gravity data, 2.0 gm/cc

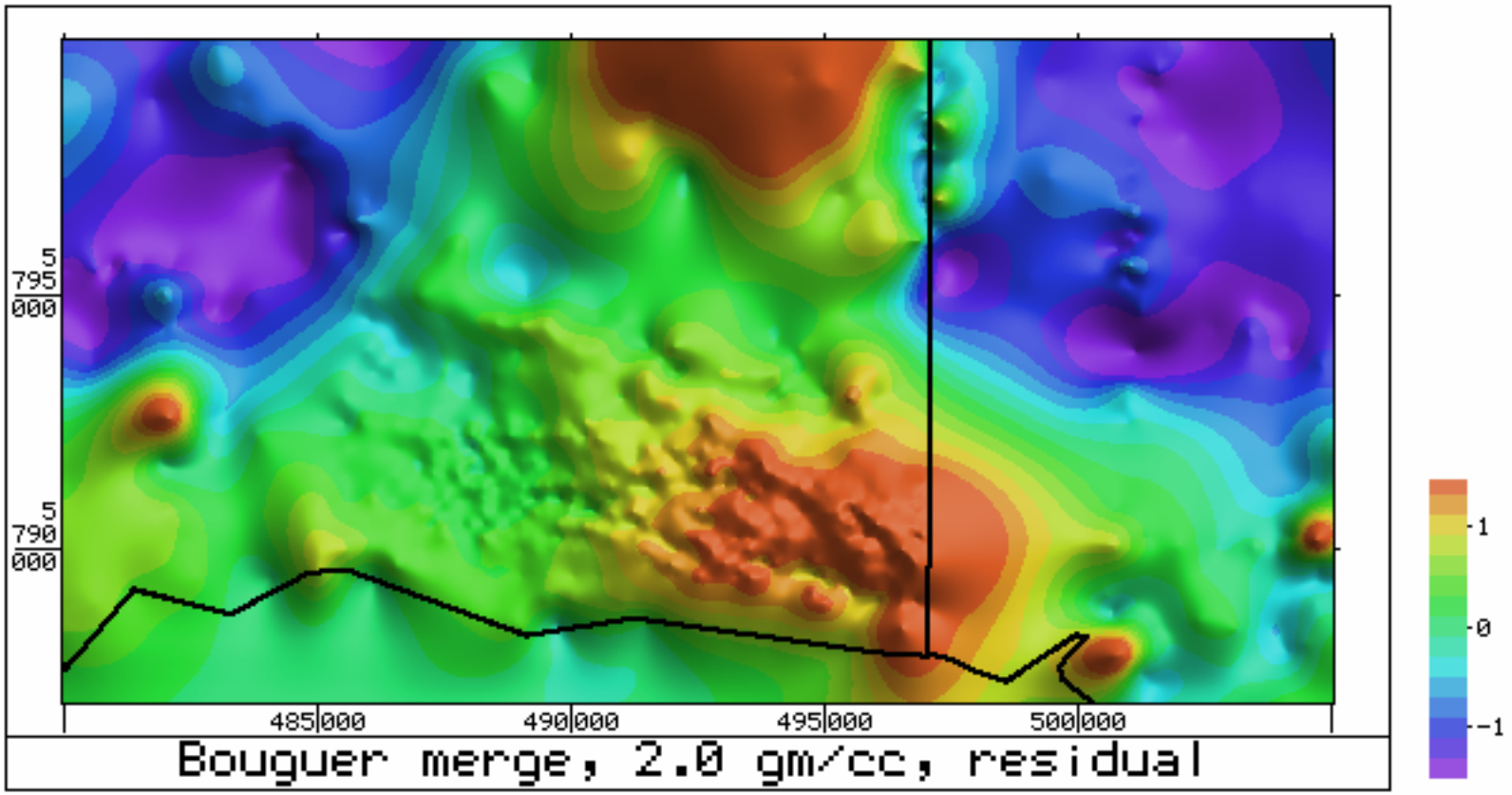

Figure 26. Merged Bouguer gravity, residual, 2.0 gm/cc

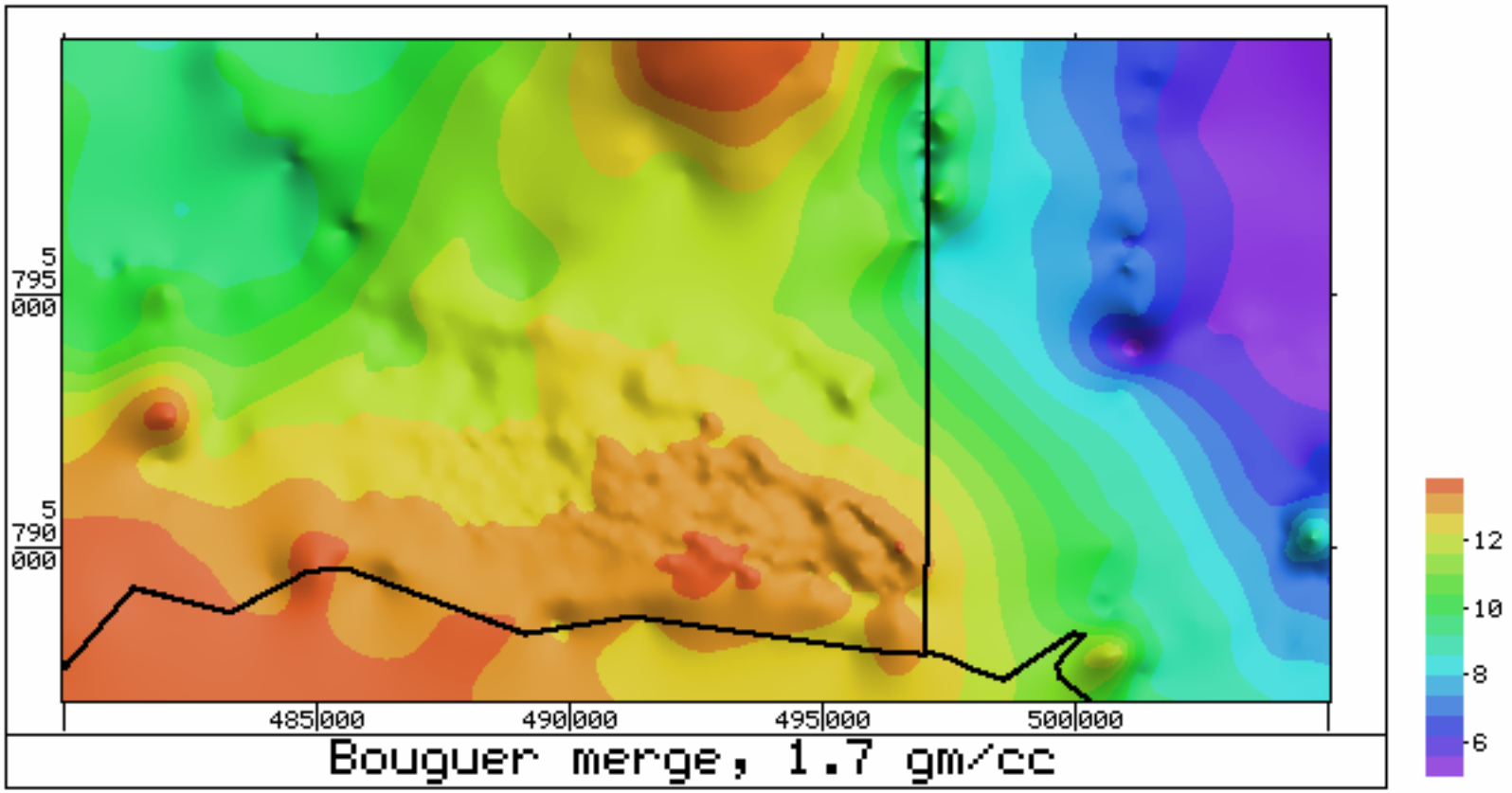

Figure 27. Merged Bouguer gravity data, 1.7 gm/cc

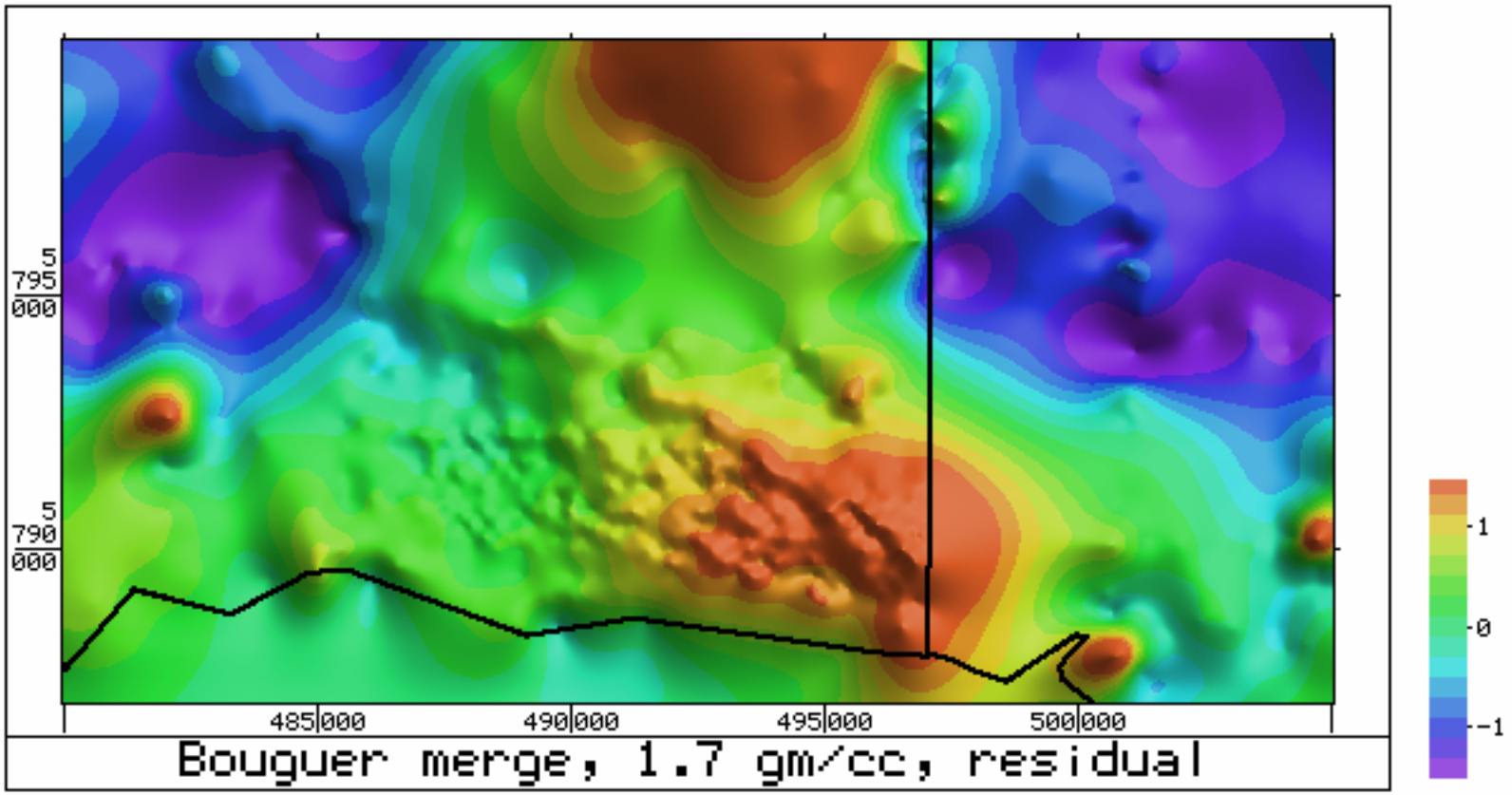

Figure 28. Merged Bouguer gravity, residual, 1.7 gm/cc

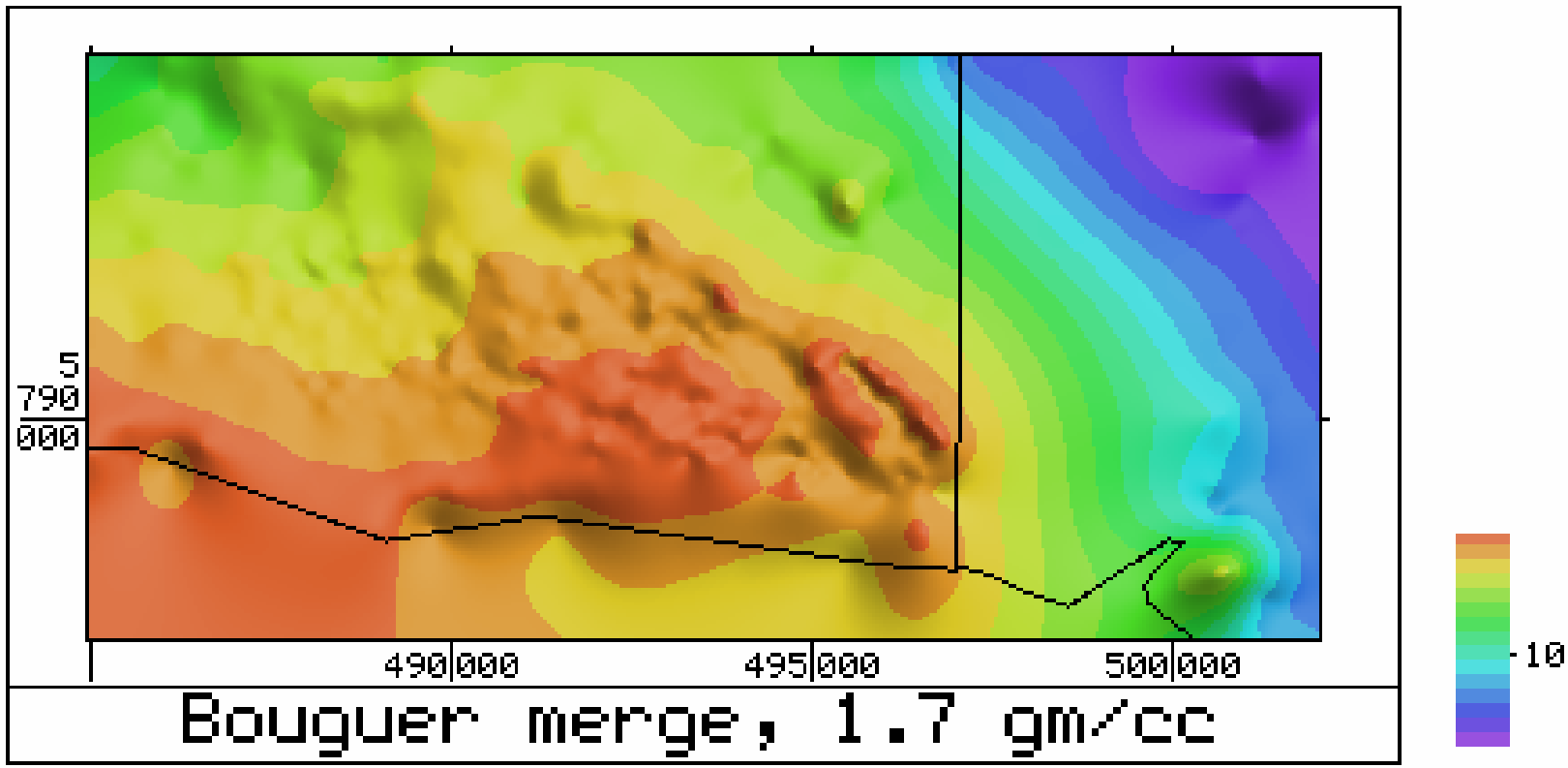

Figure 29. Bouguer gravity, 1.7 gm/cc, colour interval 0.4 mgal

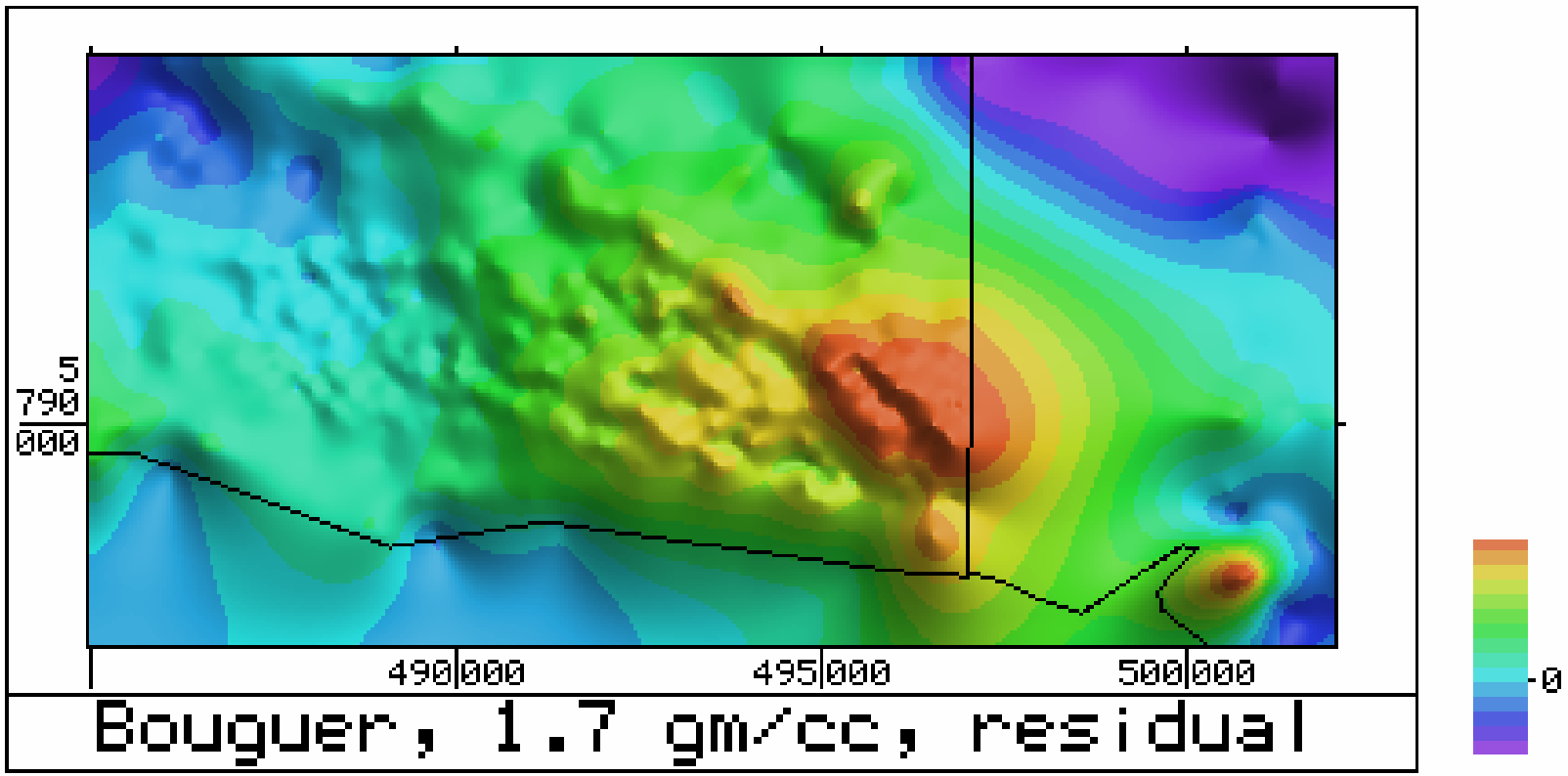

Figure 30. Bouguer gravity, 1.7 gm/cc, residual, colour interval 0.2 mgal

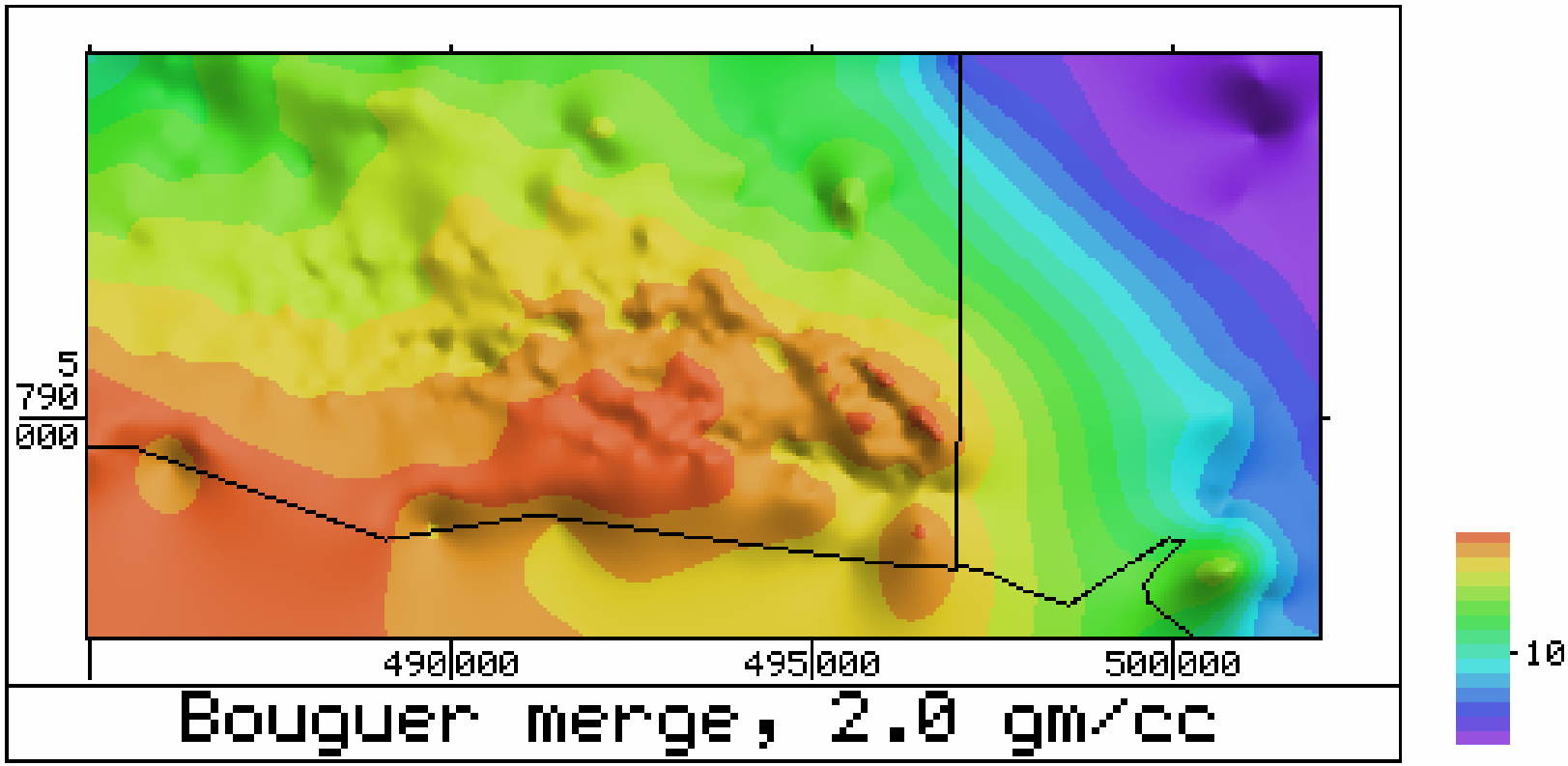

Figure 31. Bouguer gravity, 2.0 gm/cc, colour interval 0.4 mgal

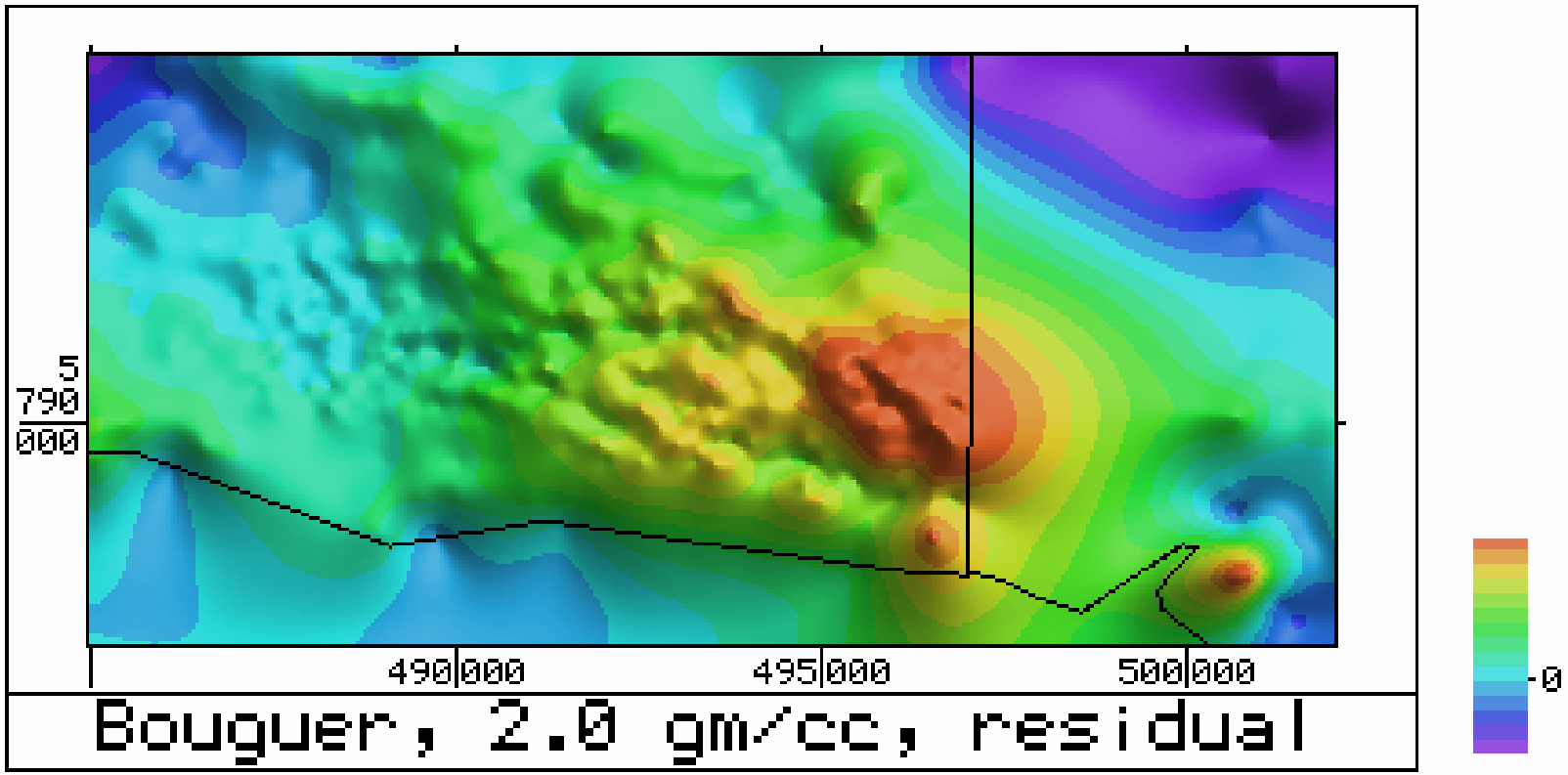

Figure 32. Bouguer gravity, 2.0 gm/cc, residual, colour interval 0.2 mgal

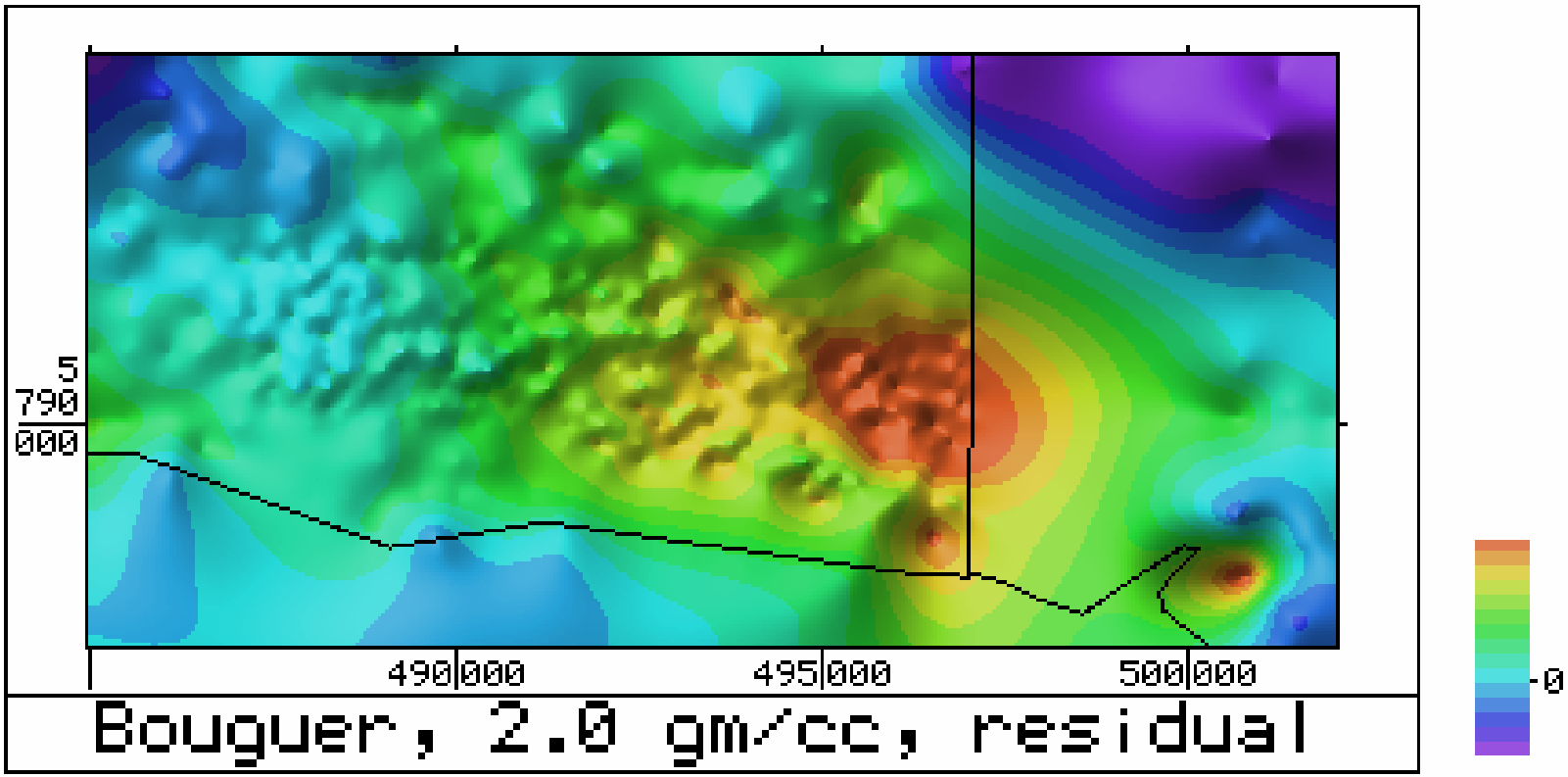

Figure 33. Bouguer gravity, 2.0 gm/cc, residual, illumination from SE

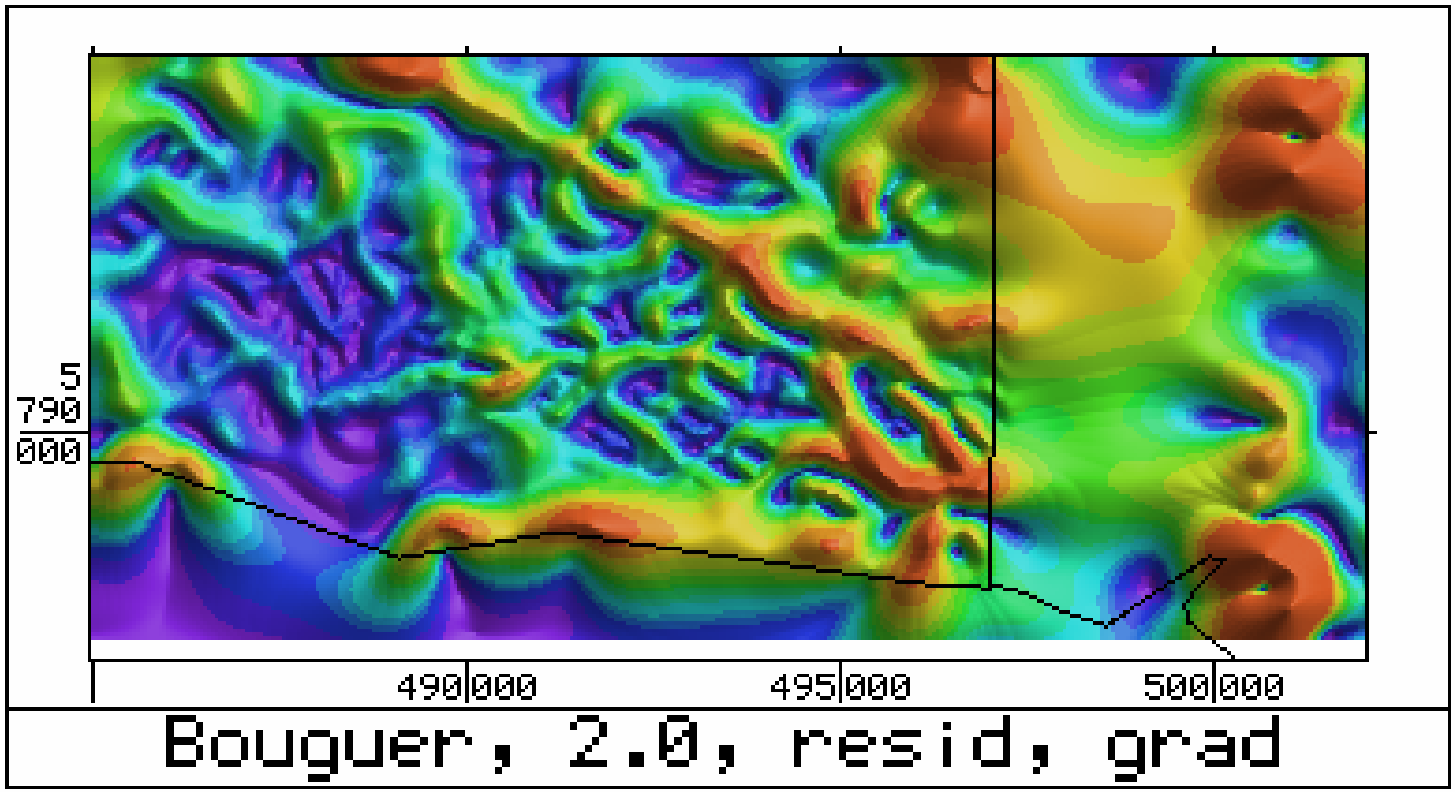

Figure 34. Bouguer gravity, 2.0 gm/cc, horizontal gradient

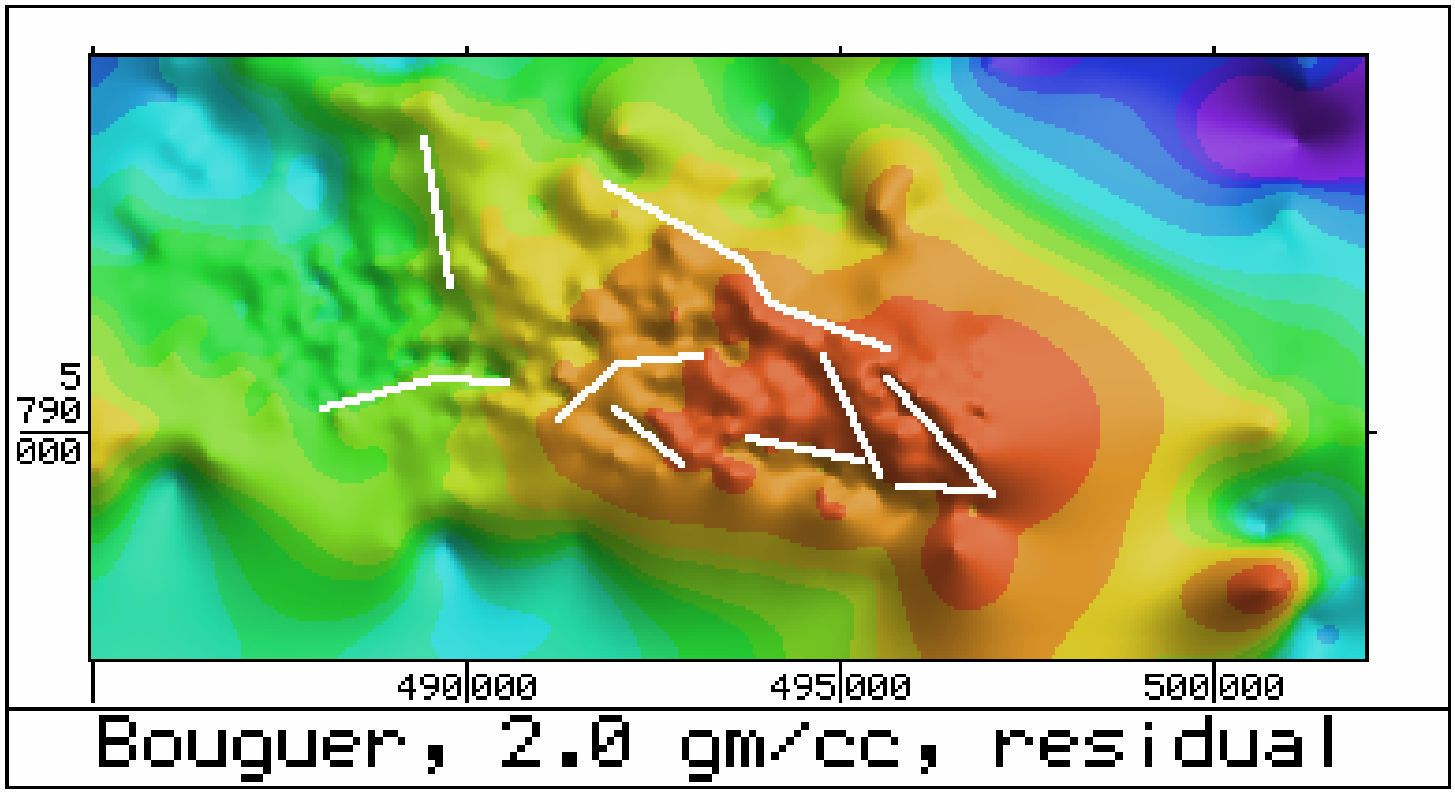

Figure 35. Bouguer gravity, 2.0 gm/cc, residual, with gradient lineations

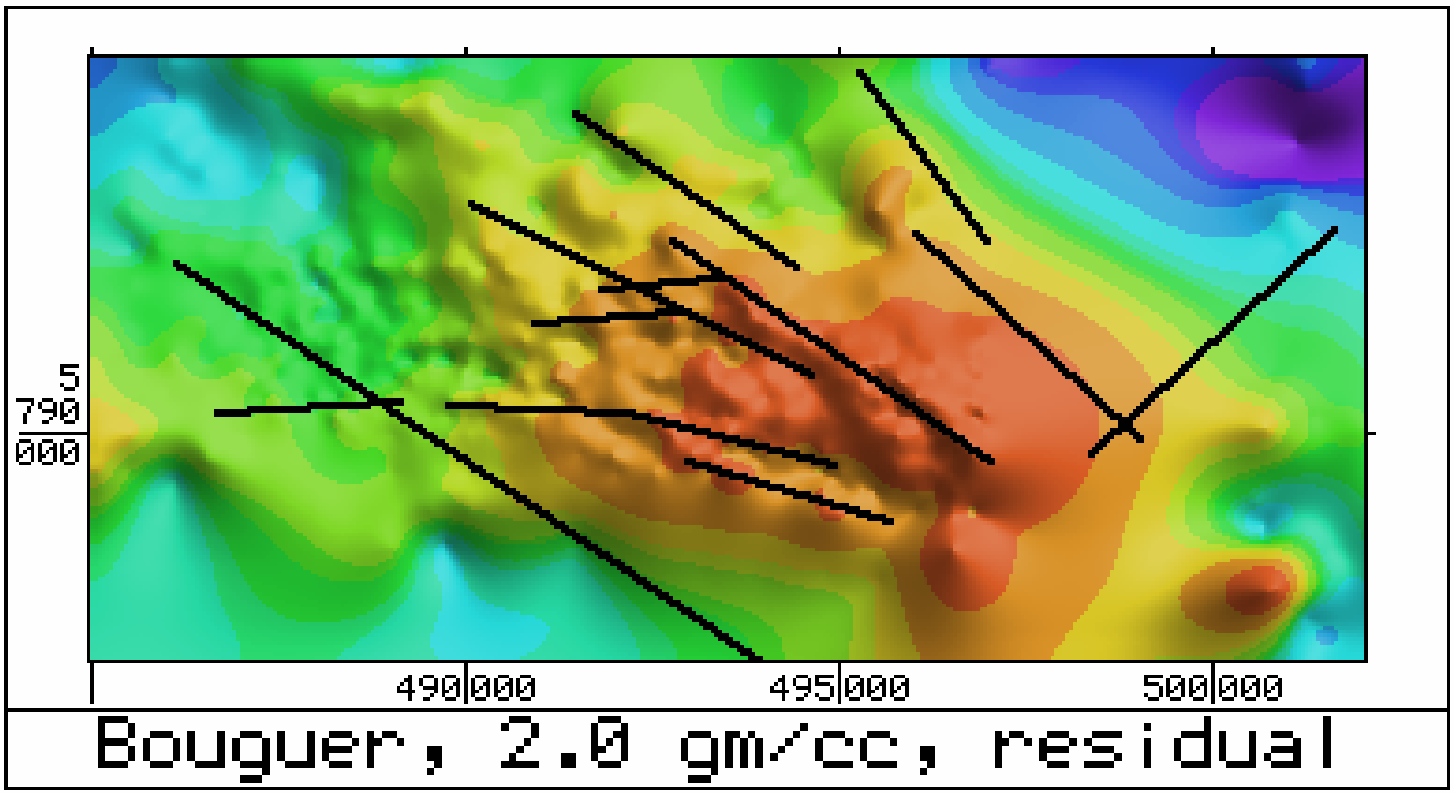

Figure 36. Bouguer gravity, 2.0 gm/cc, residual, with magnetic lineations

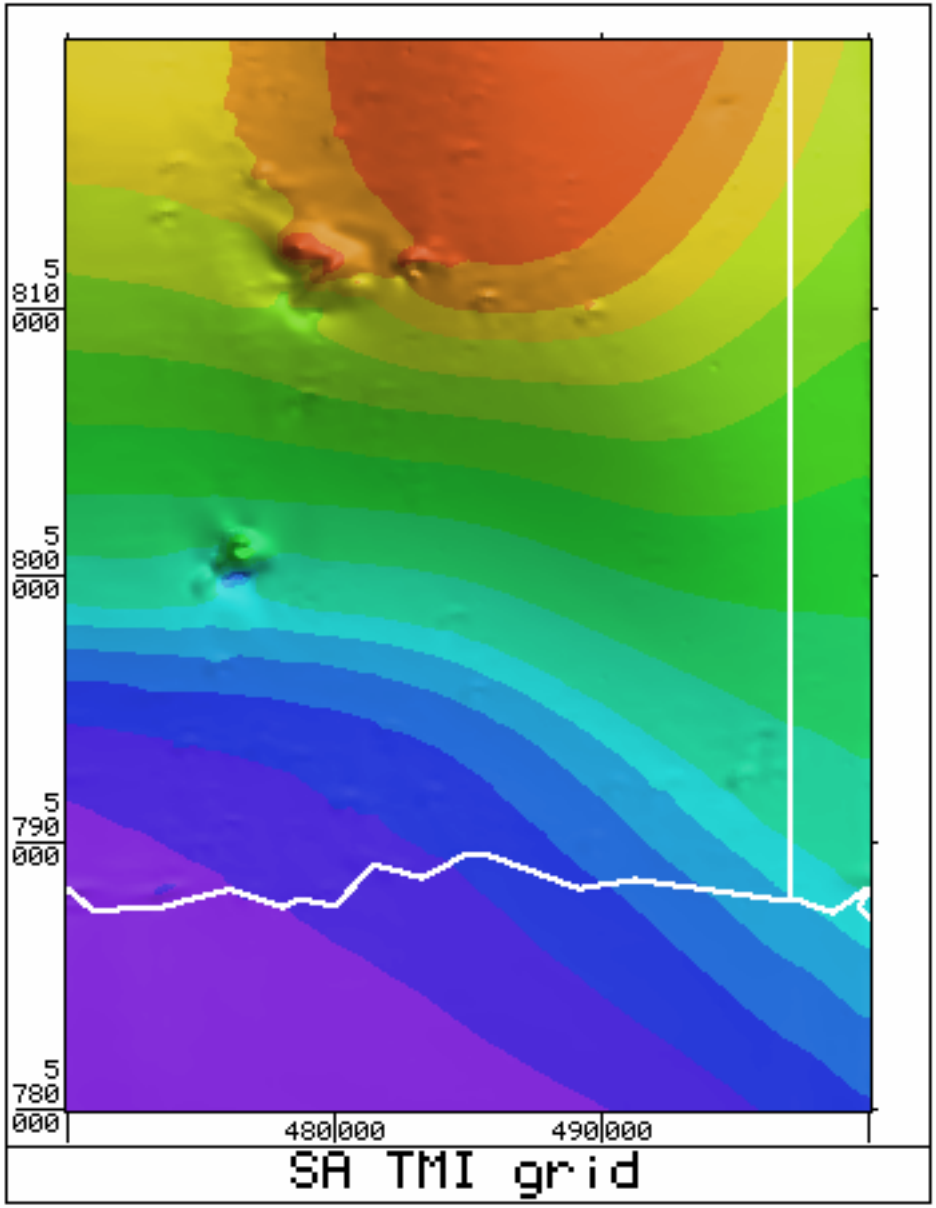

Figure 37. TMI, from S.A. 200 m grid

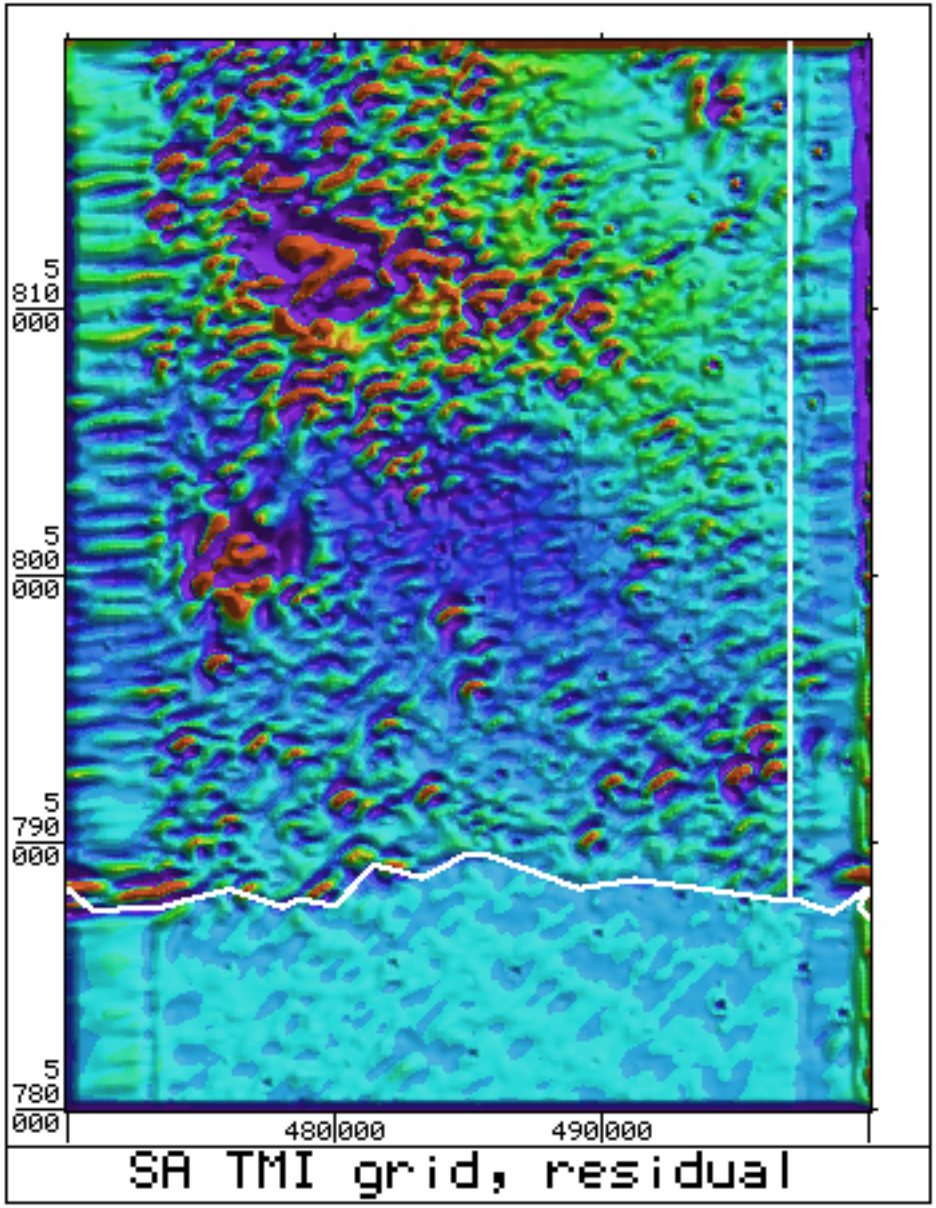

Figure 38. TMI residual, from S.A. grid

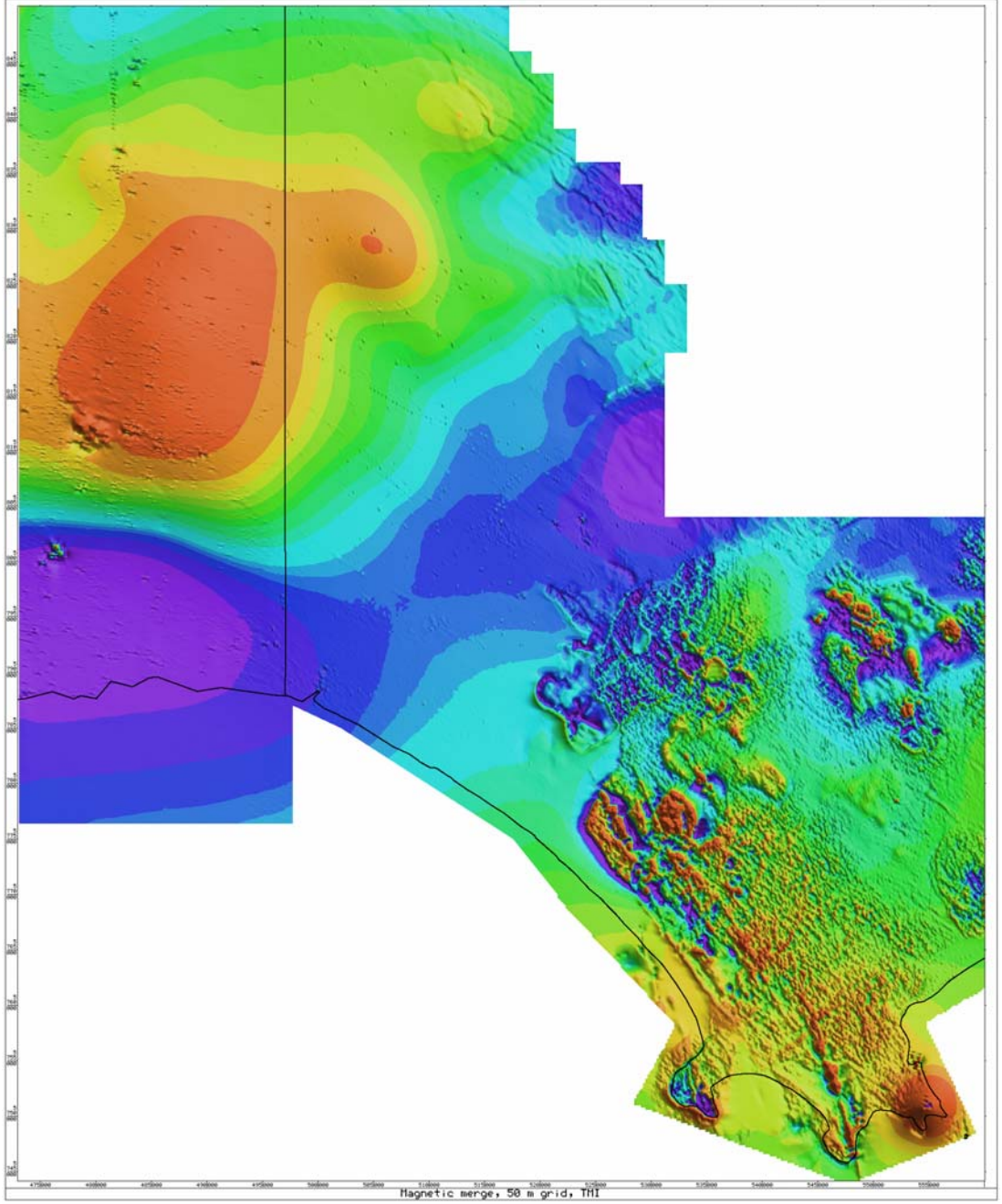

Figure 39. TMI, levelled and merged data

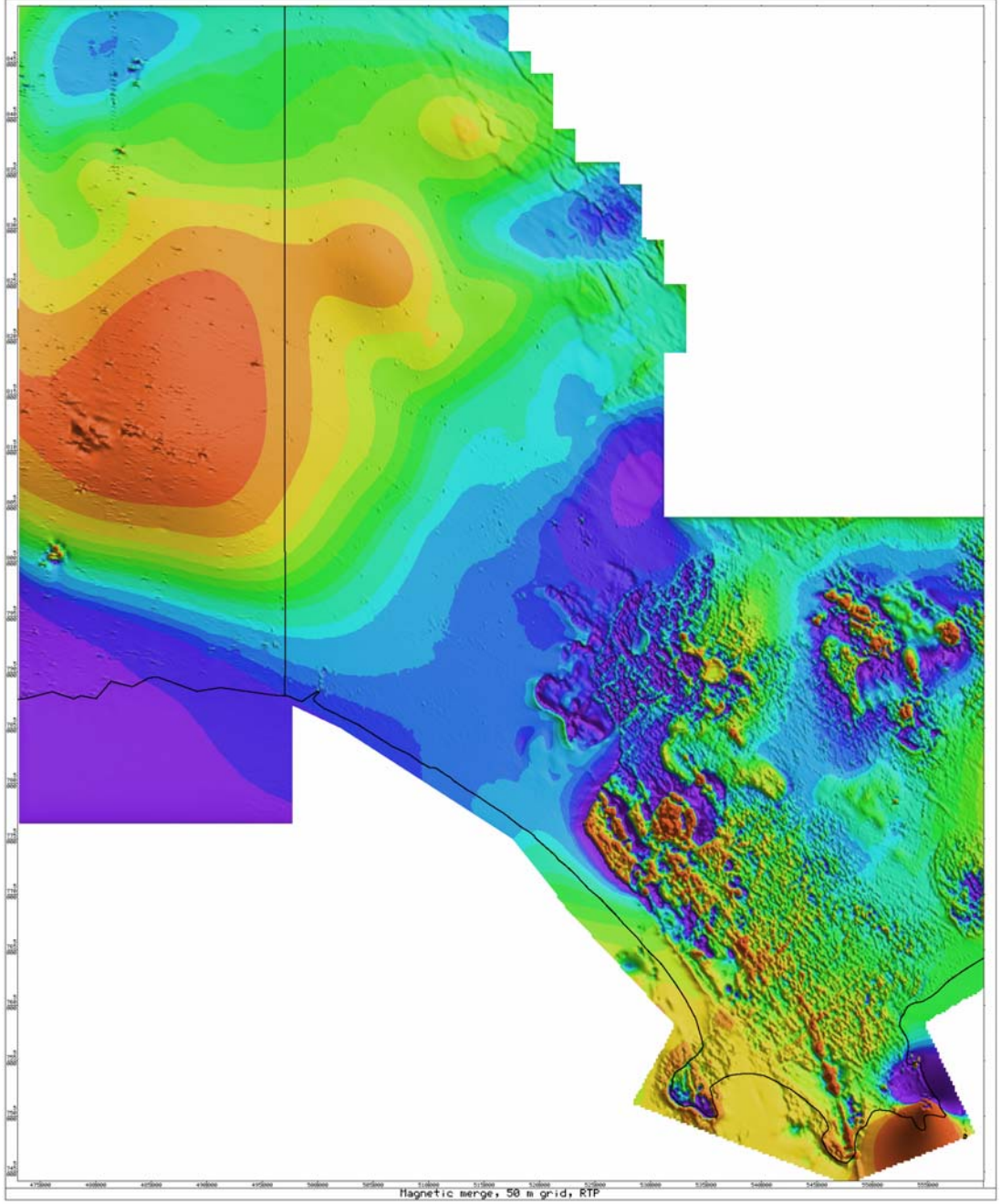

Figure 40. RTP magnetics, levelled and merged data

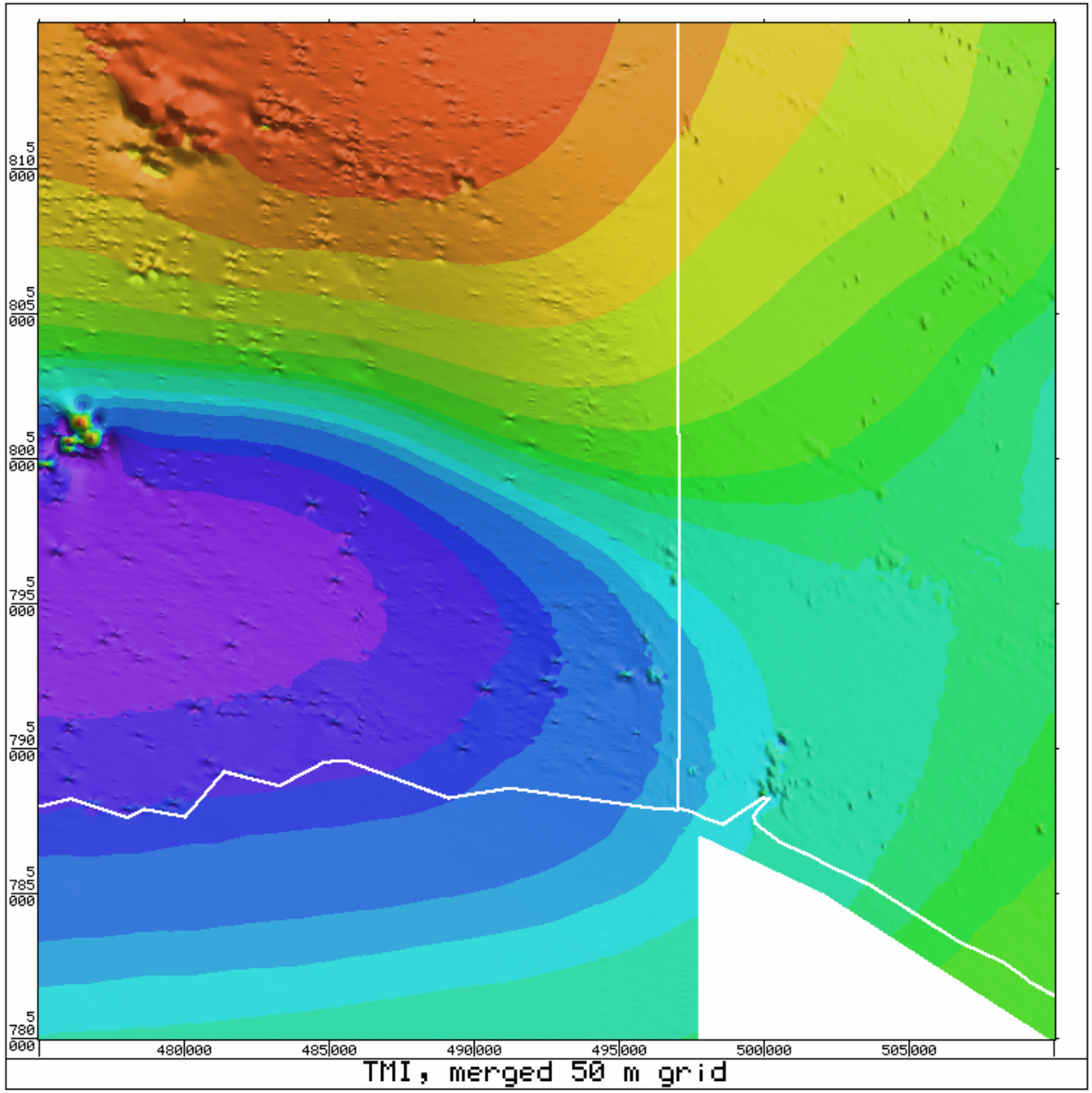

Figure 41. Total Magnetic Intensity

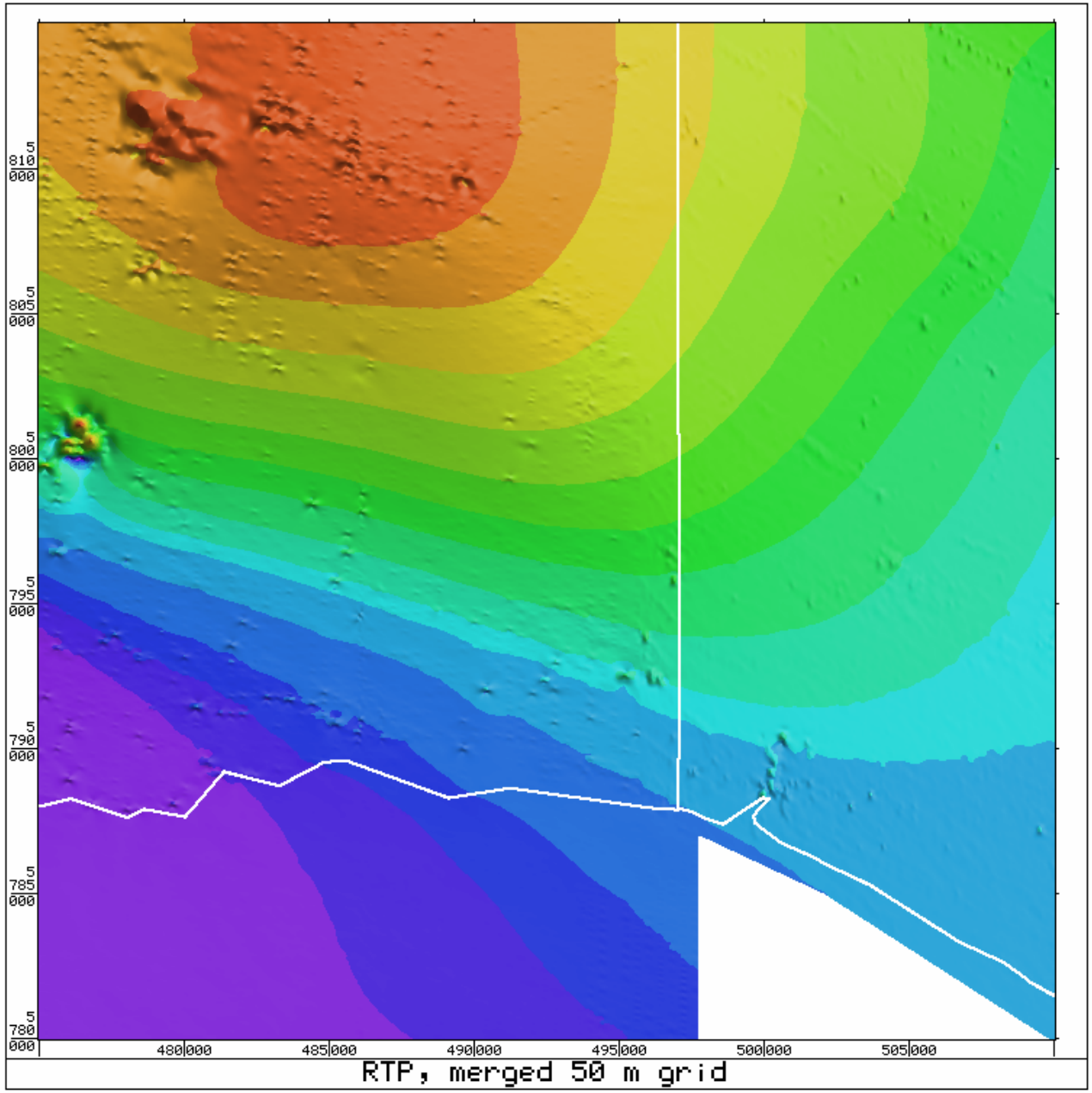

Figure 42. RTP magnetics

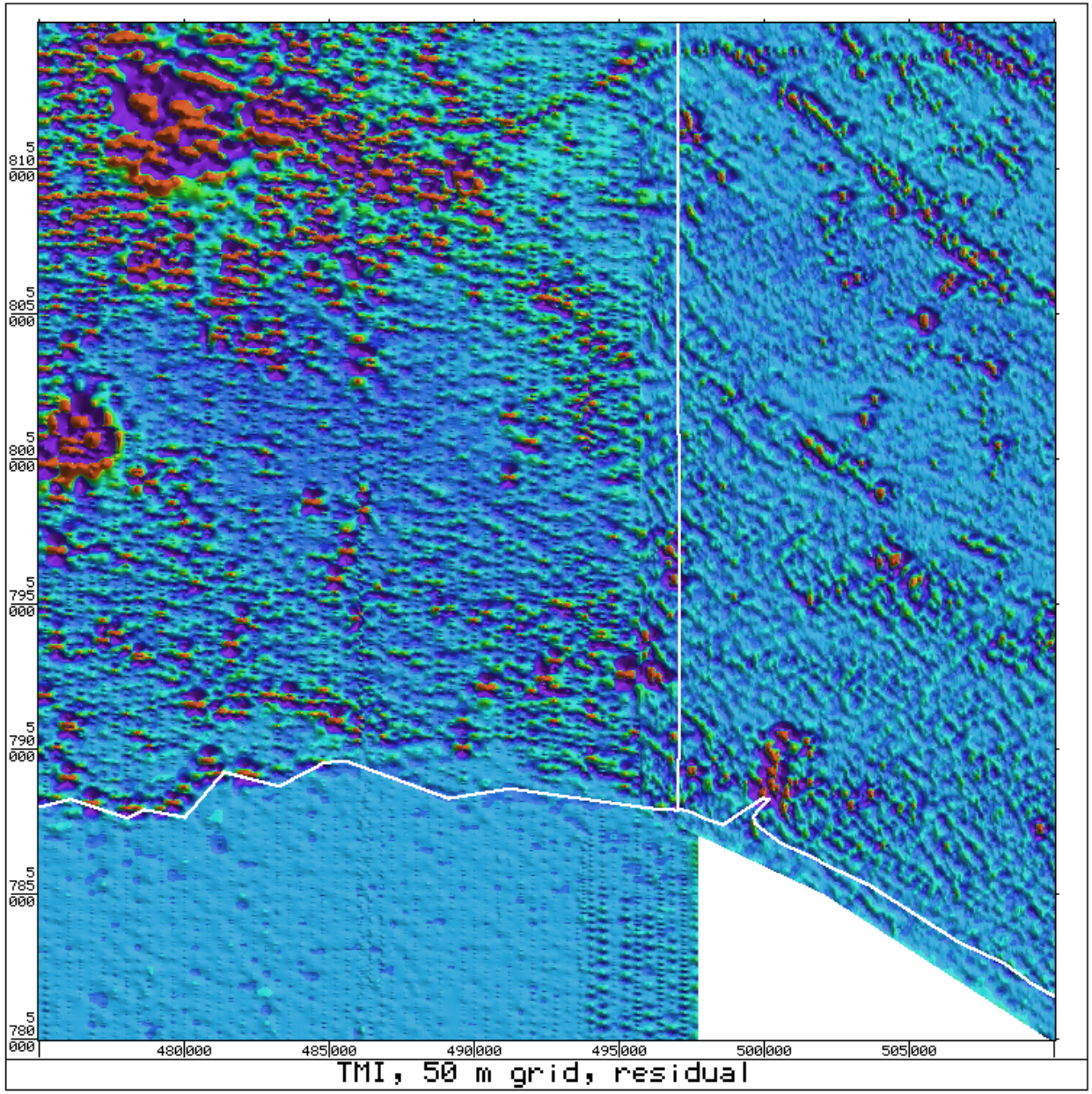

Figure 43. TMI residual, 1 km operator

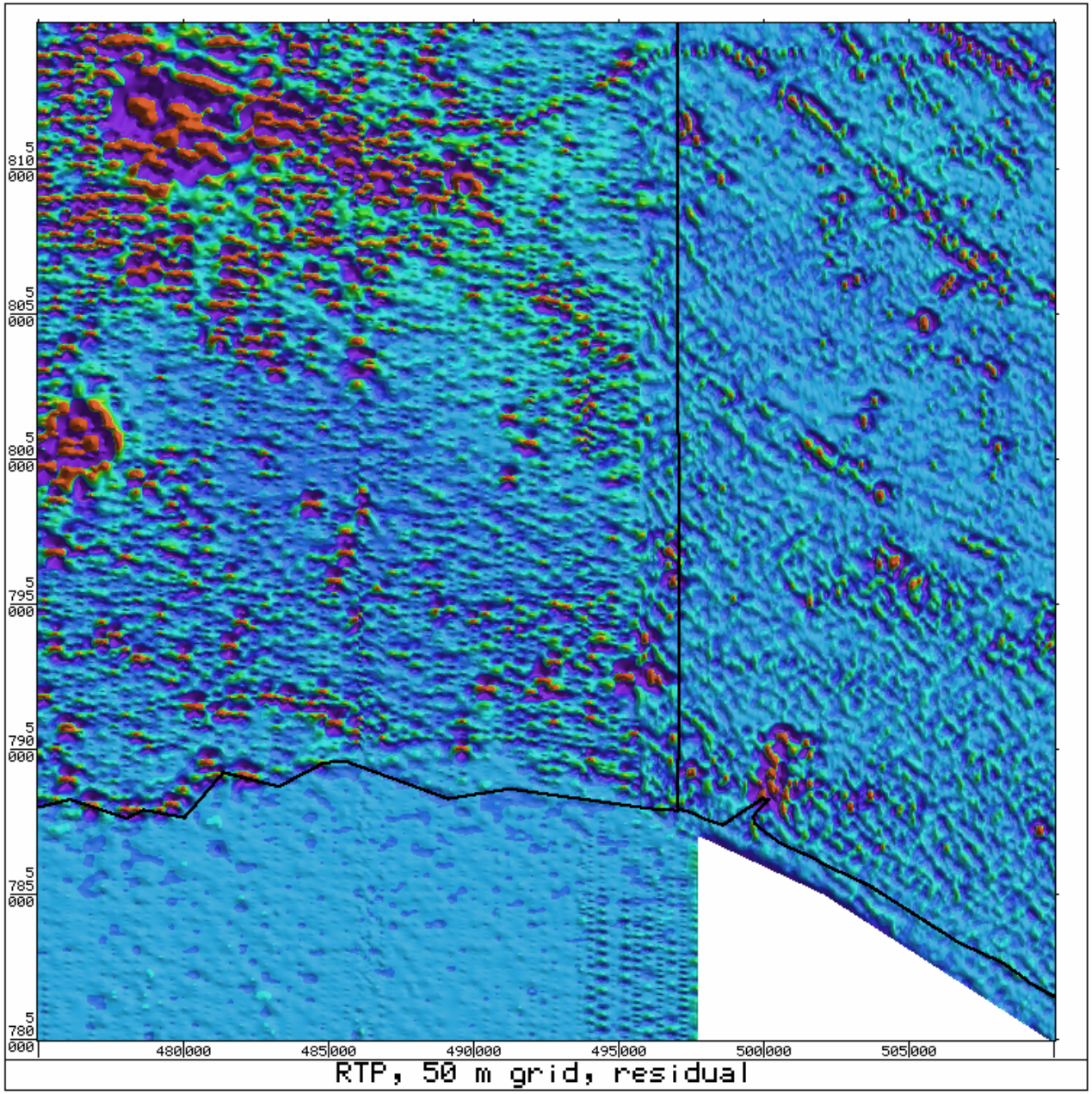

Figure 44. RTP residual, 1 km operator

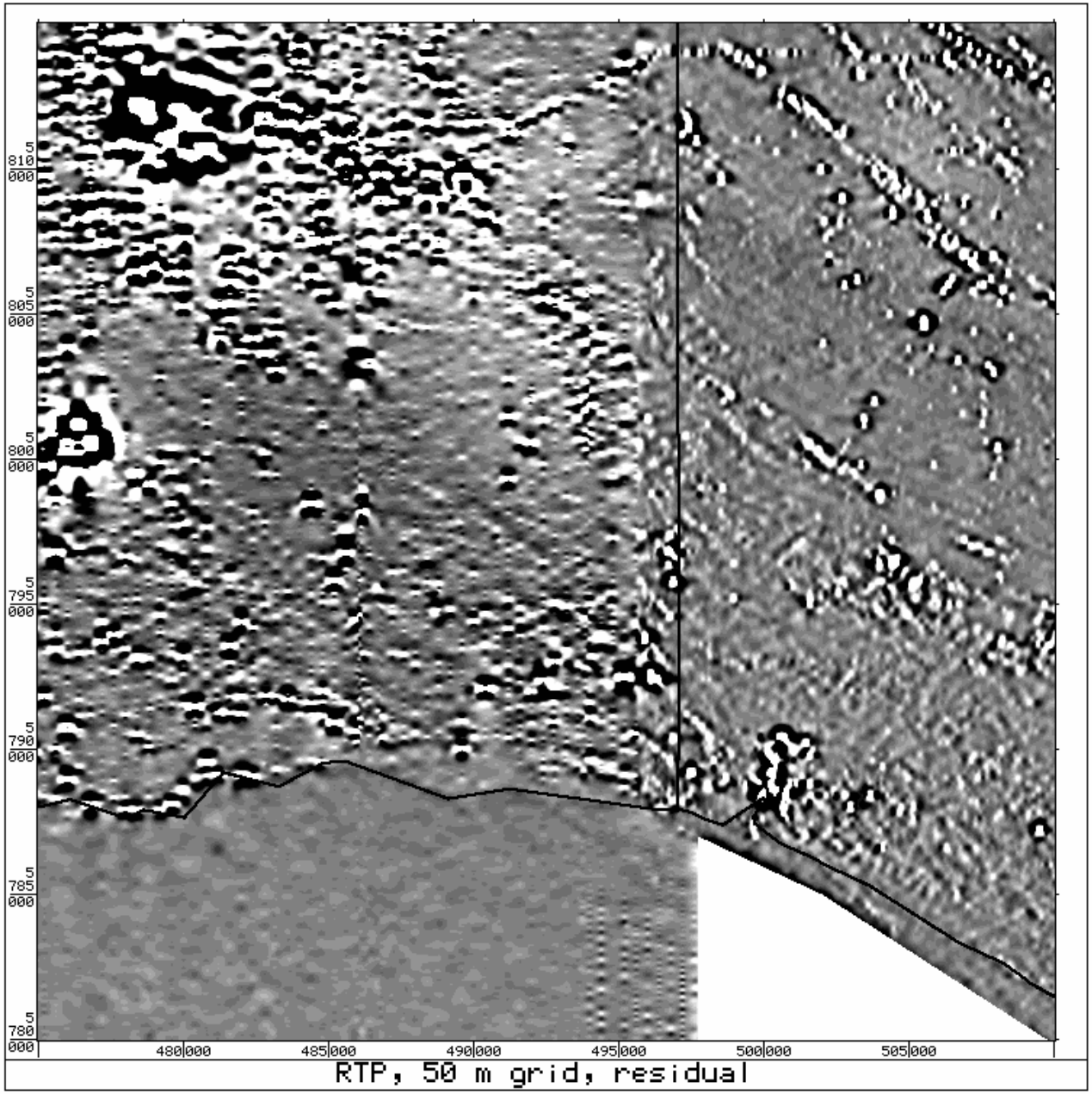

Figure 45. RTP residual, 1 km operator

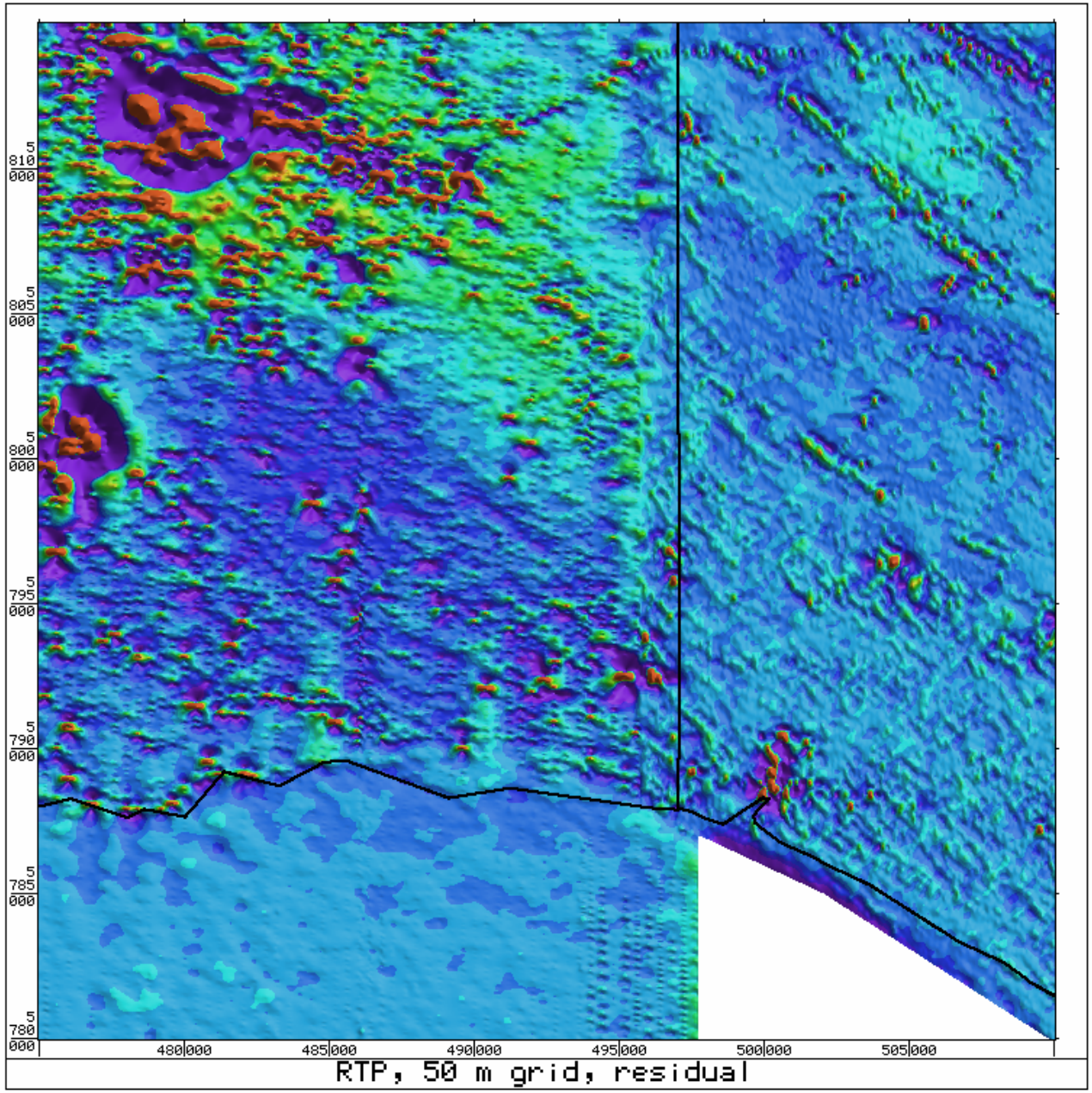

Figure 46. RTP residual, 2.5 km operator

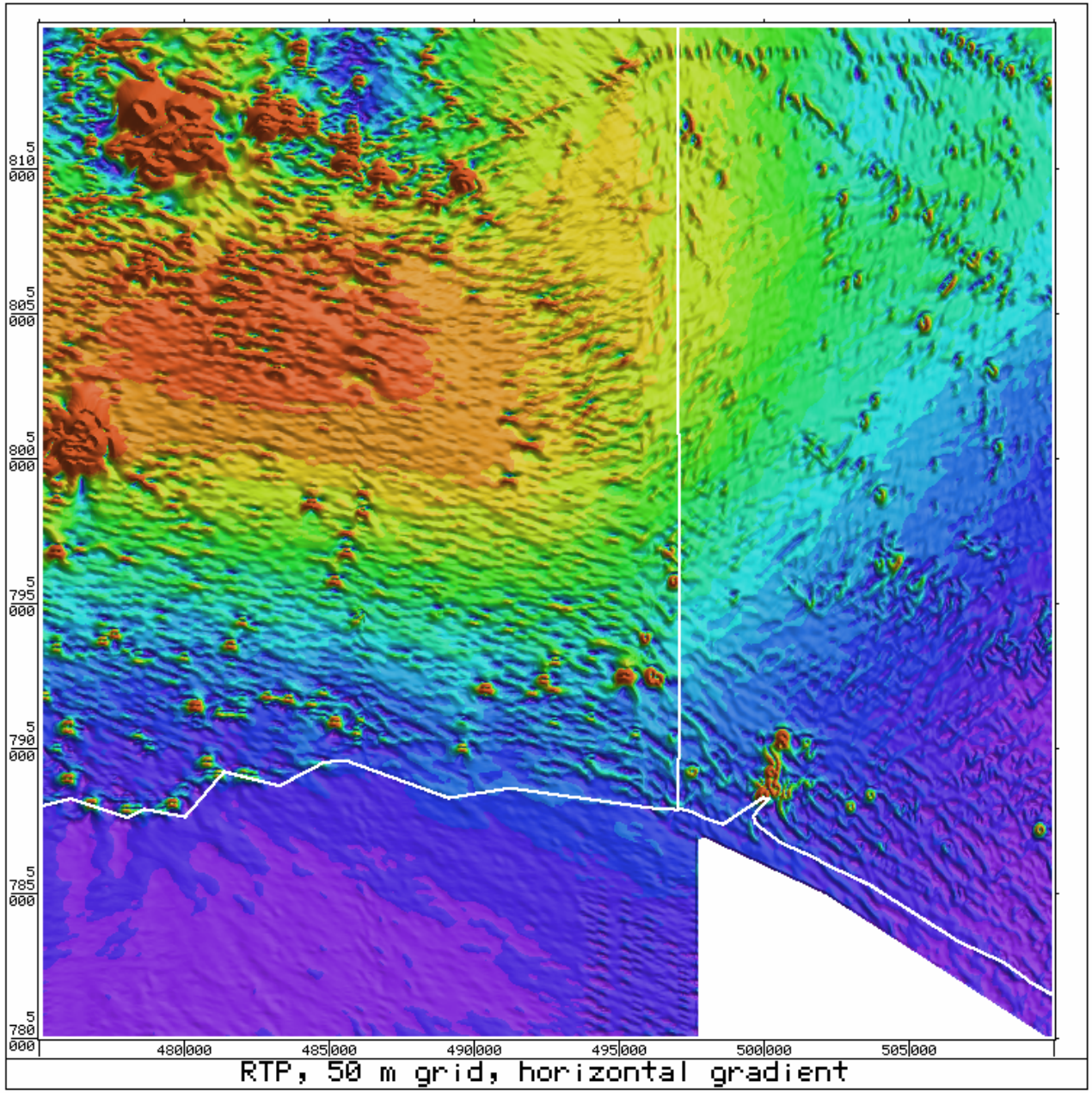

Figure 47. RTP horizontal gradient

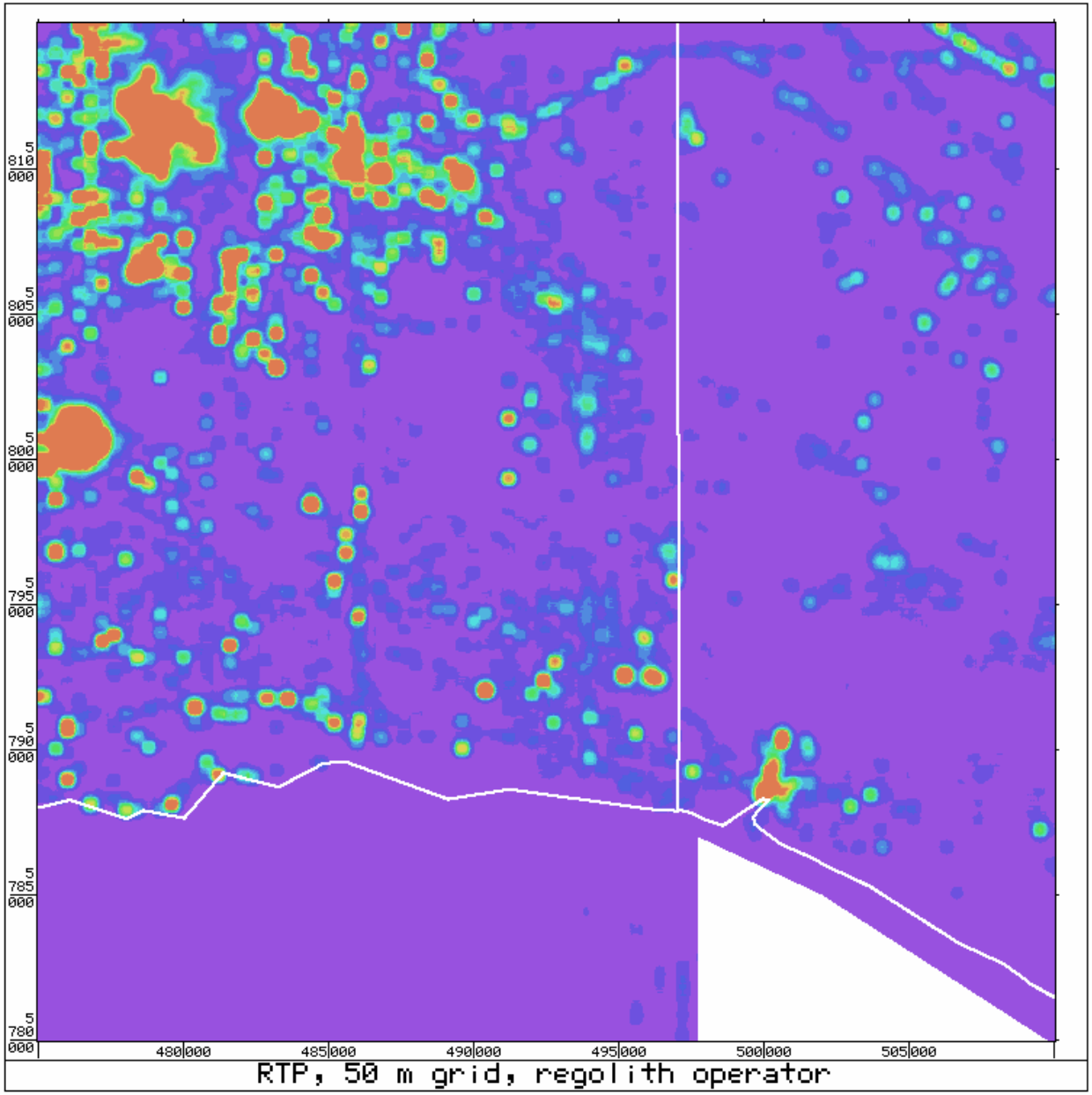

Figure 48. RTP, "regolith" enhancement

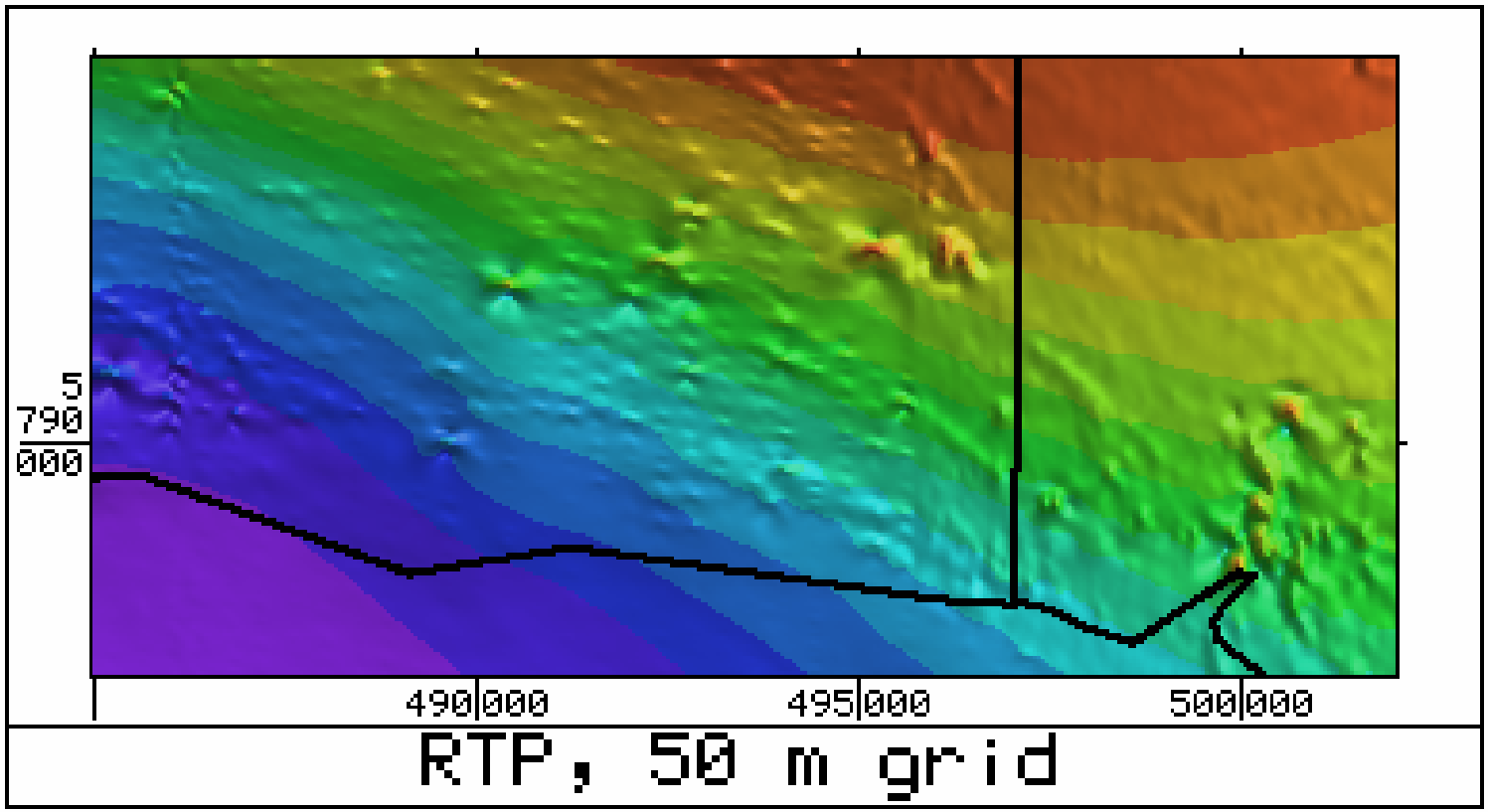

Figure 49. RTP, prospect area

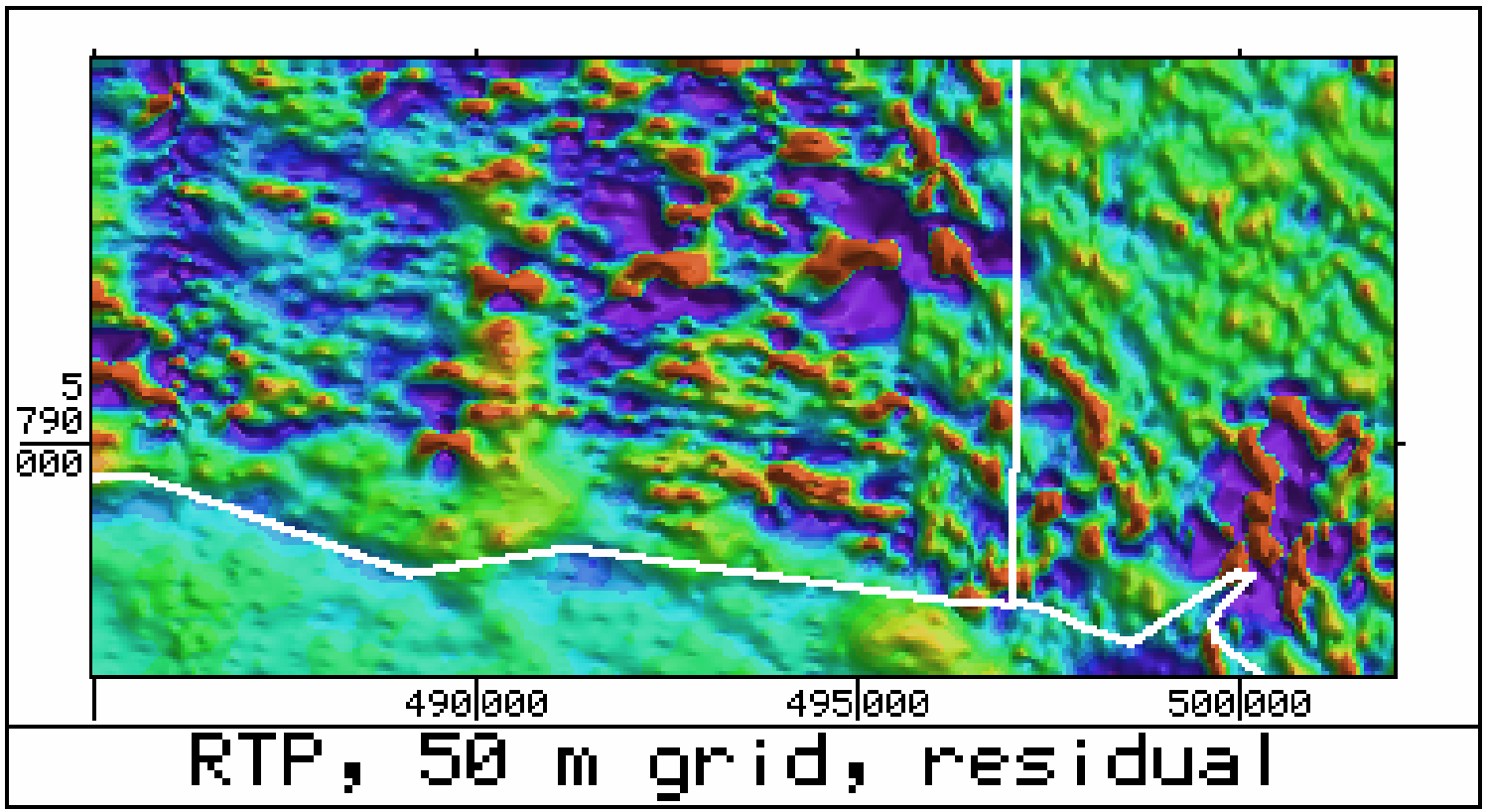

Figure 50. RTP, residual, 2.5 km operator

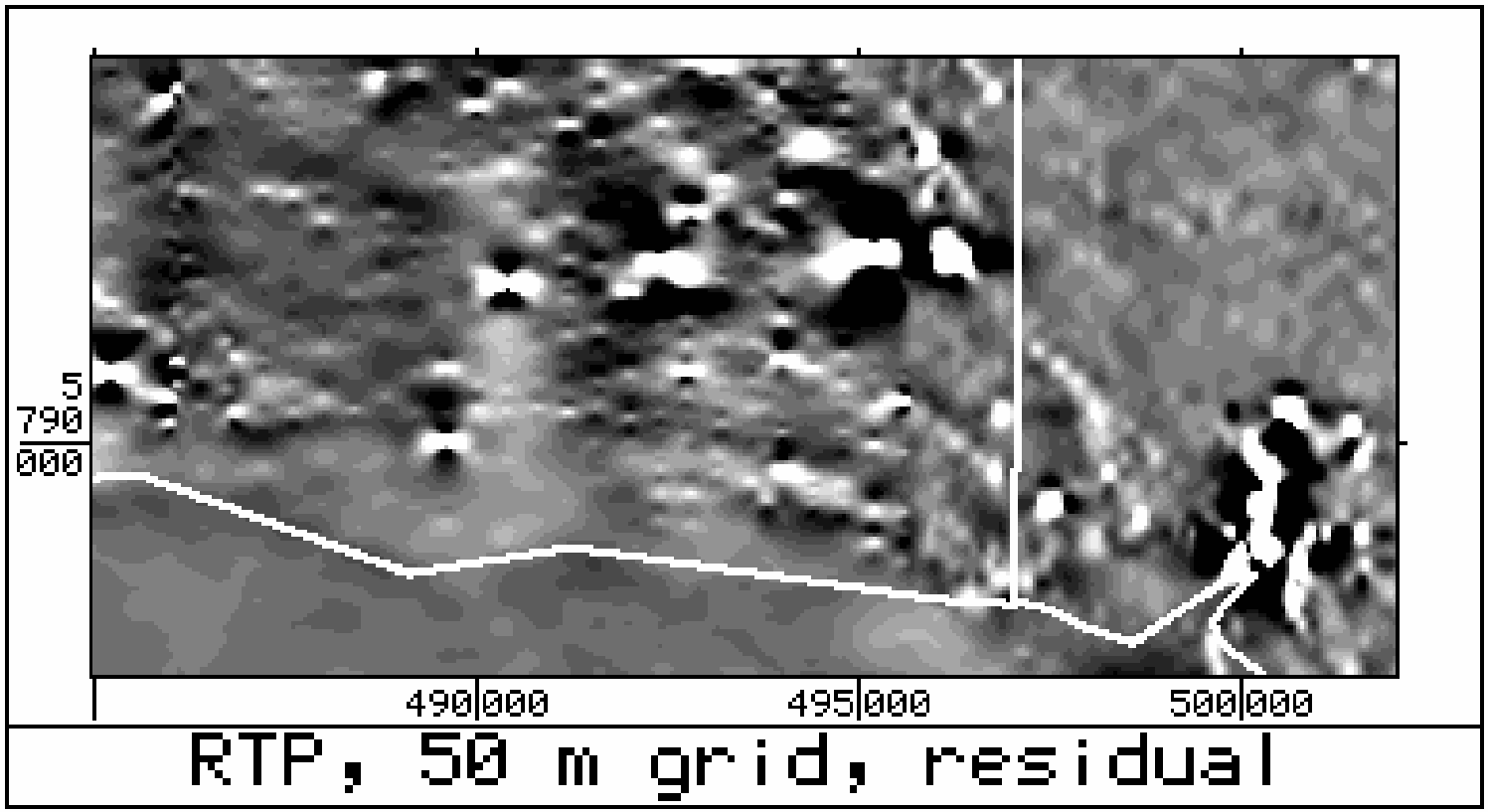

Figure 51. RTP, residual, 2.5 km operator

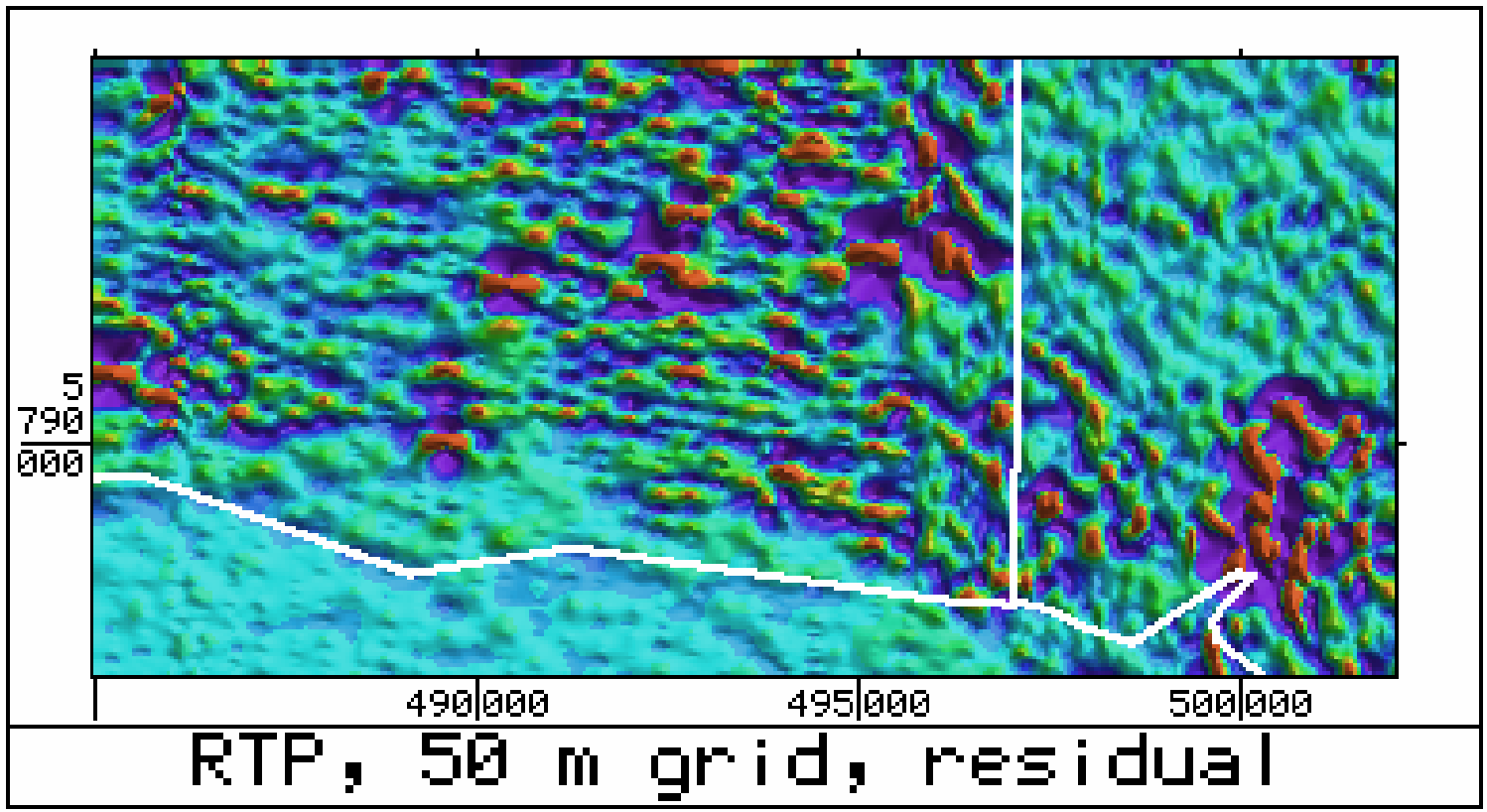

Figure 52. RTP, residual, 1 km operator

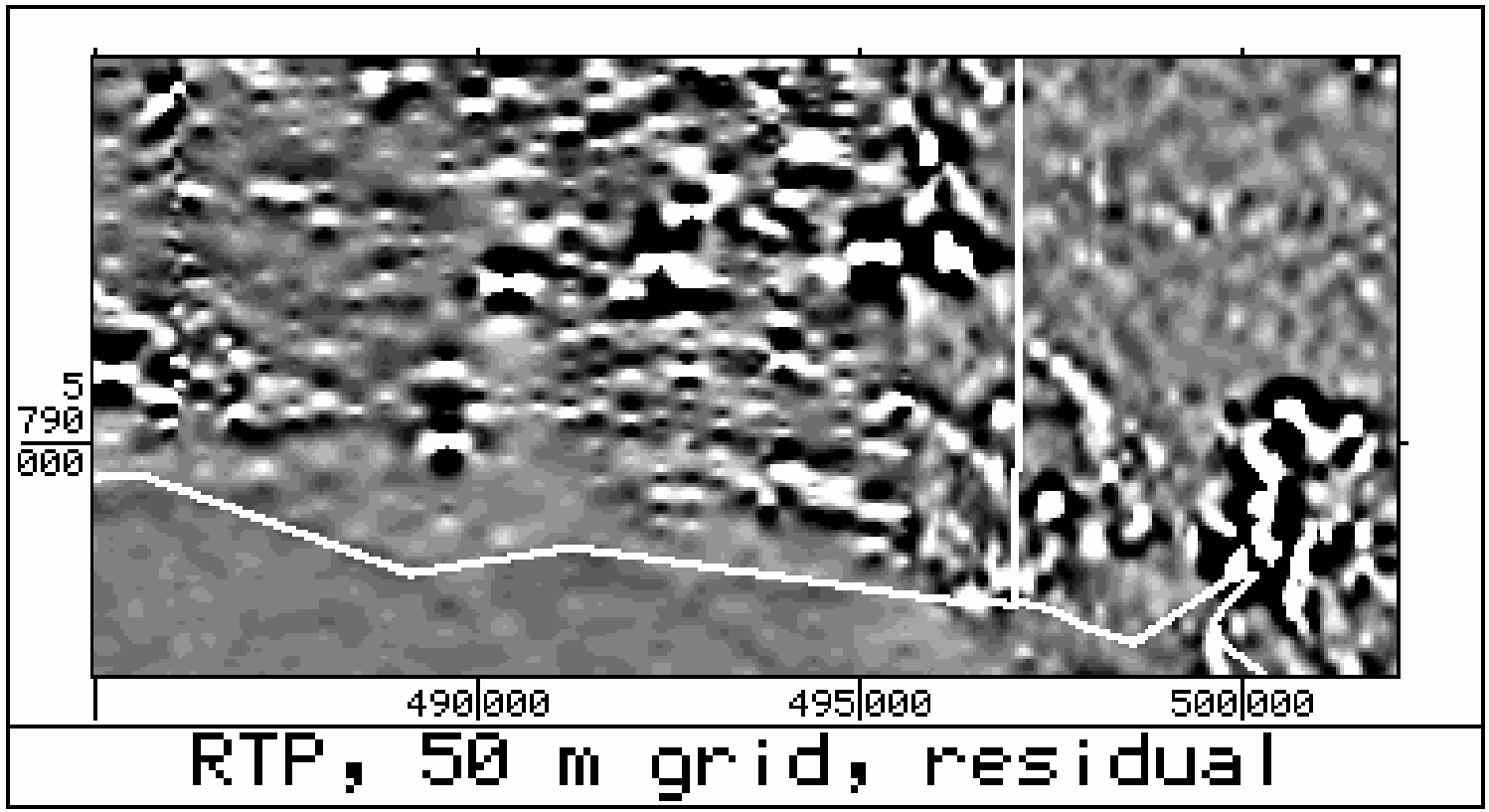

Figure 53. RTP, residual, 1 km operator

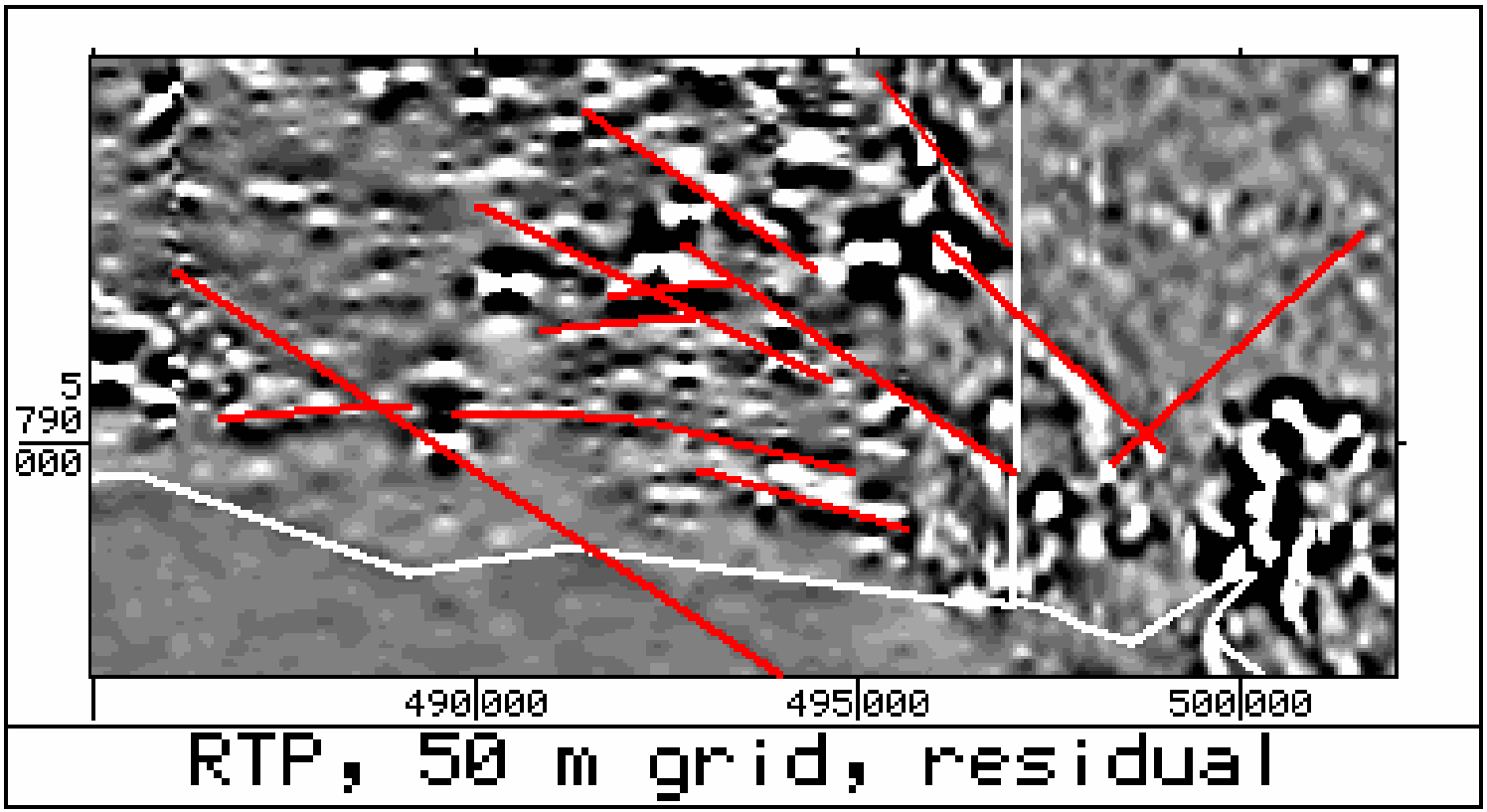

Figure 54. RTP, residual, 1 km operator, with interpreted lineations

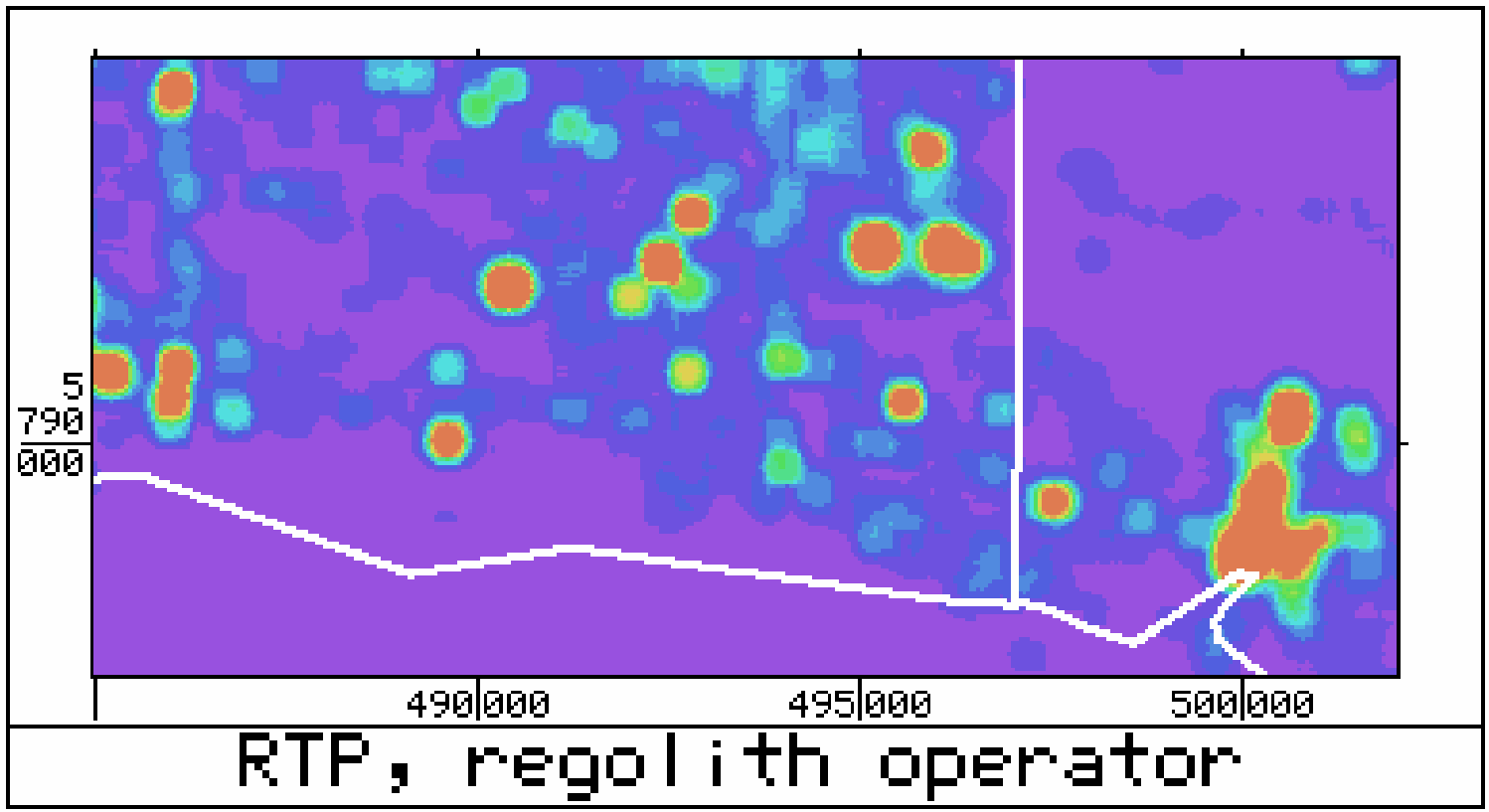

Figure 55. RTP, "regolith" operator

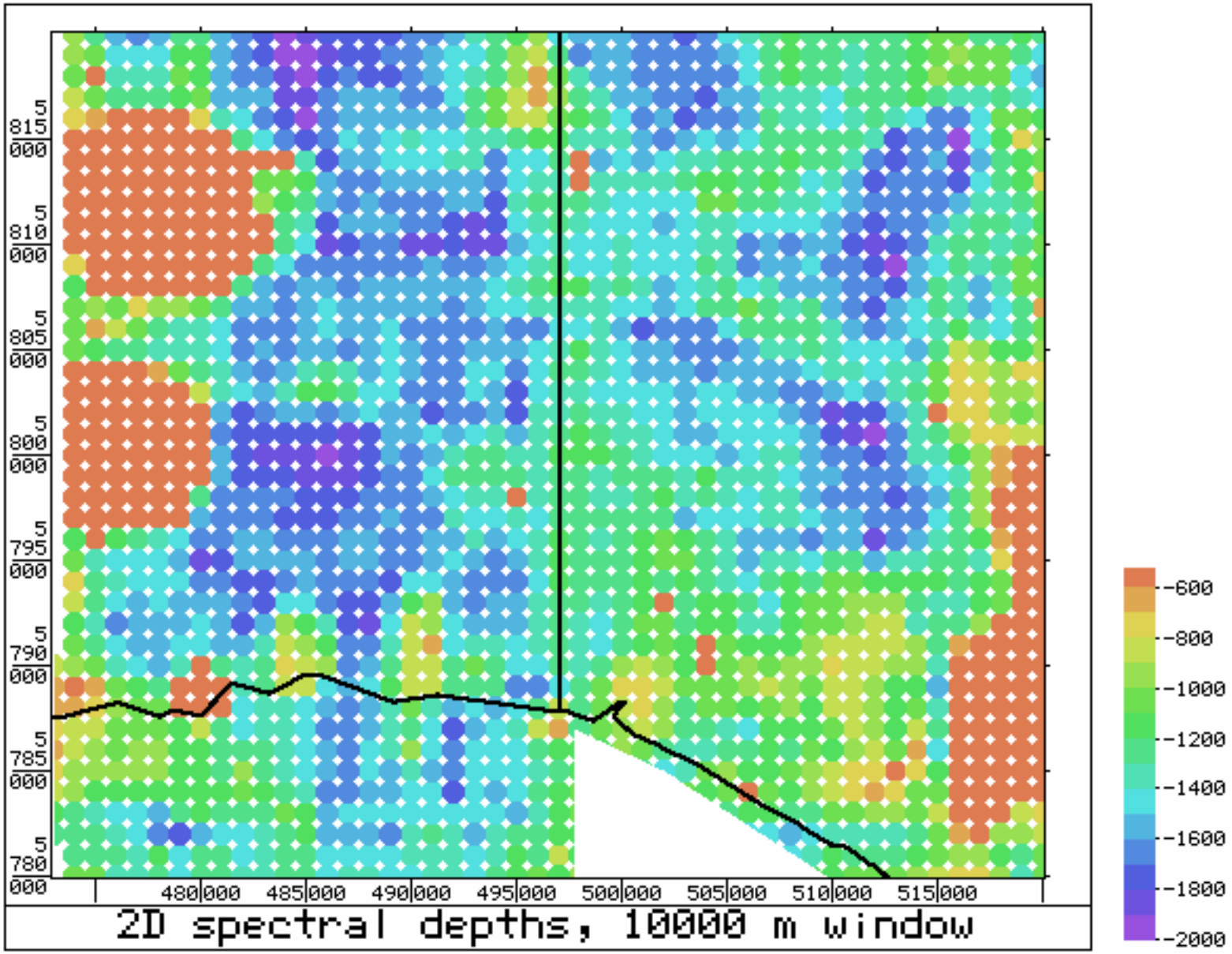

Figure 56. Magnetic spectral depths, 10 km window

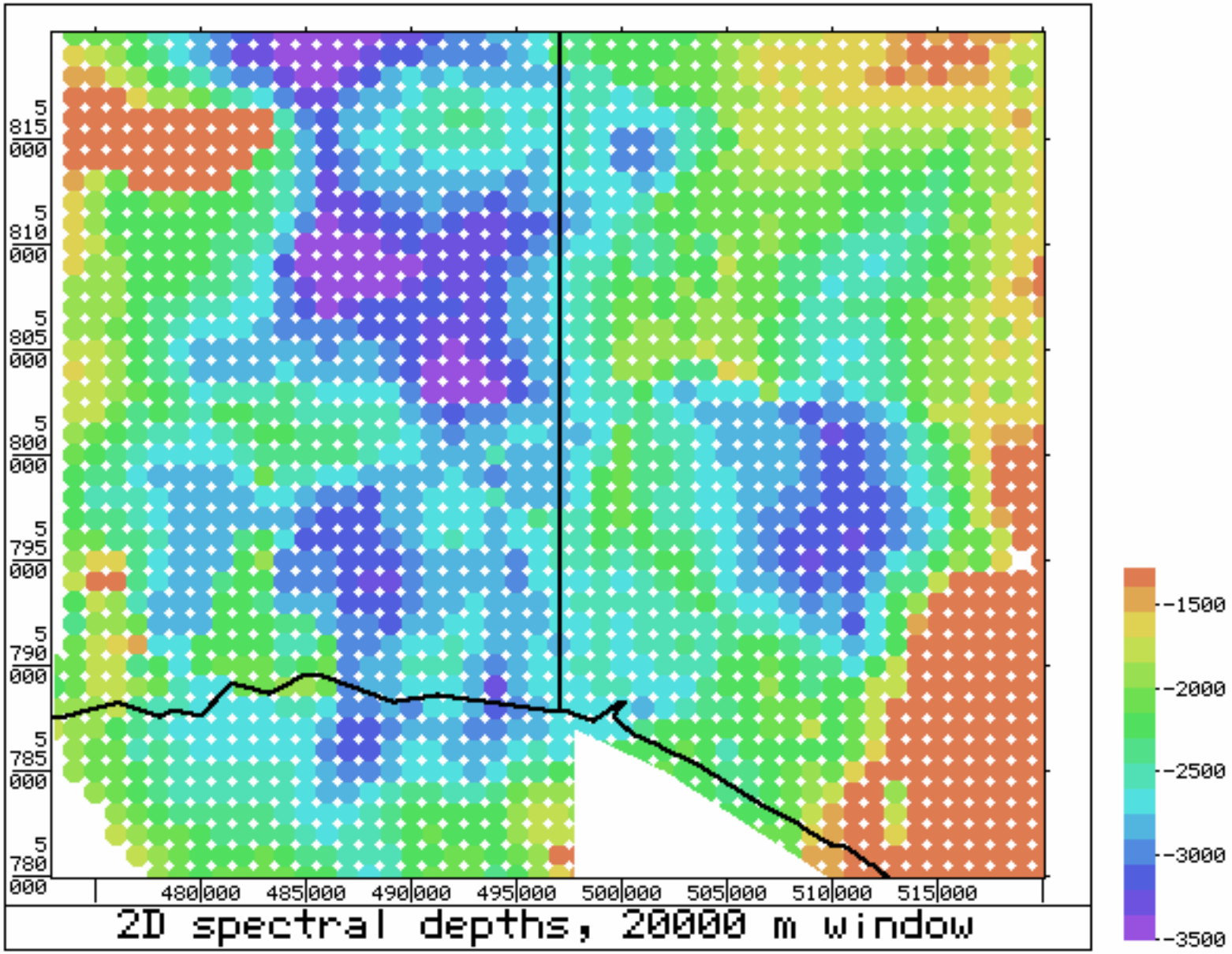

Figure 57. Magnetic spectral depths, 20 km window

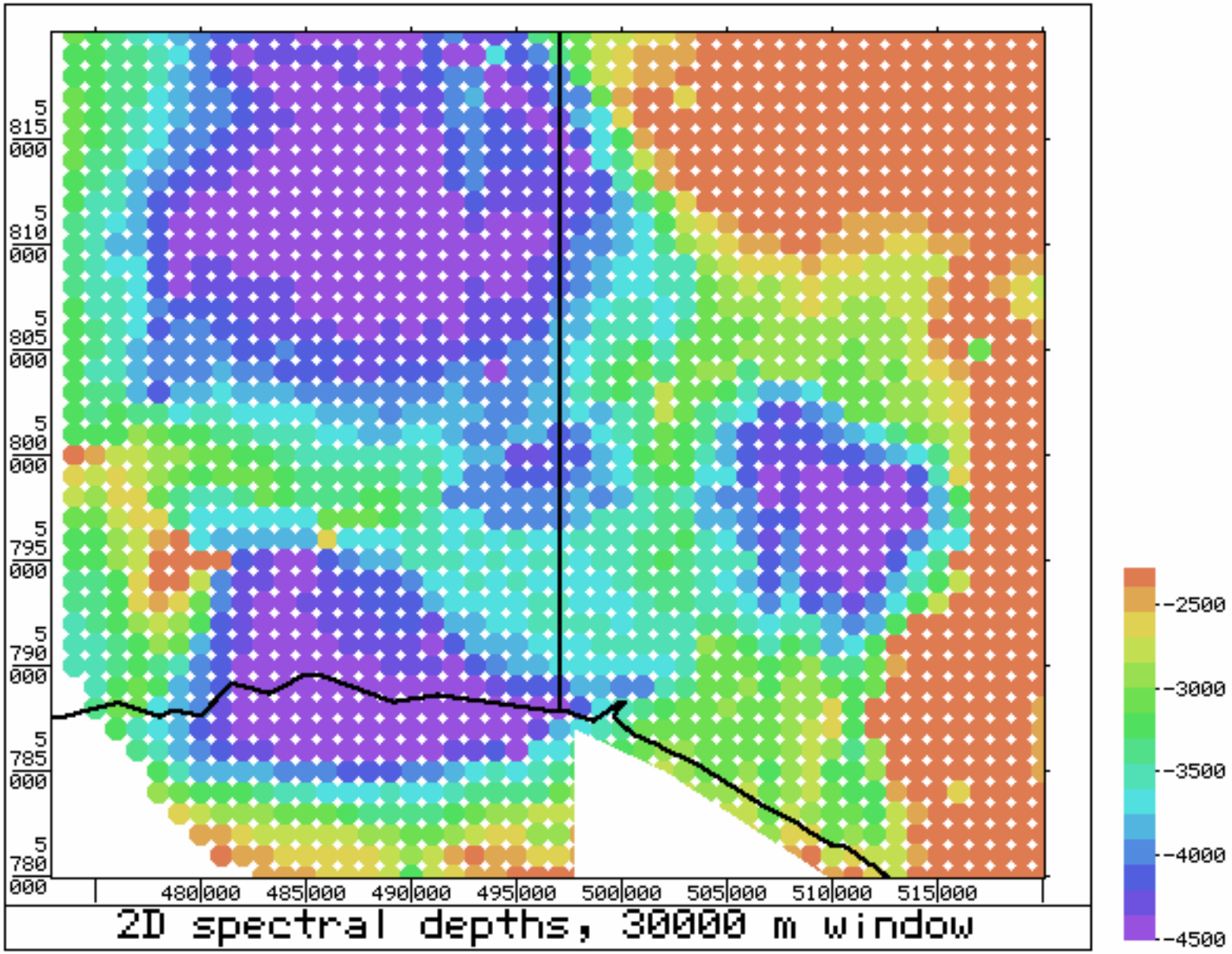

Figure 58. Magnetic spectral depths, 30 km window

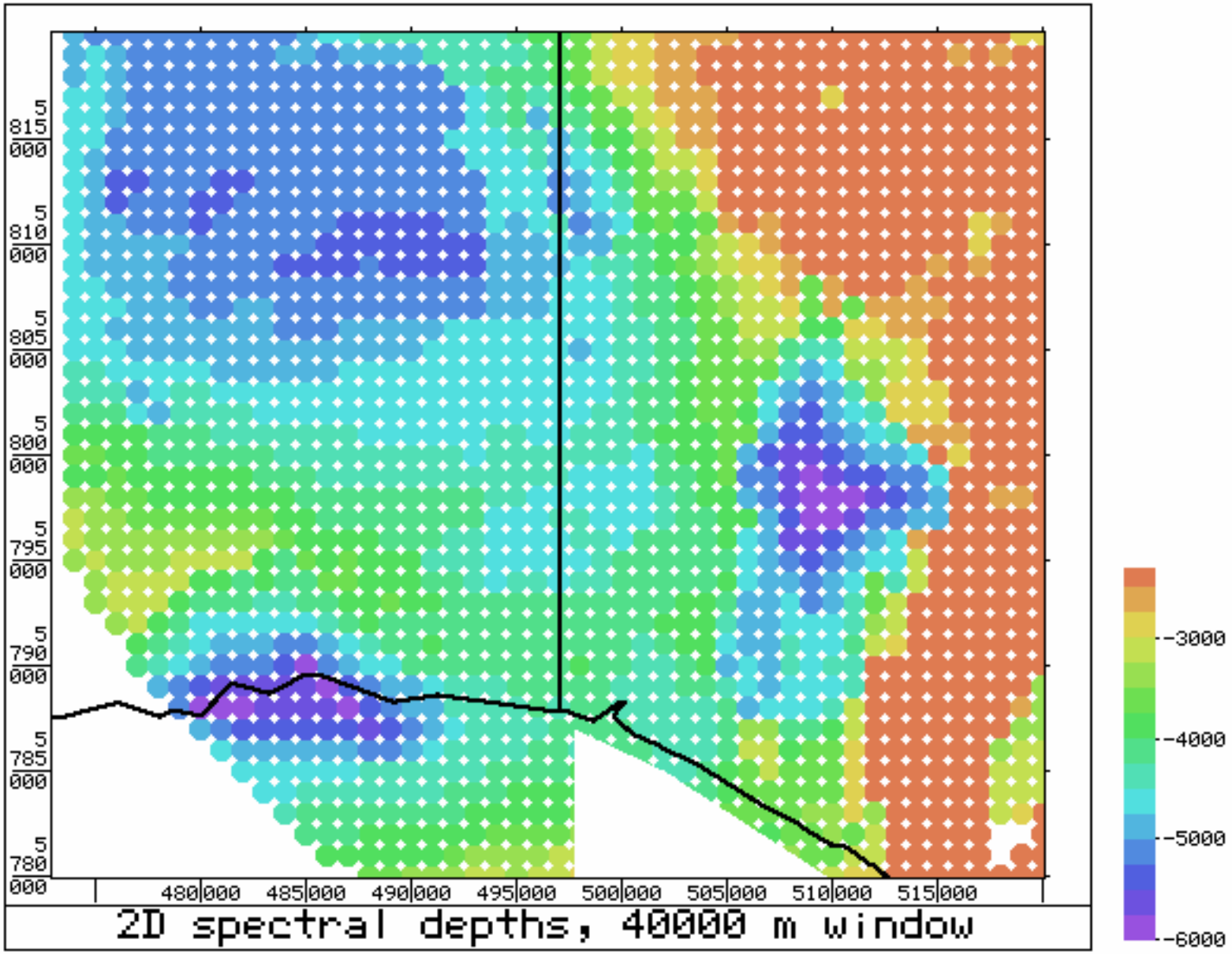

Figure 59. Magnetic spectral depths, 40 km window

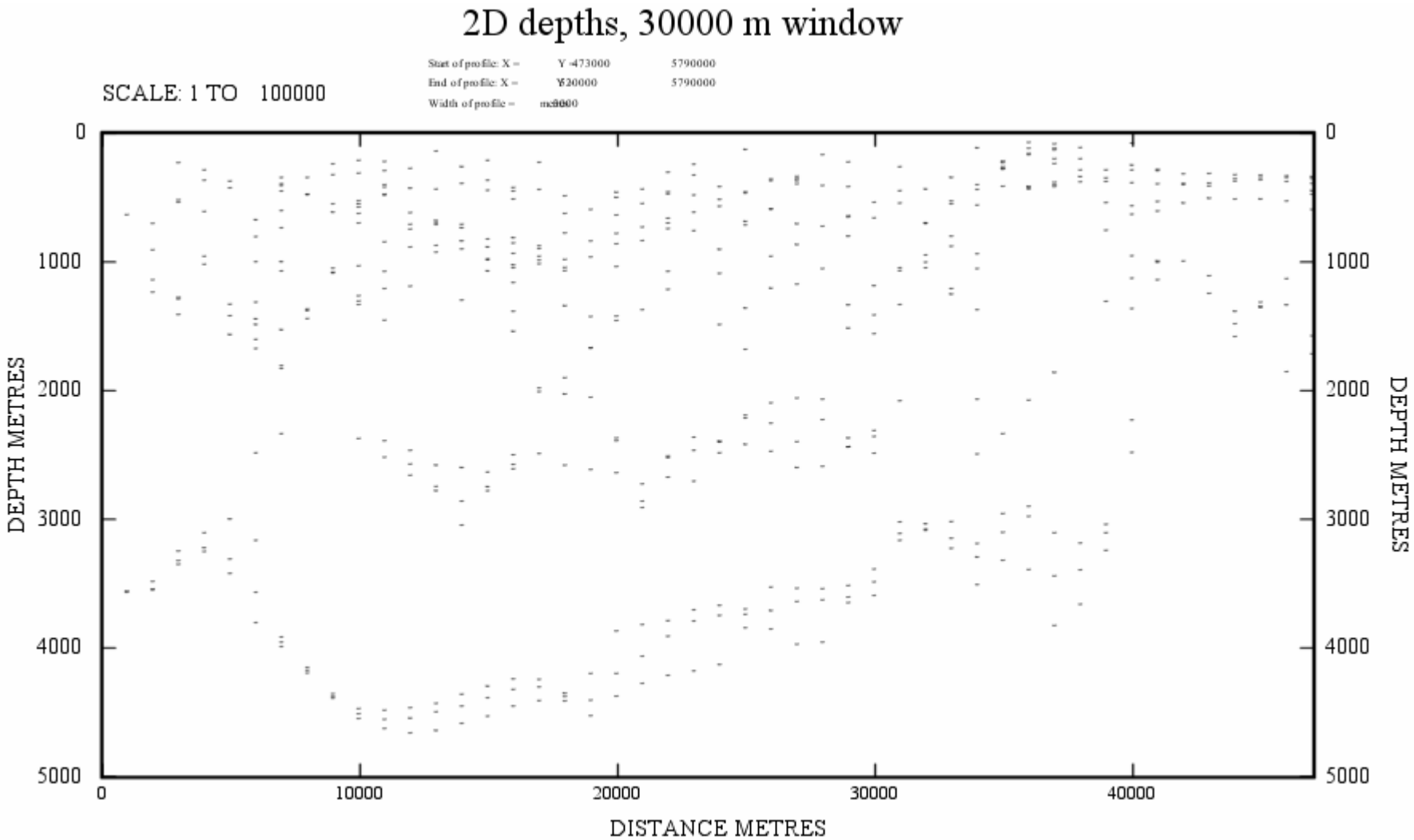

Figure 60 – 2D Spectral Depths, 30000m Window, W-E Section at 5790000mN

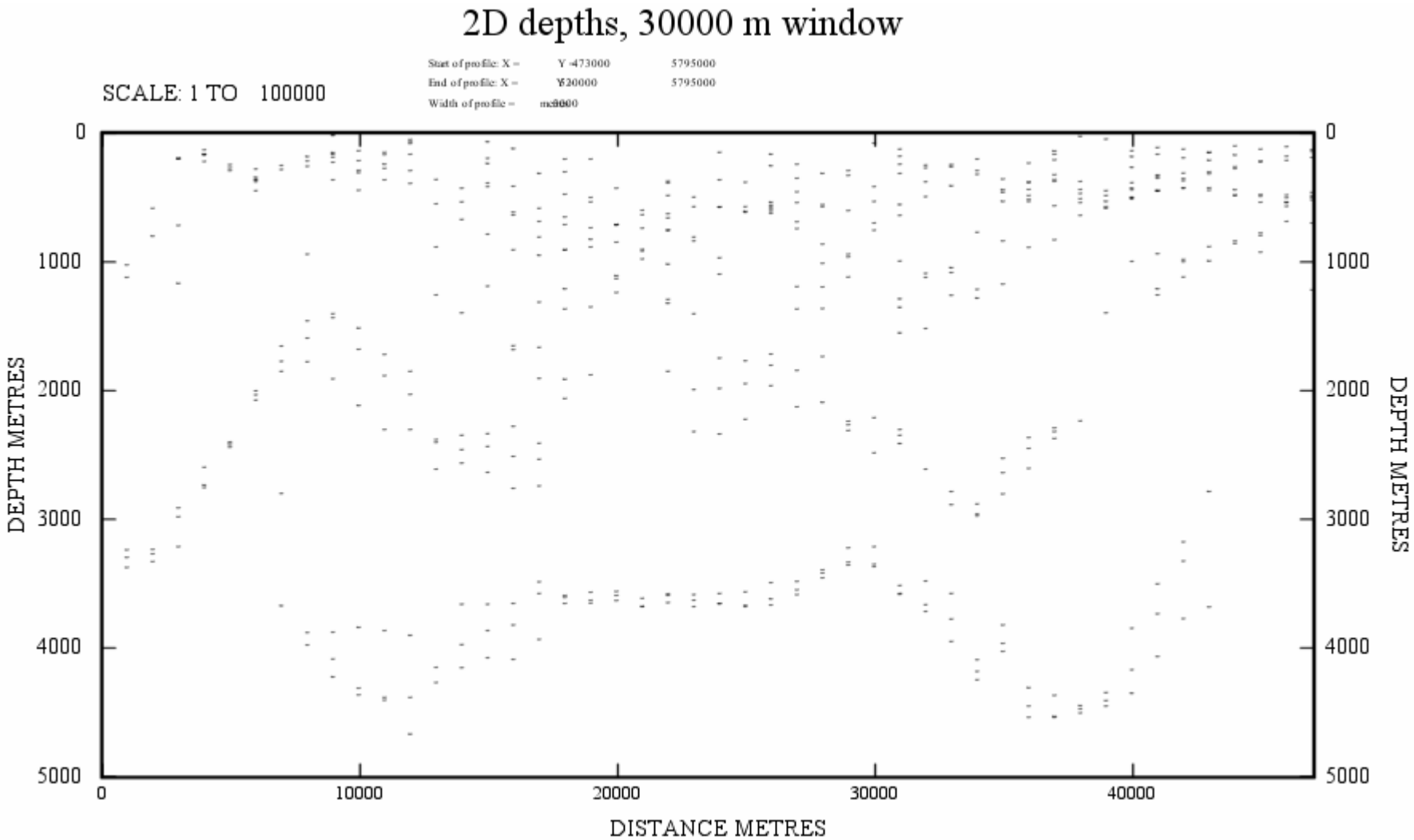

Figure 61 – 2D Spectral Depths, 30000m Window, W-E Section at 5795000mN

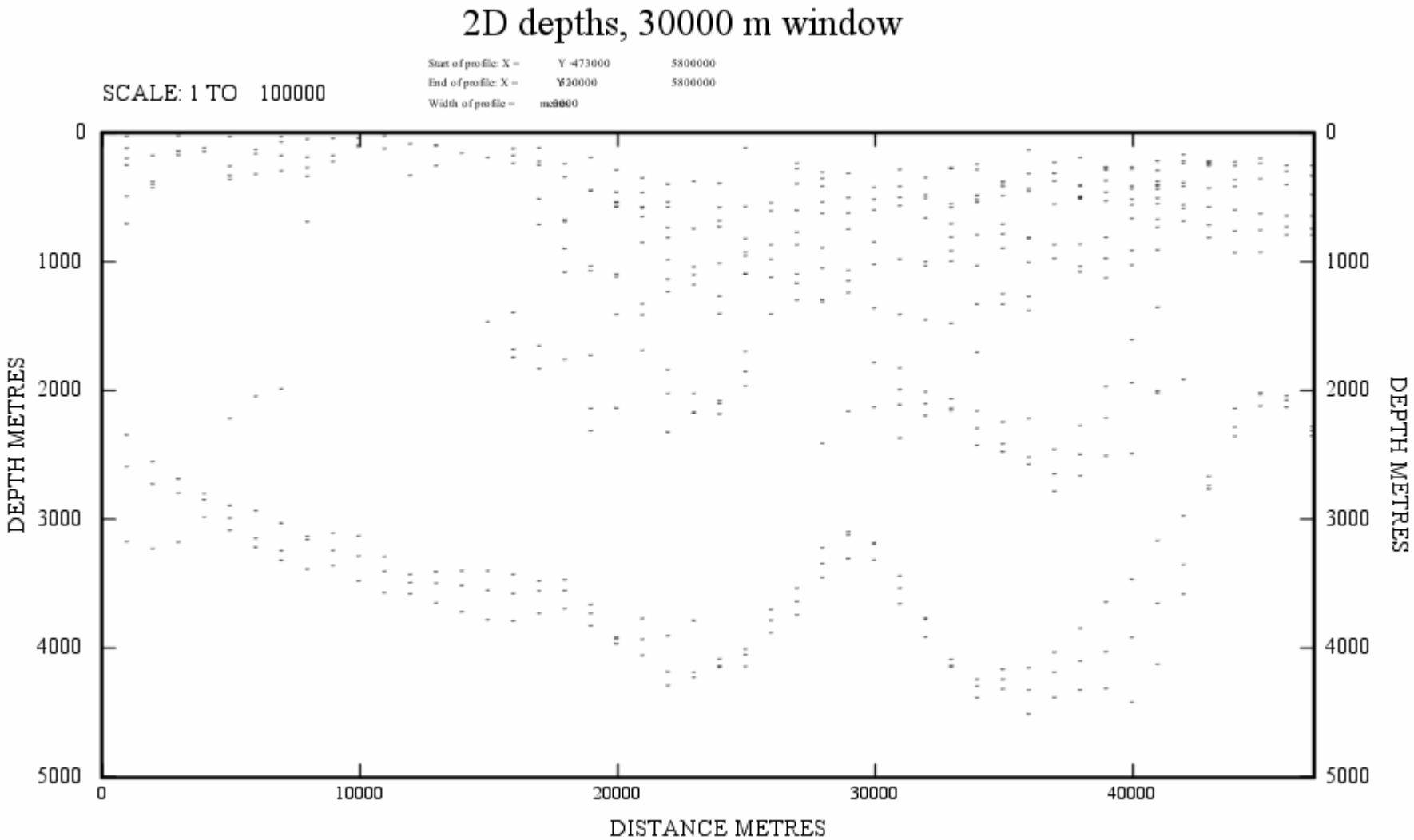

Figure 62 – 2D Spectral Depths, 30000m Window, W-E Section at 5800000mN

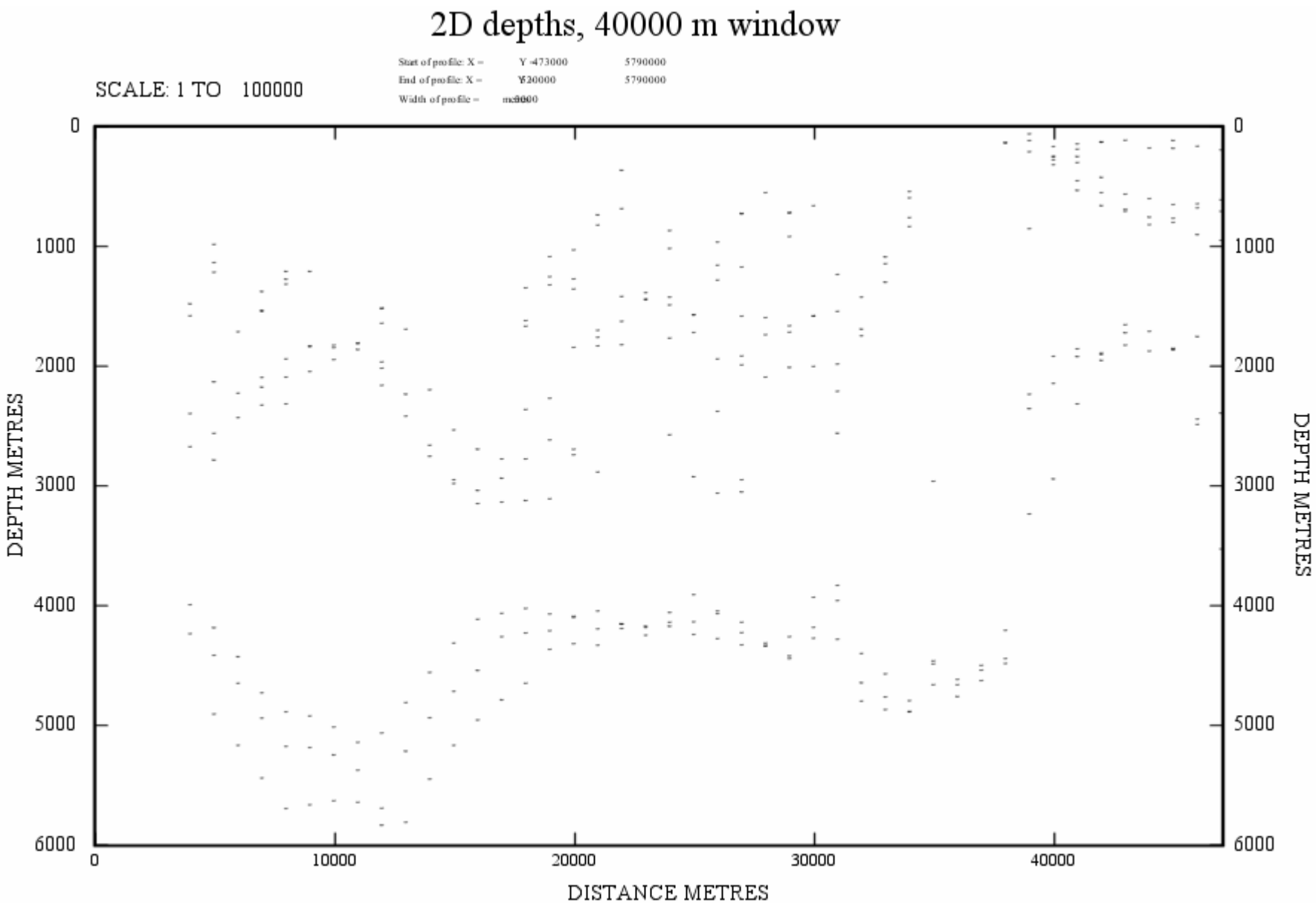

Figure 63 – 2D Spectral Depths, 30000m Window, W-E Section at 5790000mN

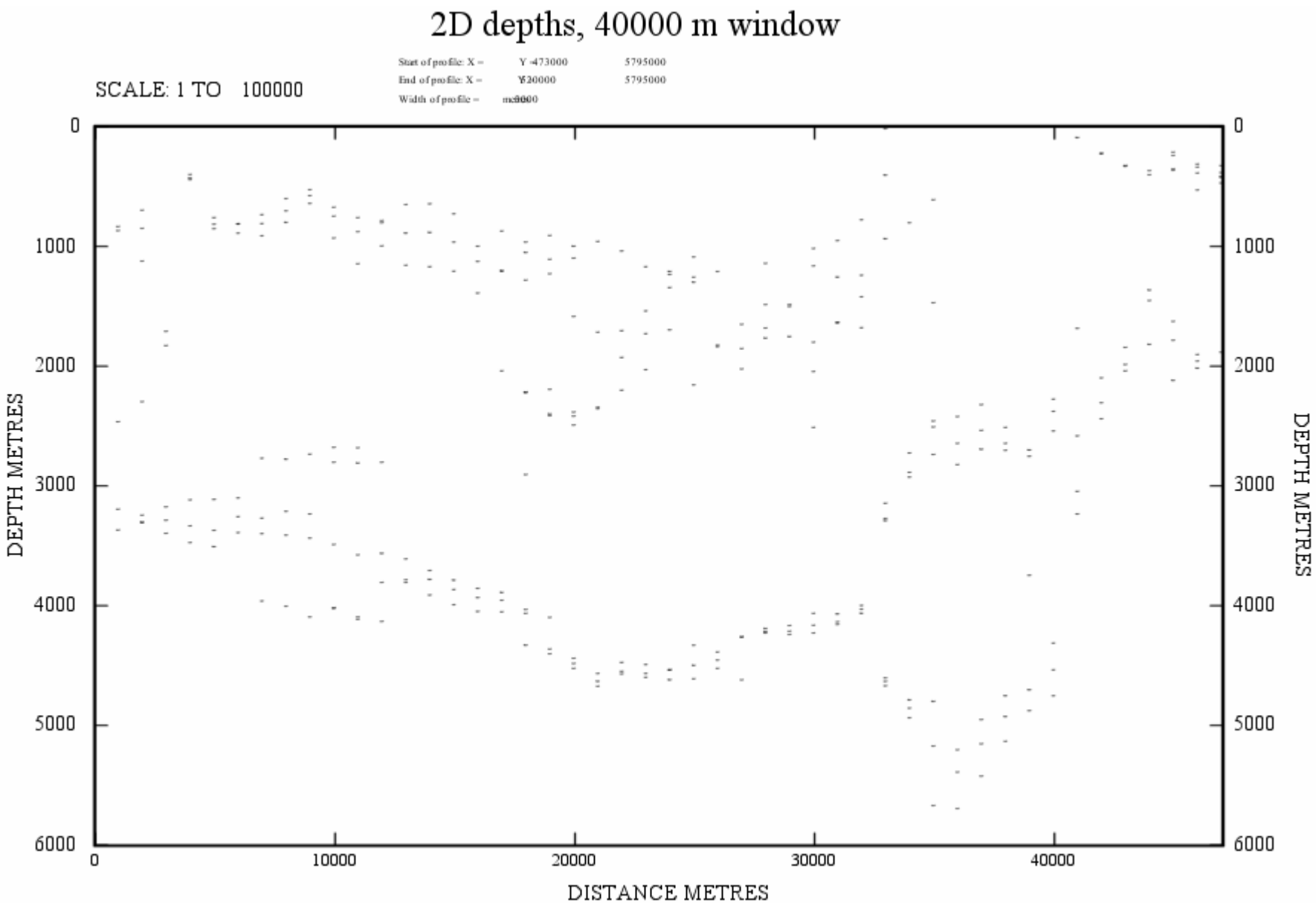

Figure 64 – 2D Spectral Depths, 30000m Window, W-E Section at 5795000mN

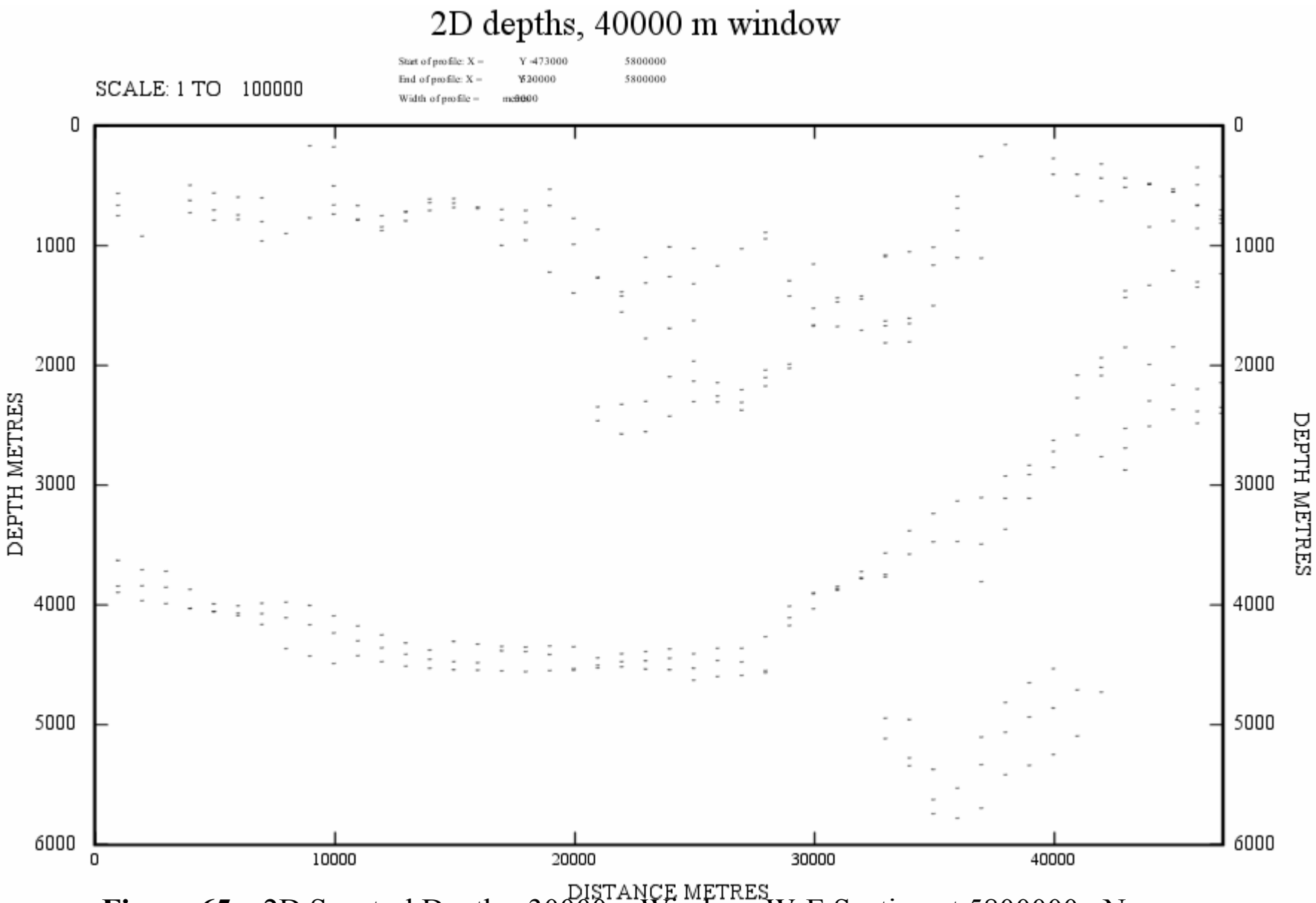

Figure 65 – 2D Spectral Depths, 30000m Window, W-E Section at 5800000mN

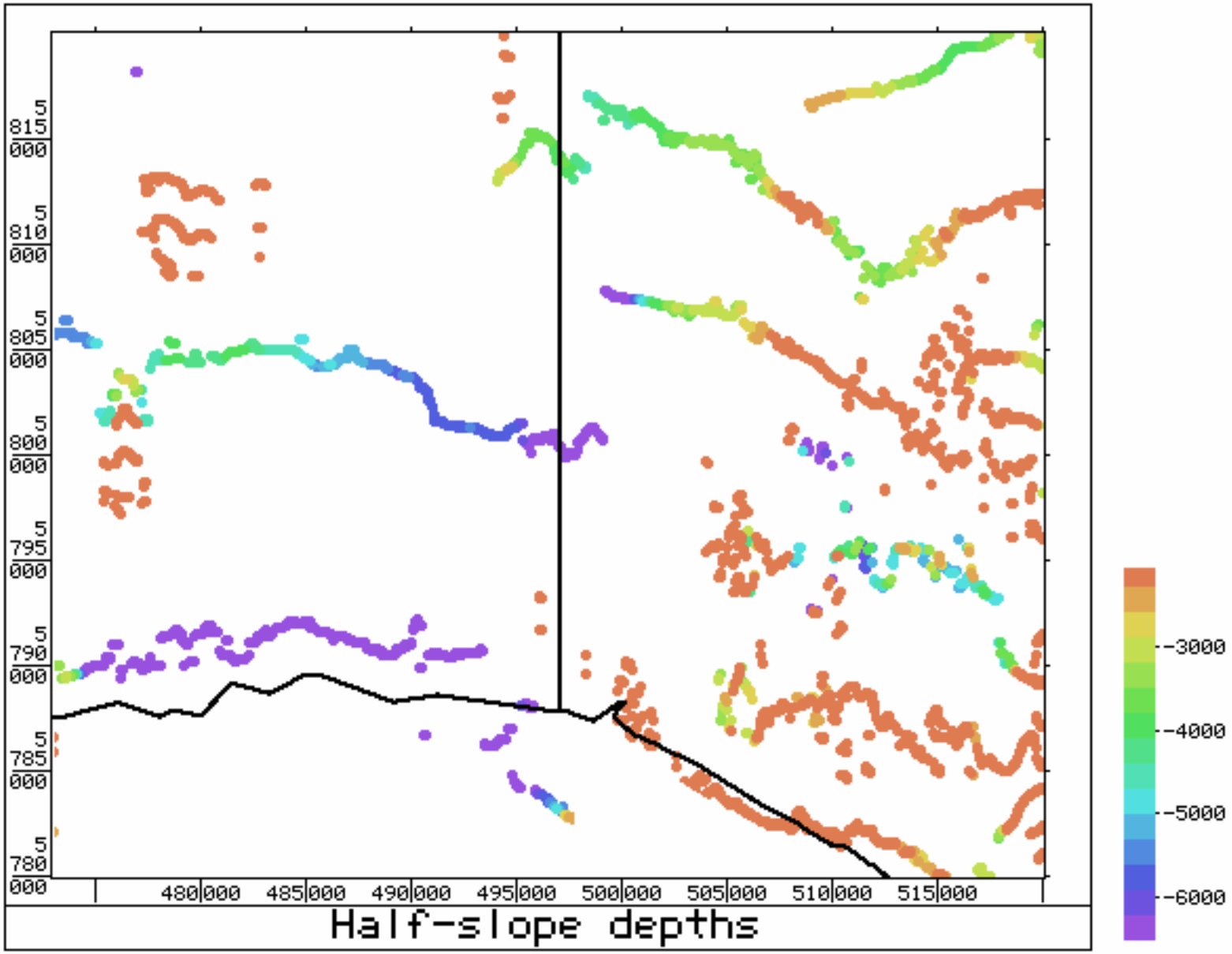

Figure 66. Magnetic half-slope depths

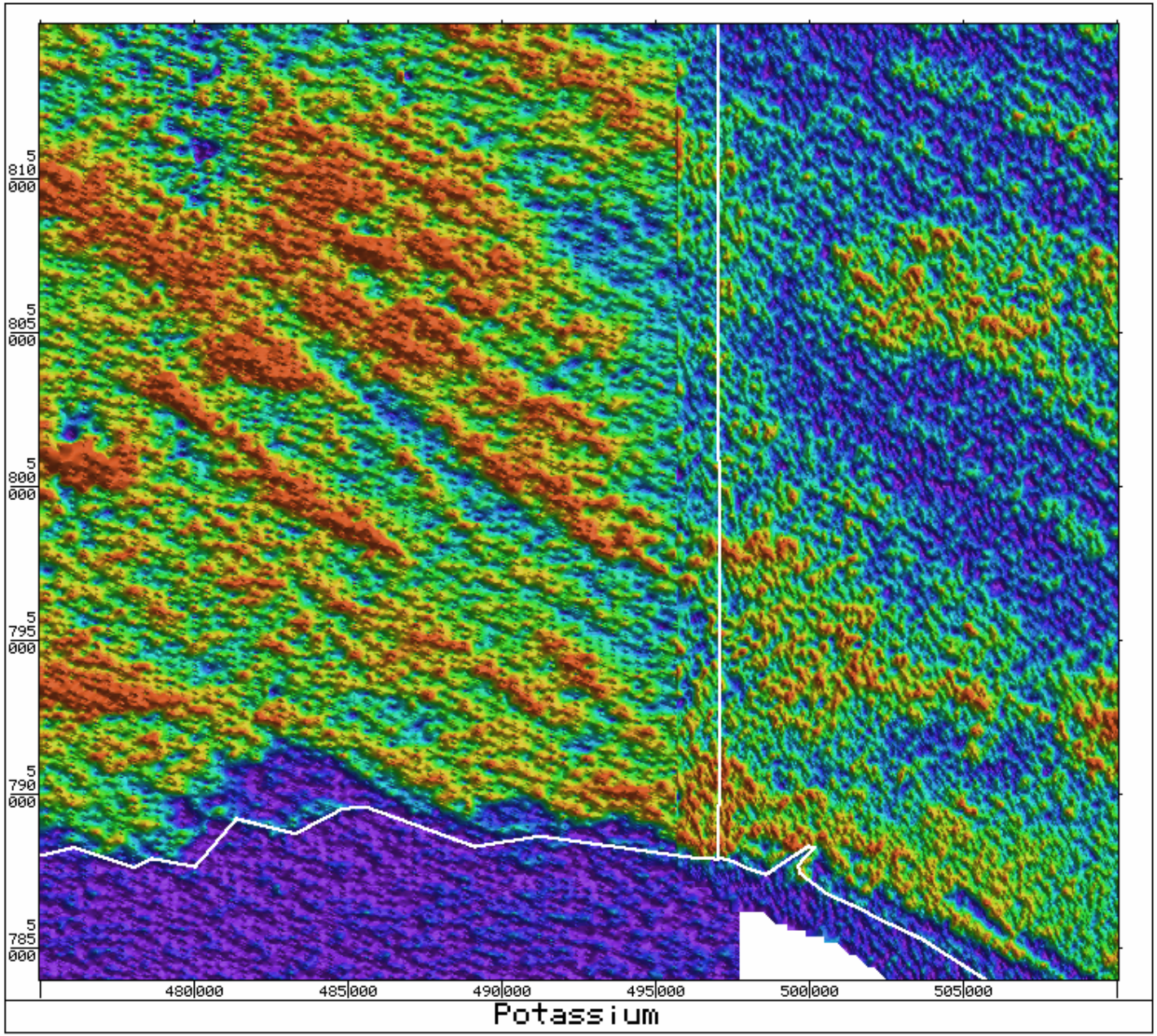

Figure 67. Potassium, merged 50 m grids

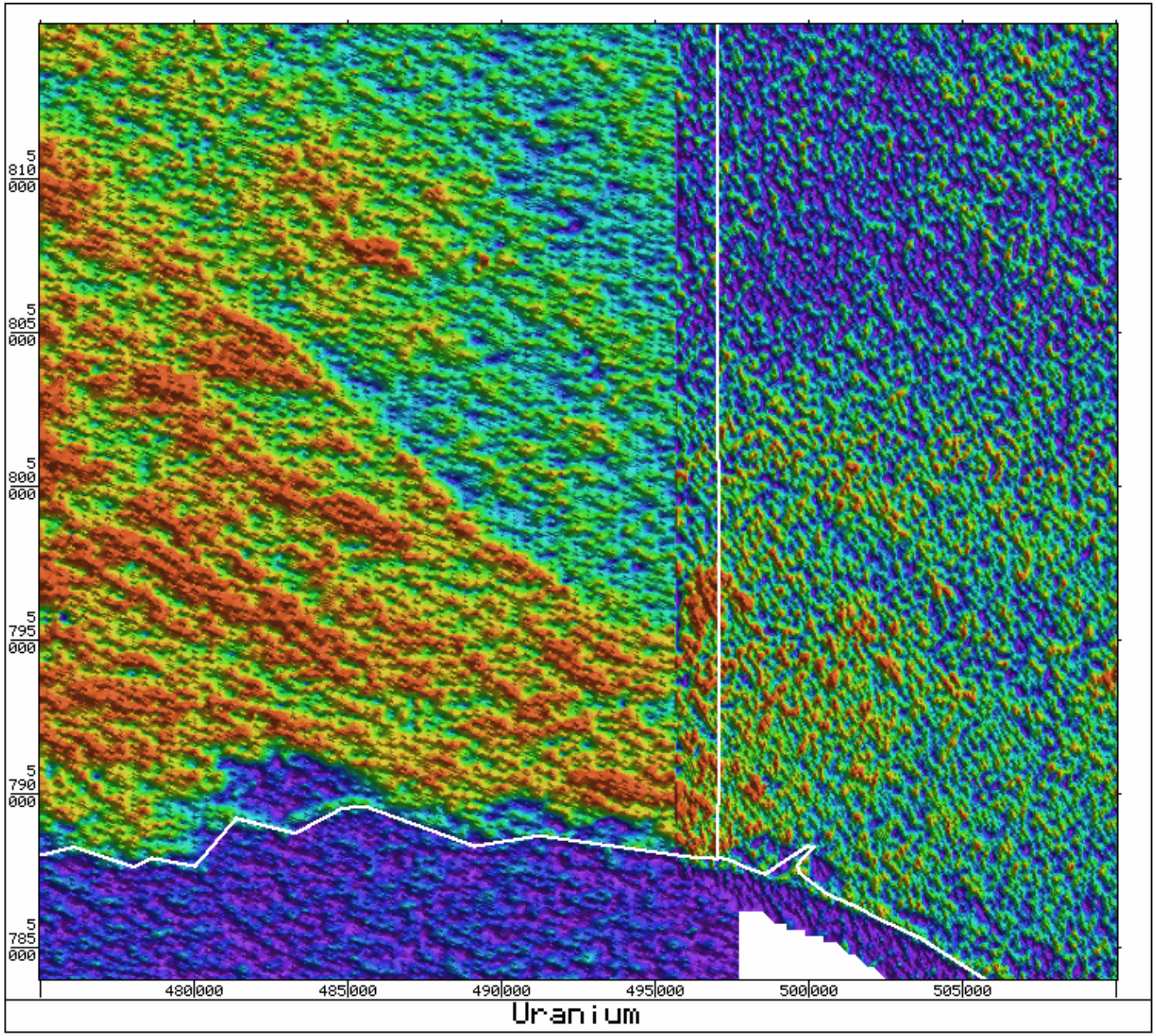

Figure 68. Uranium, merged 50 m grids

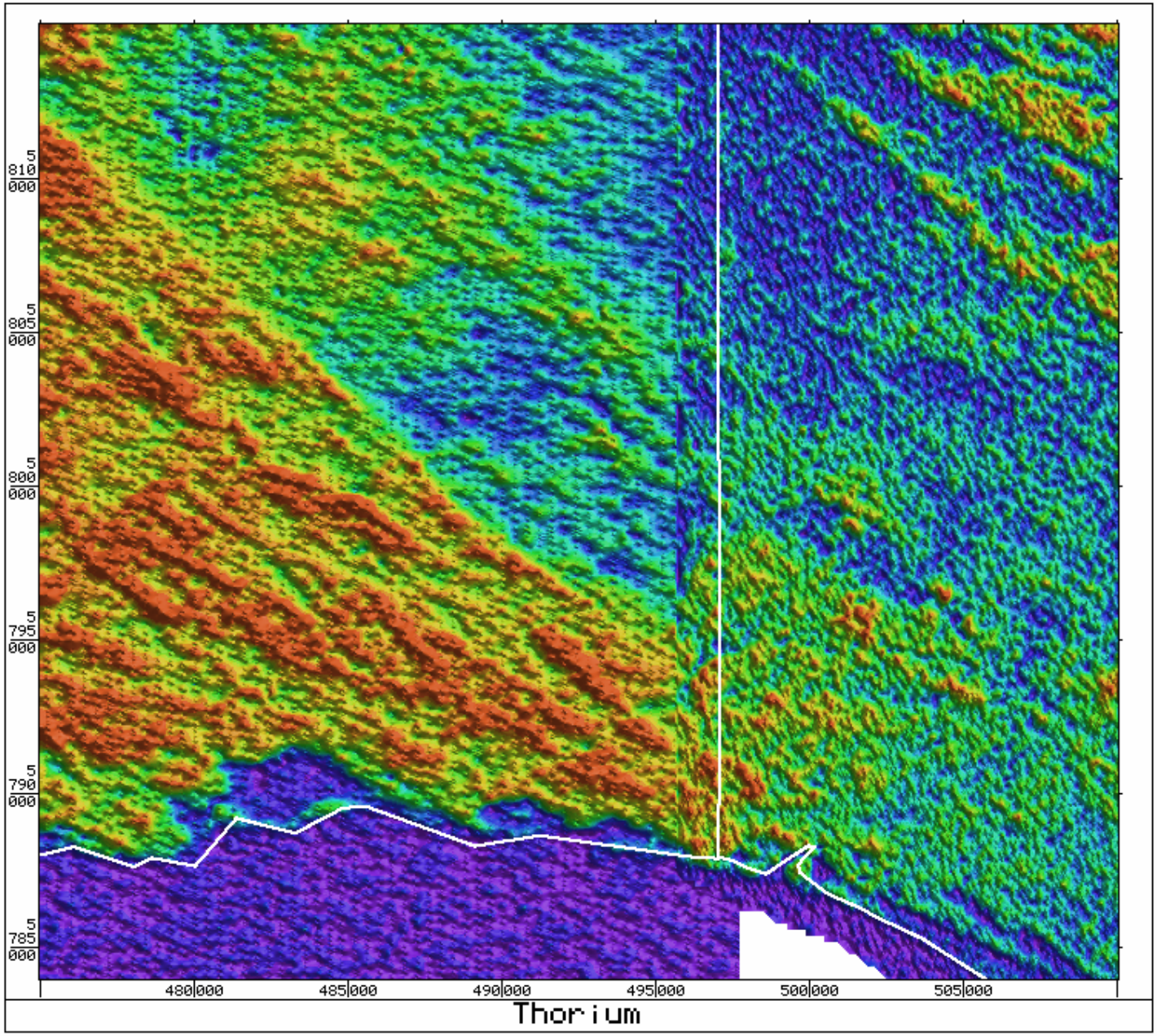

Figure 69. Thorium, merged 50 m grids

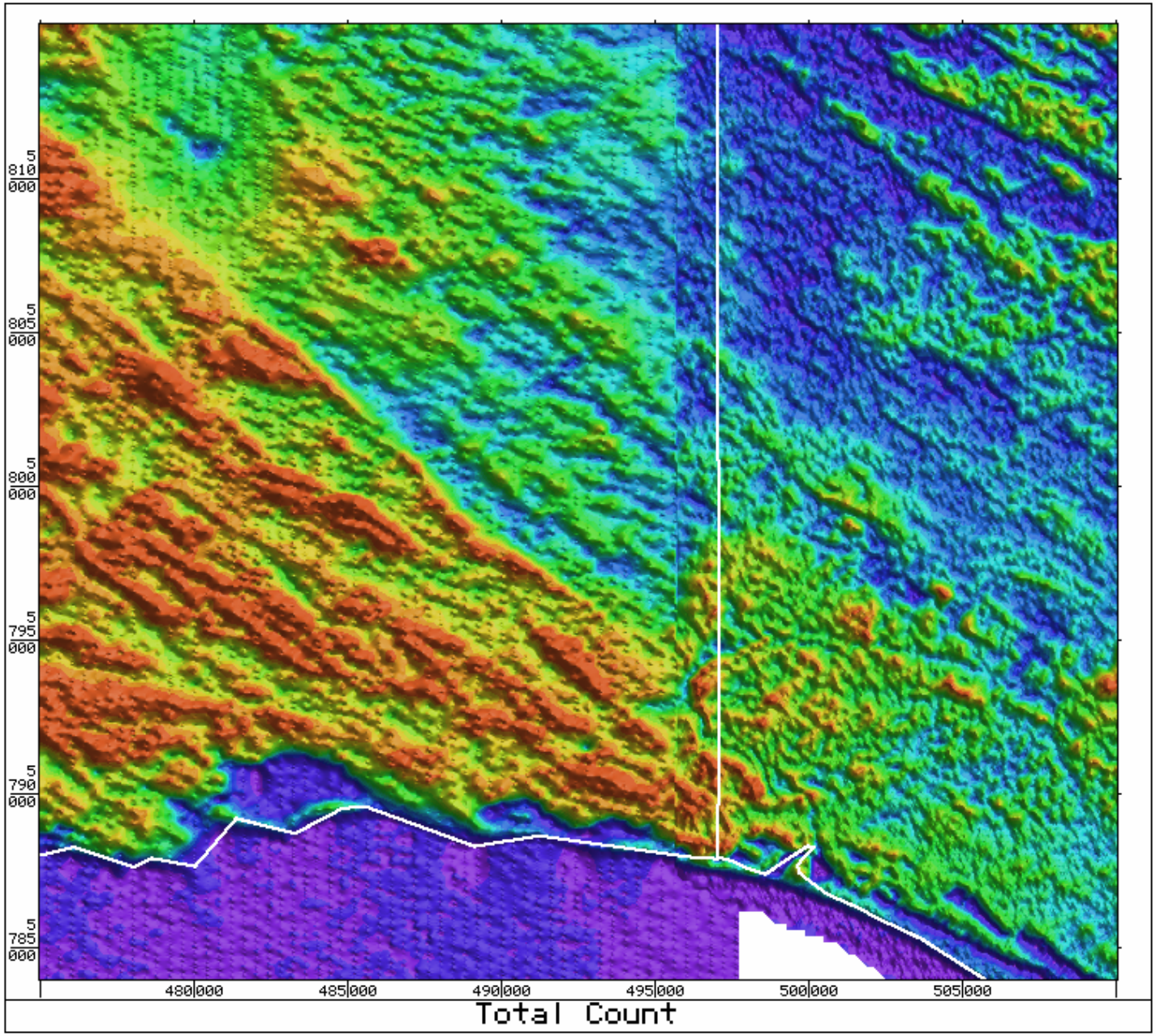

Figure 70. Total Count, merged 50 m grids

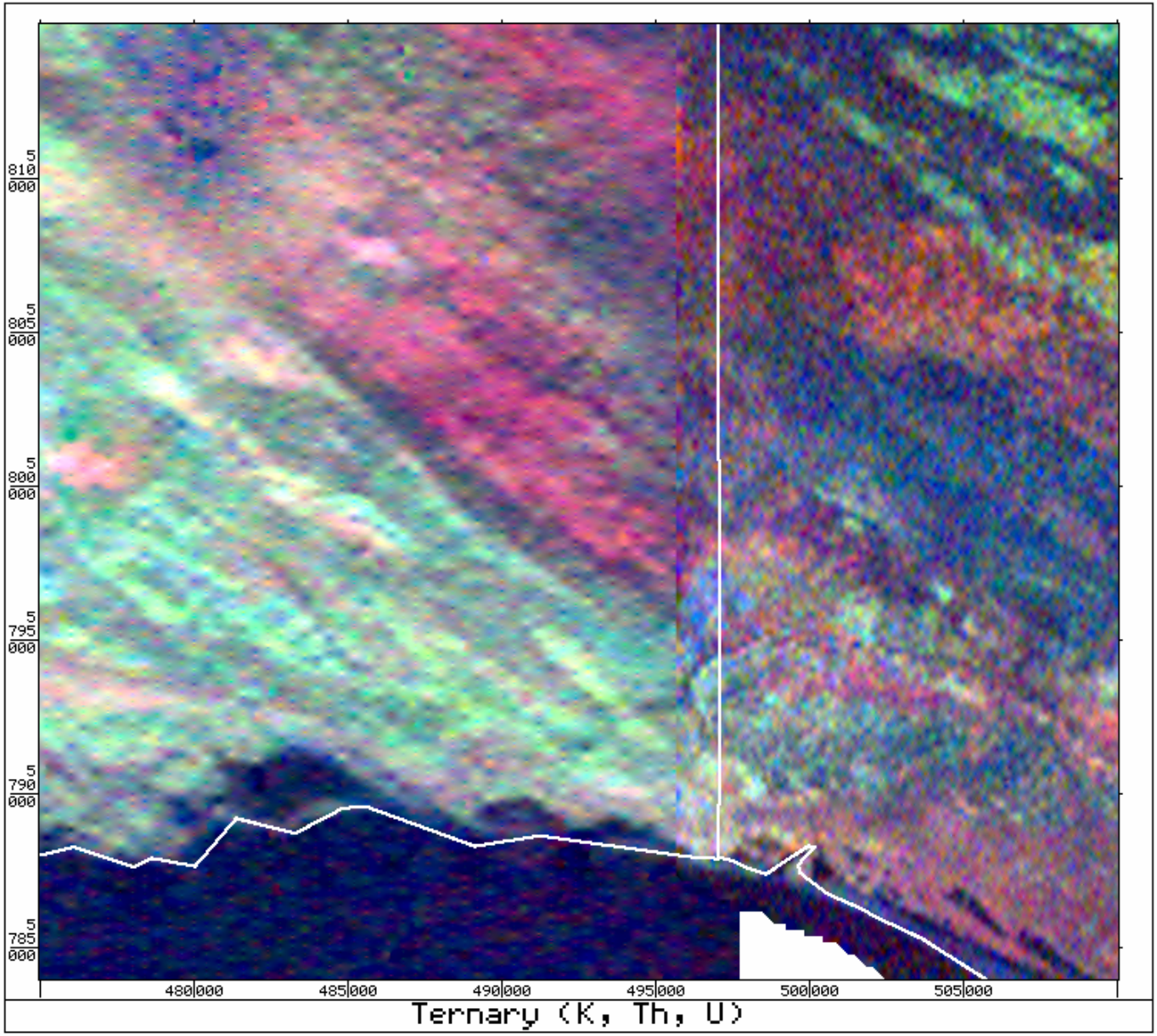

Figure 71. Radiometric ternary plot
(K red, Th green, U blue)

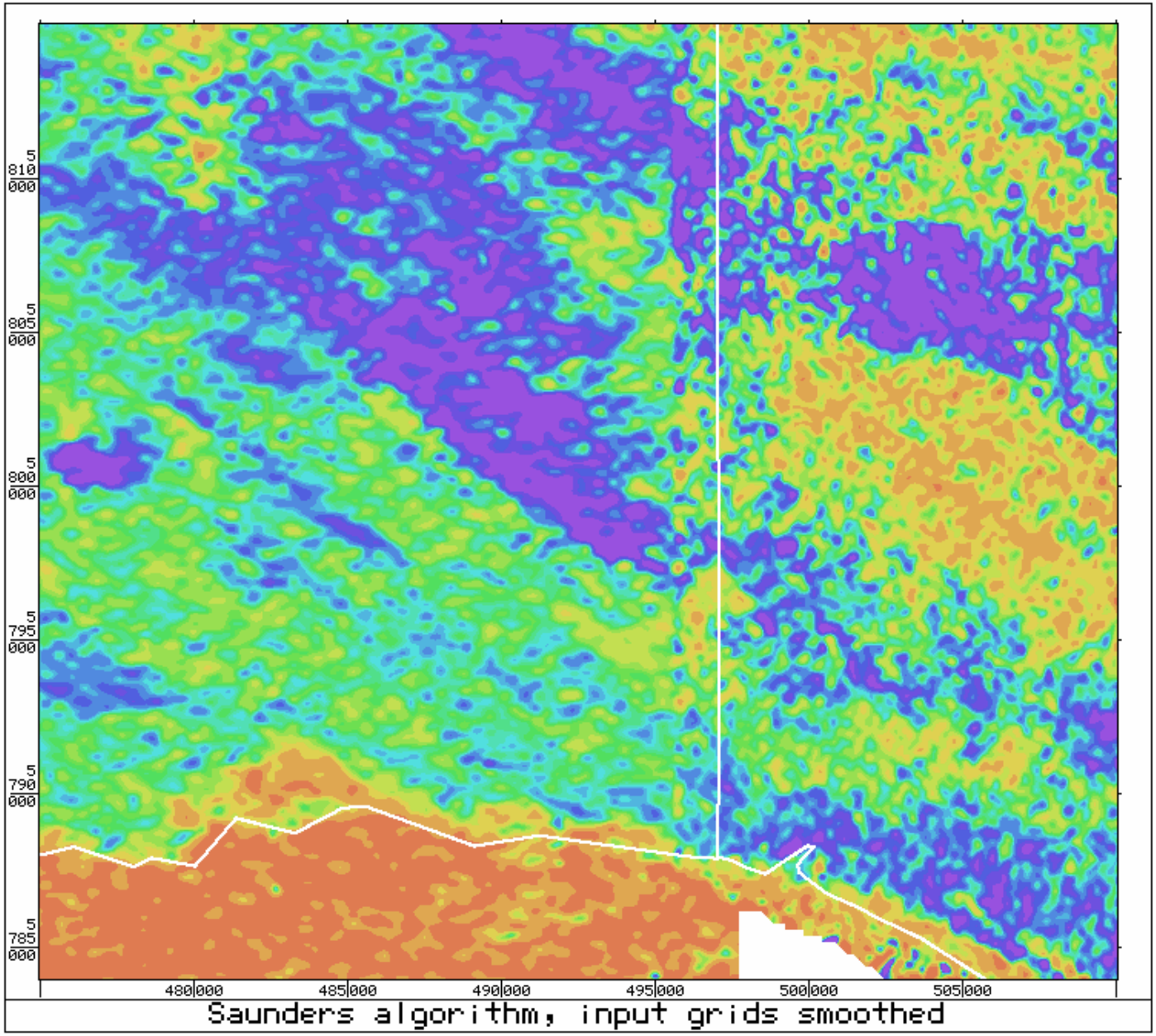

Figure 72. Petroleum factor, Saunders' (1994) algorithm

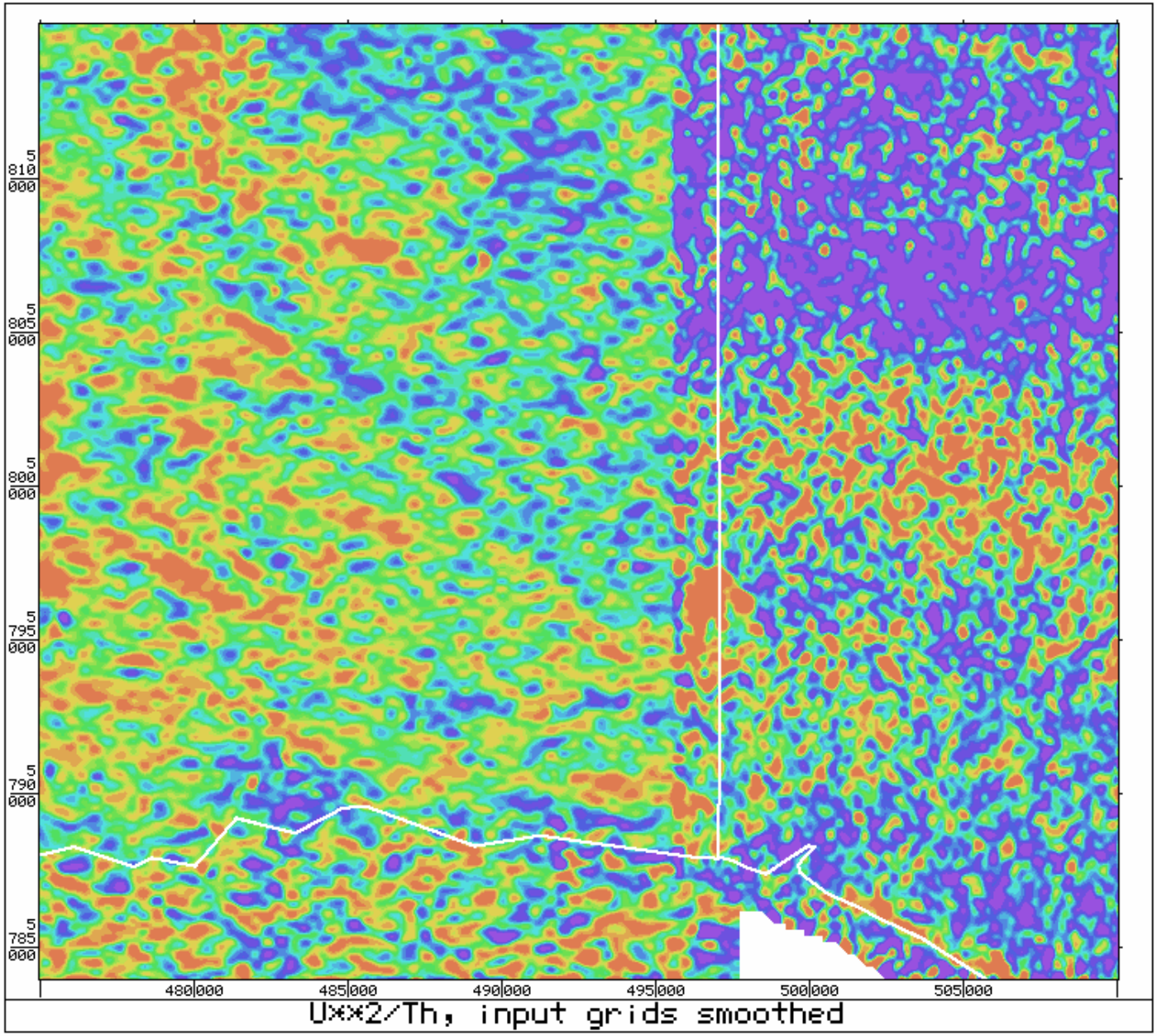

Figure 73. (Uranium squared)/Thorium

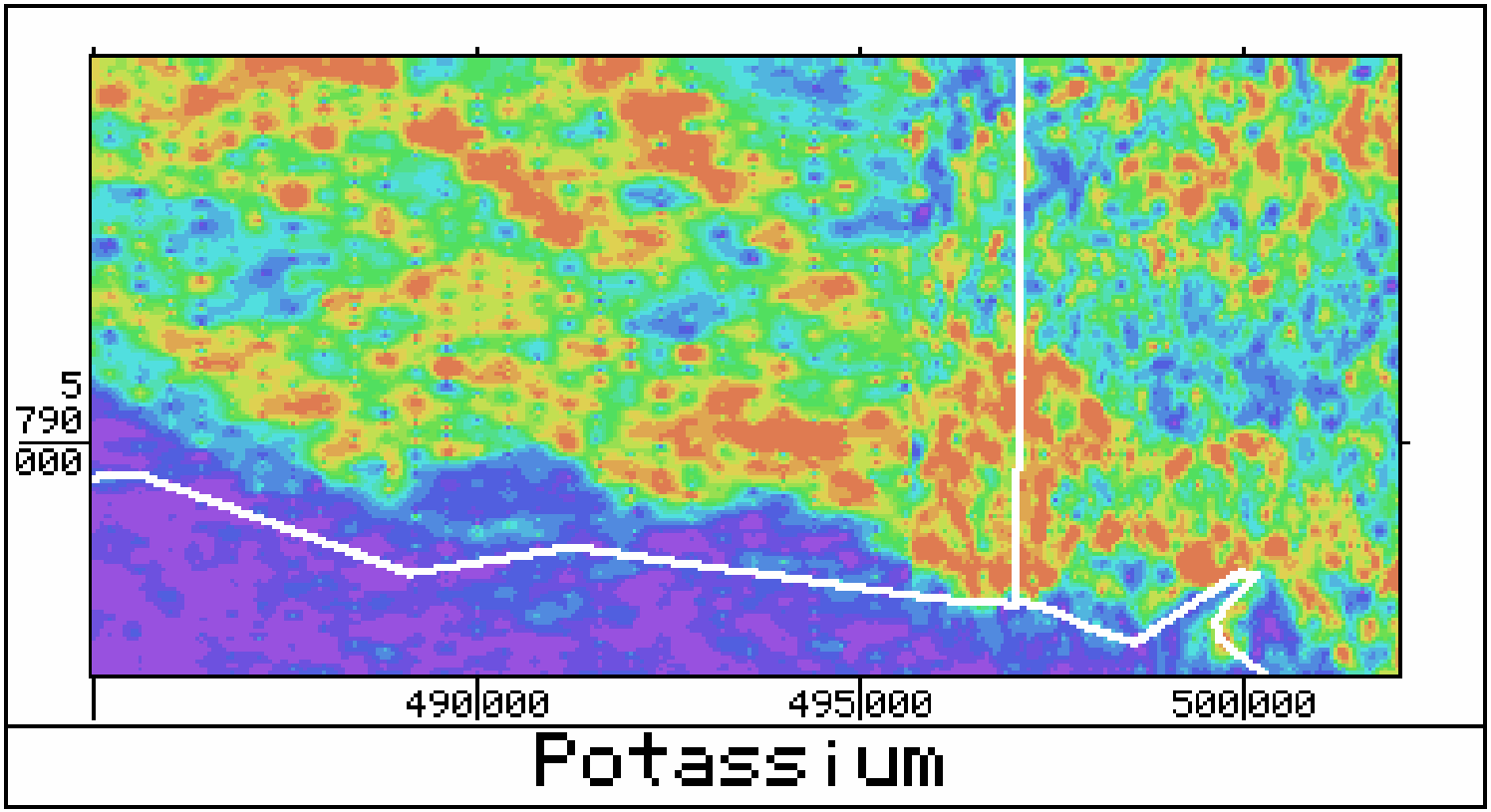

Figure 74. Potassium

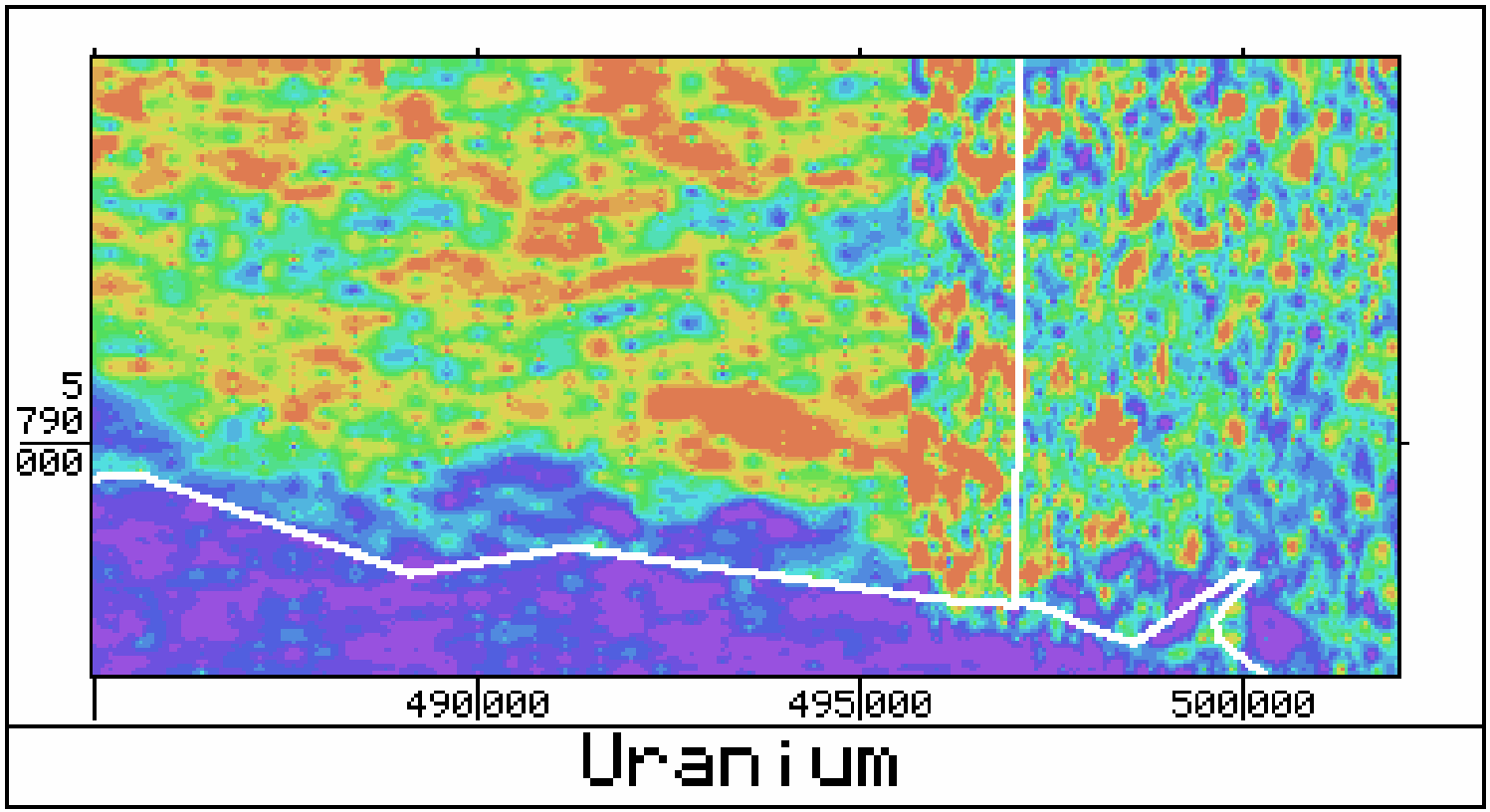

Figure 75. Uranium

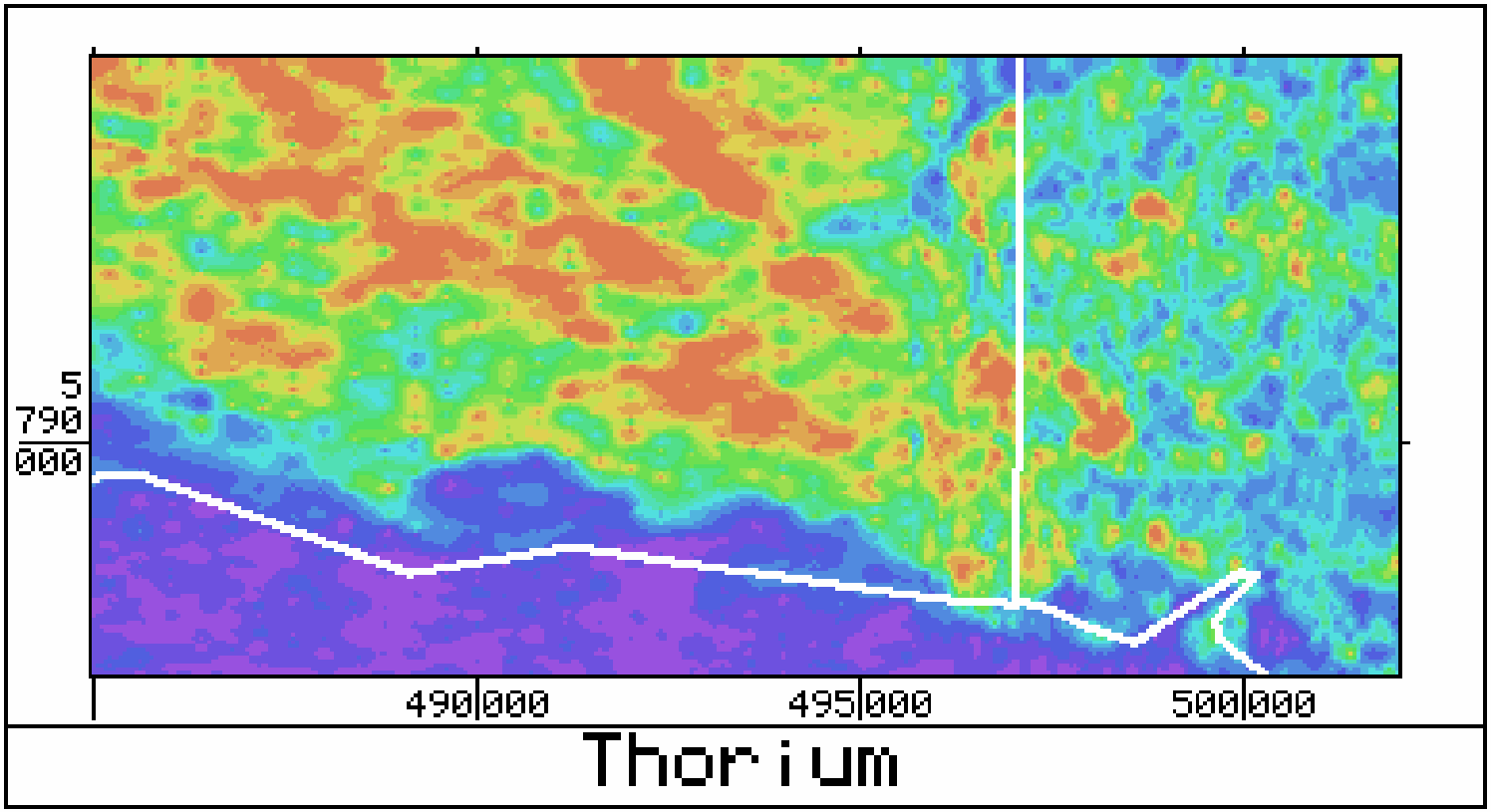

Figure 76. Thorium

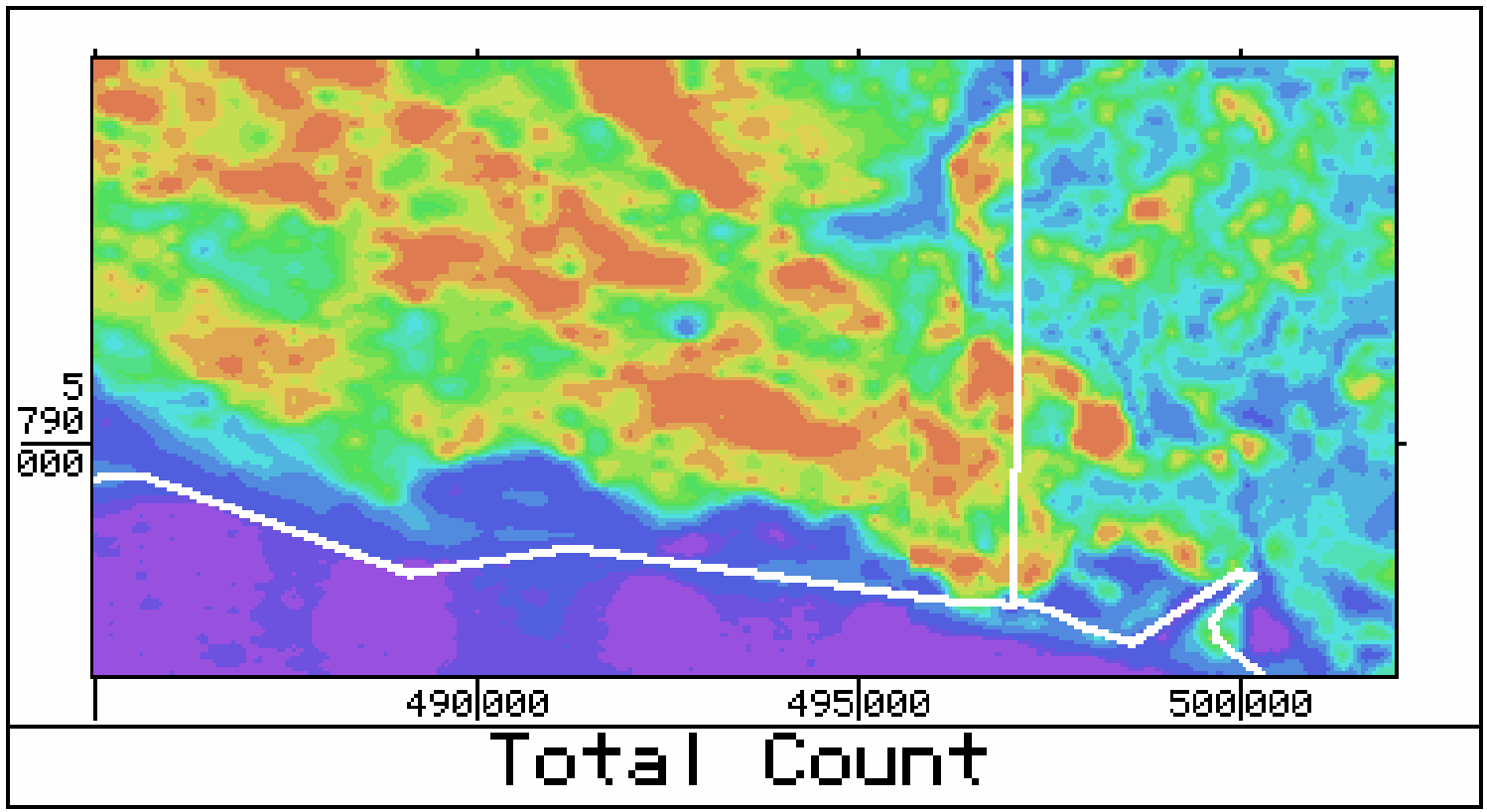

Figure 77. Total Count

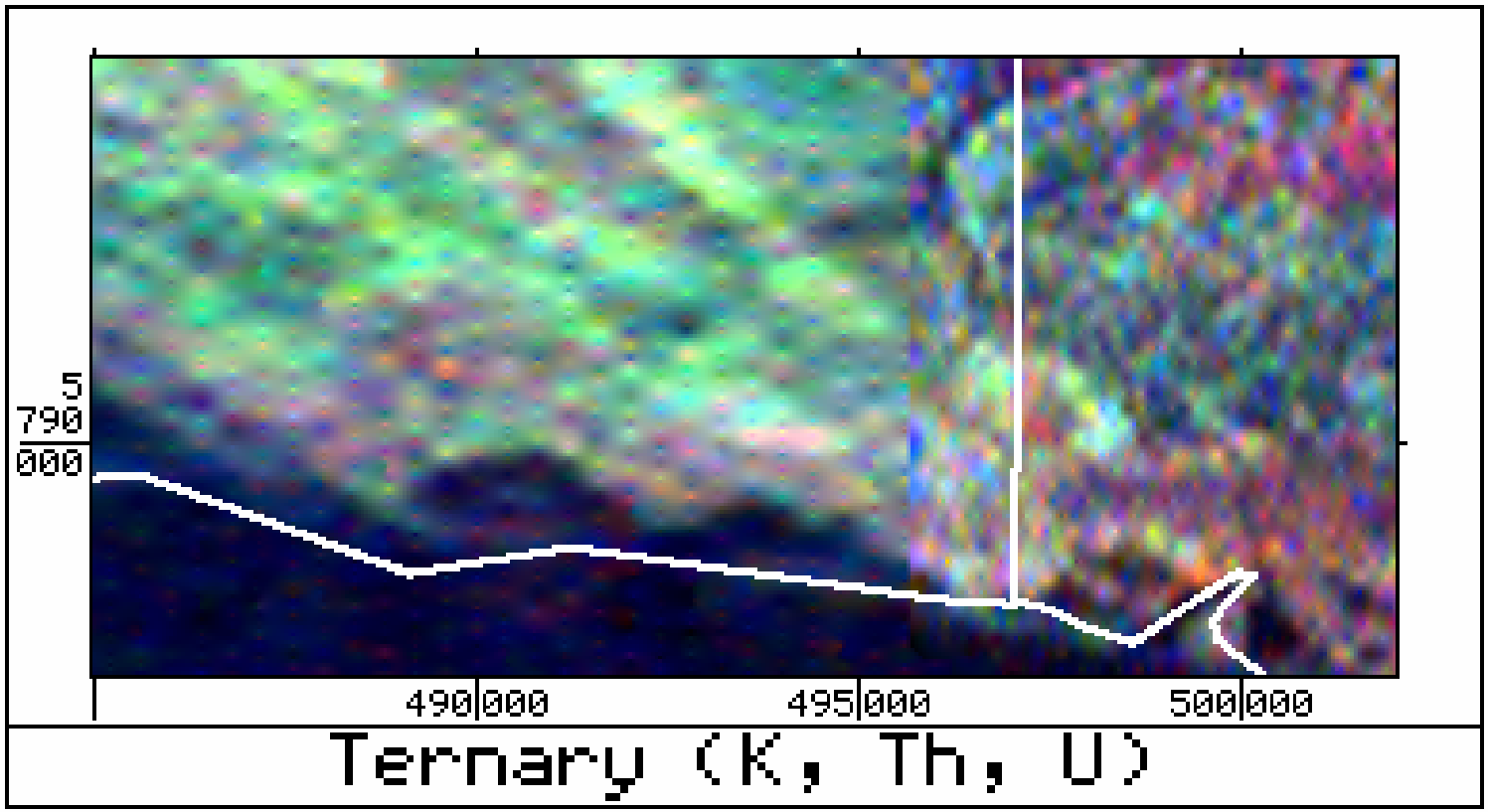

Figure 78. Radiometric ternary plot

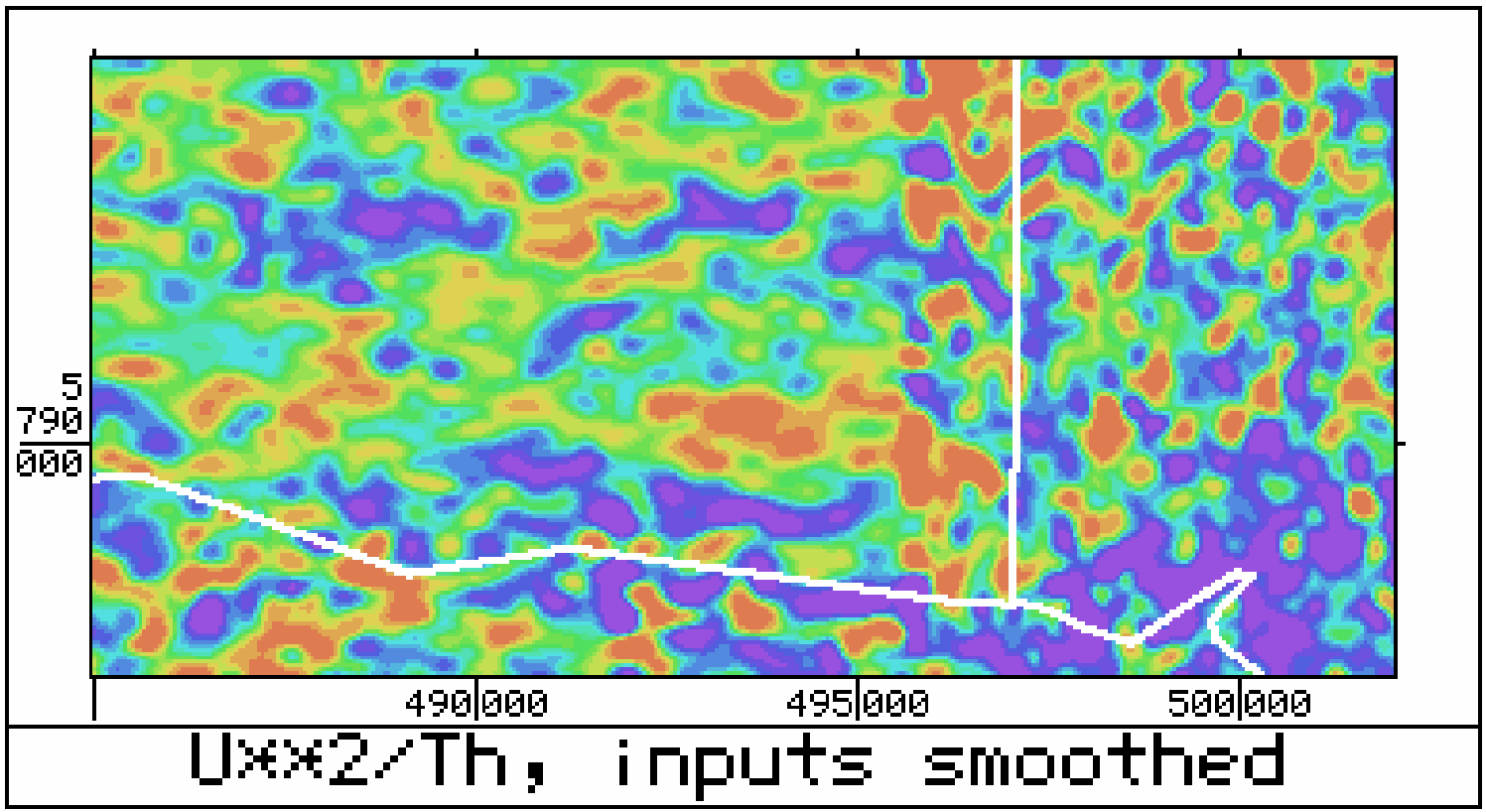

Figure 79. (Uranium squared)/Thorium

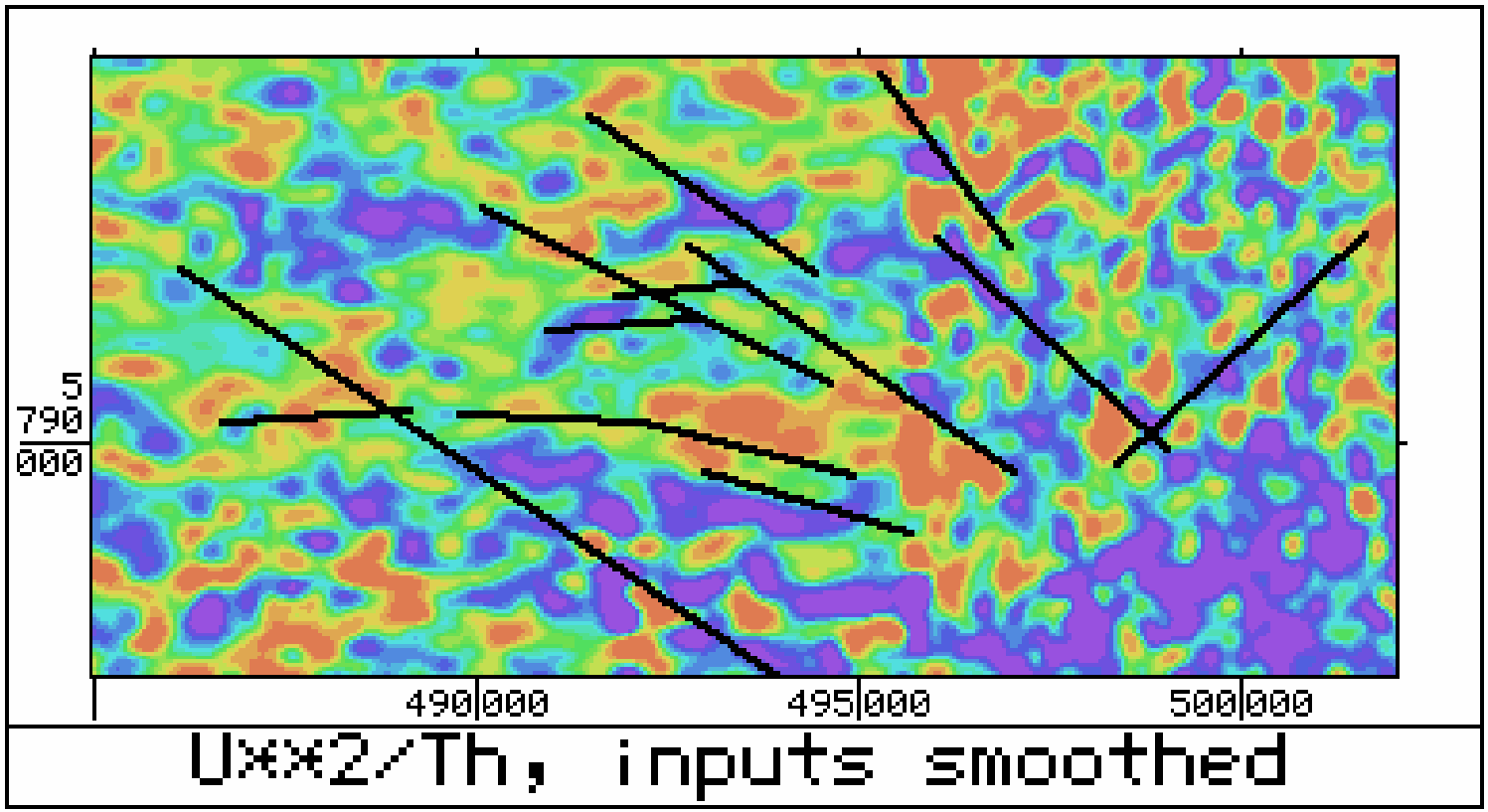

Figure 80. (Uranium squared)/Thorium, with magnetic lineations

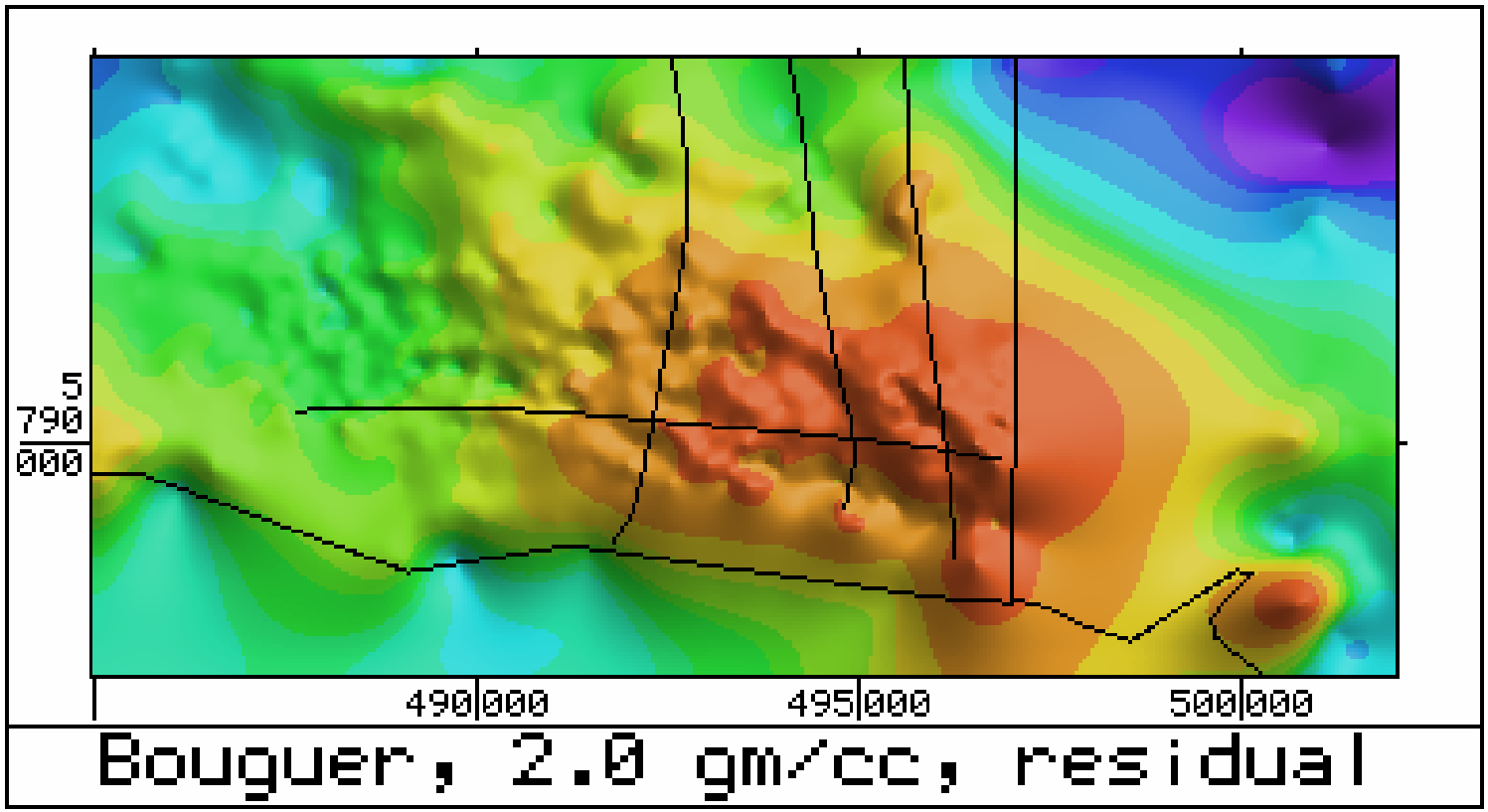

Figure 81. Bouguer gravity, 2.0 gm/cc, residual, with seismic lines

APPENDIX 2

PROCESSING CONTRACTORS REPORT (PHASE 2)

Stewart Geophysical Consultants P/L

Additional gravity data over the Summer Hill Prospect, southeast South Australia

prepared for

Origin Energy Resources Ltd.
GPO Box 148
Brisbane
Queensland 4001

by

Stewart Geophysical Consultants Pty. Ltd.
44 Harrow Road
College Park
South Australia 5069
Australia
Phone/Fax: 61-8-8363 3635
Email: stewgeop@senet.com.au

November 2002

Contents

List of Figures

Additional gravity data over the Summer Hill prospect, southeast South Australia

Introduction

The Summer Hill prospect, in the extreme southeast part of South Australia, is poorly covered by AGSO gravity data, as shown in Figure 1, which includes 611 gravity stations. Hence a gravity survey over the area was conducted in May 2002, during which 556 stations were observed within the area of interest. The new stations superseded the existing coverage, and a total of 1114 stations from the merged data set are plotted in Figure 2. The gravity grid using a Bouguer density of 2.0 gm cm^{-3} for the first survey is shown in Figure 3. The residual was obtained using a two-dimensional Hamming filter 25 km across in order to minimise the strong regional trend and is shown in Figure 4, where locally high values are red. The horizontal gradient employing an anisotropic operator 500 m wide is plotted in Figure 5. Local maxima in the gradient (red) should correspond to marked lateral changes in density, such as faults.

It can be seen that the anomaly maximum is close to the eastern margin of the gravity survey, while immediately to the east of the State border there is a gap of about 3 km in the gravity coverage (cf. Figure 2). There are several well-defined lineations or trends within the data, but the eastern extent of the structure remains undefined in Figures 3 through 5. Hence additional gravity acquisition has been undertaken in order to resolve the outline of the anomaly. The new data have been merged with the previous survey data, and these have then been incorporated into the regional coverage. In addition to the merged data sets and grids, several enhancements are also included with this report.

The UTM coordinates used for all the mapping here are given as AMG66 zone 54 values, as the existing data sets are based on this datum. All gravity values are in milligals. Most of the maps are presented as colour bitmaps, where the size of the text is related to the pixel or grid cell size. The UTM coordinate ticks are mainly at 5 or 10 km intervals, and the location of any pixel can be found readily on the screen by using the cursor to count the numbers of pixels from a plotted coordinate mark. Where shading has been used for the coloured diagrams the illumination is from the northeast for most of the images. Generally the detail and colour contrasts are better when viewed on the screen than on the paper prints given in this report, and hence the bitmap image files are included as digital products with this report.

Gravity data

The new gravity data set included 237 observations, some of which were repeat and base stations. As before, most of the stations were nominally on a 250 by 250 m grid, with a more irregular spacing in areas of difficult access, such as the National Park in the northeast and along the coast. If all duplicate stations, including multiple base readings, are removed then the number of new gravity points is reduced to 196. Some of the new stations coincided with stations from the earlier survey as a check on the consistency of the data. Generally the repeat values agreed reasonably well, within a few hundredths of

a milligal of the previous readings. Duplicate points were also removed when the data were merged for the 2 separate surveys, to give the 730 points shown in Figure 6.

Terrain corrections were applied to the gravity survey, since even small corrections of a tenth of a milligal or less may be significant when the anomalies being studied are only of the order of one or two milligals. A digital terrain model (DTM) had been generated previously using data from two regional airborne surveys. However in some places the DTM differed by more than 10 m from the gravity heights, due to inaccuracies in the airborne data. This would lead to significant and quite erroneous terrain corrections for the gravity if only the DTM grid from the airborne data were to be used for the corrections. Hence the heights from the gravity survey stations were used to create a more reliable, although less detailed, elevation grid in the survey area, and this was then merged with the regional grid, as shown in Figure 7. The expected gravity terrain corrections were estimated at 200 m intervals across the survey area for a density of 2.67 gm cm^{-3} and are shown in Figure 8, where the maximum value is 0.25 milligal. The terrain corrections were then calculated exactly at each of the new station locations and used to give a final corrected Bouguer value for merging and gridding. Generally the corrections were only a few hundredths of a milligal, with a maximum of about 0.16 milligal for a density of 2.67 gm cm^{-3}.

A density of 2.67 gm cm^{-3} was used for the initial Bouguer reduction of the gravity data. While this density is often employed for routine gravity work, it is more appropriate to use a lower value in sedimentary environments. Hence gravity data sets, including terrain corrections, and plots were also generated for Bouguer densities of 2.40, 2.20, 2.00 and 1.80 gm cm^{-3}. These would correspond to a typical sedimentary rock, through to poorly consolidated or weathered sediments, and unconsolidated material such as sand. The terrain-corrected Bouguer values were gridded at a 50 m interval using minimum curvature routines, and are shown for densities of 1.8, 2.0 and 2.2 gm cm^{-3} in Figures 9, 10 and 11 respectively. Although there are no large variations in the topography, a change in the Bouguer density has a noticeable effect on the patterns observed in the gravity plot. There are significant lineations in the gravity plots, which may be related in part to topographic effects. The grids were therefore used to determine an optimum Bouguer density. In this process residual grids derived with an operator 5 km across were used to remove the regional trends and hence enable the local variations in the gravity field to be correlated with the topography. A minimum in the cross correlation of the elevation and residual grids was achieved for a Bouguer density of about 1.8 gm cm^{-3}, as expected from the surface lithology of the area. Data corrected with this density are therefore probably the most appropriate to use for gravity mapping and analysis in this area.

The corrected data were then merged with the existing regional data set, where old stations were discarded where they lay within the area of the new data. The locations of the merged data are plotted in Figure 12, which contains 1270 stations. The adjustment required to merge the data sets was found by the offset between old values and the grid of the new data at each AGSO station location. Only a small shift of –0.07 milligal was applied to the AGSO values for Bouguer data with a density of 1.8 gm cm^{-3}, where the offset reduced to zero for a density of 2.67 gm cm^{-3}. A 50 m grid of the merged data for a density of 1.8 gm cm^{-3} is shown in Figure 13, while the residual obtained with a 25 km operator is shown in Figure 14. The Bouguer and residual grids for a density of 2.0 gm

cm^{-3} are given in Figures 15 and 16, and are also shown over just the survey area in Figures 17 and 18. The residual is also plotted in Figure 19, where the shading is by illumination from the southeast, in order to highlight northeasterly trends in the data, although there are few prominent trends in this direction. The residual plot in Figure 20 includes the locations of 4 seismic lines over the prospect, and the horizontal gradient is given in Figure 21.

Conclusion

The additional gravity data has enabled the eastern extent of the Summer Hill anomaly to be defined reasonably well. From Figures 18 and 19 the peak of the anomaly extends about 1 km to the east of the border, and also appears to trend in a more southerly direction at its eastern end. This is also indicated by the gradient in Figure 21, where strong north-south gradients can be seen at about 497000 m E. These appear to terminate the prominent northwesterly trend which occurs to the west of the border, although there is a weaker trend in the same direction near the coast to the east of around 498000 m E. Thus the trends parallel to the border may in fact offset the more regional northwesterly lineation. This may then have some bearing on the basement structure underlying the anomaly, which could be fairly complex if it is controlled by the intersection of two fault patterns. While the gravity data suggest that most of the structure lies to the west of the State border, it probably extends up to about 1 km into Victoria.

List of digital products (data, grids and images)

All grids are in ERMapper format, with a binary grid and an ASCII (*.ERS) header file.

1) SUMMER2.DOC
   Word document of text of Summer Hill gravity report.

2) GRAVSURV.DAT
   ASCII file of gravity data from new survey, including terrain corrections.
   26 fields (see format listing)

3) GRAVMERG.DAT
   ASCII file of merged gravity data, densities 1.8, 2.0, 2.2, 2.4 and 2.67 gm cm^{-3}.

4) ALLCSV1.CSV
   Raw ASCII data from first gravity survey (May 2002).

5) ALLCSV2.CSV
   Raw ASCII data from second gravity survey (October 2002).

6) BOUG180.ERS
   Grid of merged gravity, 50 m interval, density 1.8 gm cm^{-3}.

7) BOUG200.ERS
   Grid of merged gravity, 50 m interval, density 2.0 gm cm^{-3}.

8) B180RES.ERS
   Grid of gravity residual, density 1.8 gm cm^{-3}.

9) B20RES.ERS
   Grid of gravity residual, density 2.0 gm cm^{-3}.

10) B180GRAD.ERS
    Grid of gravity horizontal gradient, prospect area, density 1.8 gm cm^{-3}.

11) FIGURE*.BMP
    Bitmap images of the coloured diagrams in this report

12) FIGURE*.PGL
    Line diagrams in HPGL format

Format of ASCII gravity data set, both new surveys (GRAVSURV.DAT)

All coordinates are based on the ANS (AMG) spheroid. Gravity values are in milligals

1.	Line number	I8
2.	Station number	I8
3.	AMG66 zone 54 Easting (metres)	F12.2
4.	AMG66 zone 54 Northing (metres)	F12.2
5.	Longitude	F12.7
6.	Latitude	F12.7
7.	Elevation (metres)	F10.3
8.	Observed gravity	F12.3
9.	Anomalous gravity	F10.3
10.	Free-Air correction	F10.3
11.	Bouguer correction (2.67 gm cm^{-3})	F10.3
12.	Bouguer anomaly (2.67 gm cm^{-3})	F10.3
13.	Terrain correction (2.67 gm cm^{-3})	F10.3
14.	Corrected Bouguer (2.67 gm cm^{-3})	F10.3
15.	Bouguer (2.4 gm cm^{-3})	F10.3
16.	Terrain correction (2.4 gm cm^{-3})	F10.3
17.	Corrected Bouguer (2.4 gm cm^{-3})	F10.3
18.	Bouguer (2.2 gm cm^{-3})	F10.3
19.	Terrain correction (2.2 gm cm^{-3})	F10.3
20.	Corrected Bouguer (2.2 gm cm^{-3})	F10.3
21.	Bouguer (2.0 gm cm^{-3})	F10.3
22.	Terrain correction (2.0 gm cm^{-3})	F10.3
23.	Corrected Bouguer (2.0 gm cm^{-3})	F10.3
24.	Bouguer (1.8 gm cm^{-3})	F10.3
25.	Terrain correction (1.8 gm cm^{-3})	F10.3
26.	Corrected Bouguer (1.8 gm cm^{-3})	F10.3

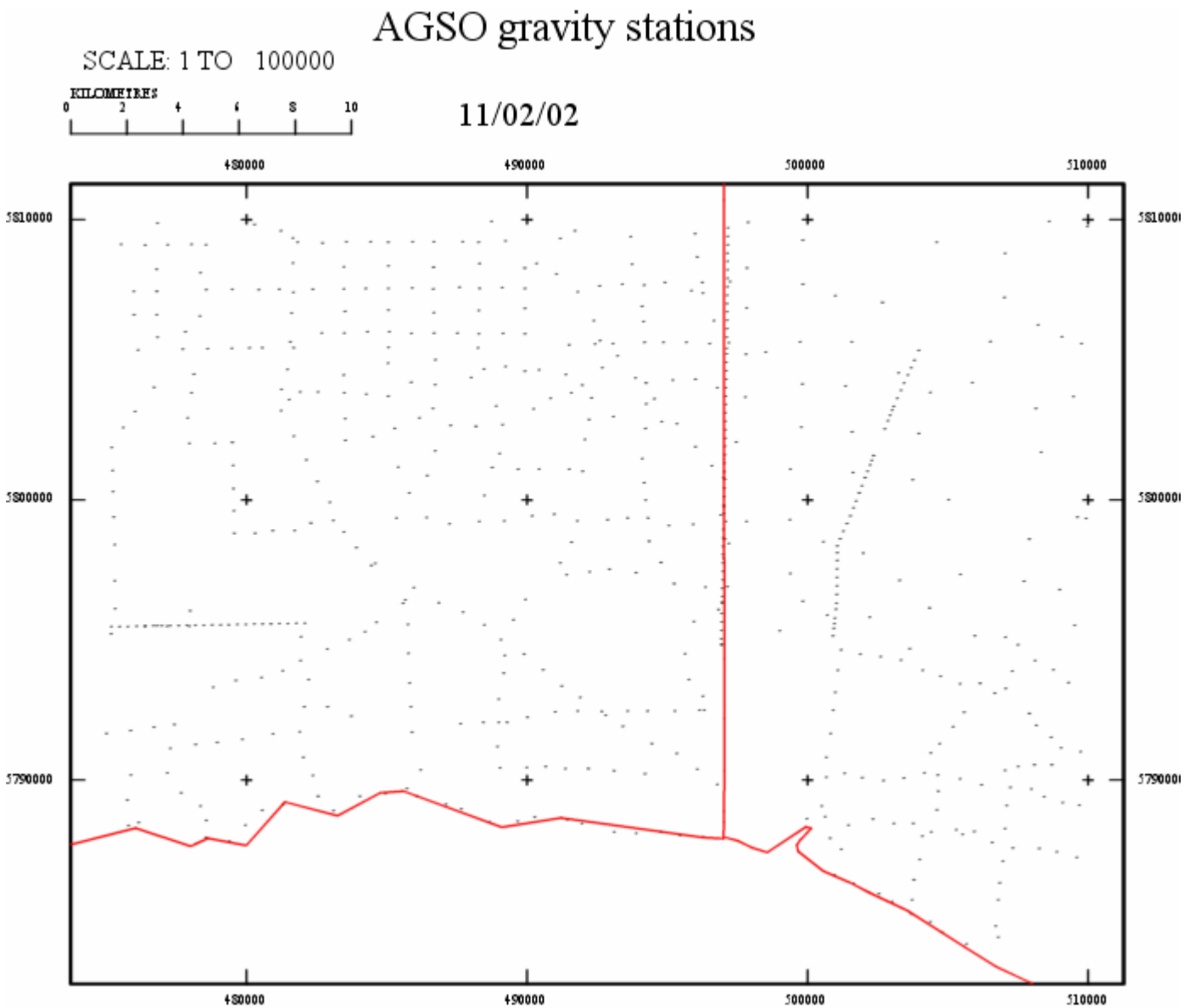

Figure 1 – AGSO Gravity Stations in Southeast South Australia and Western Victoria

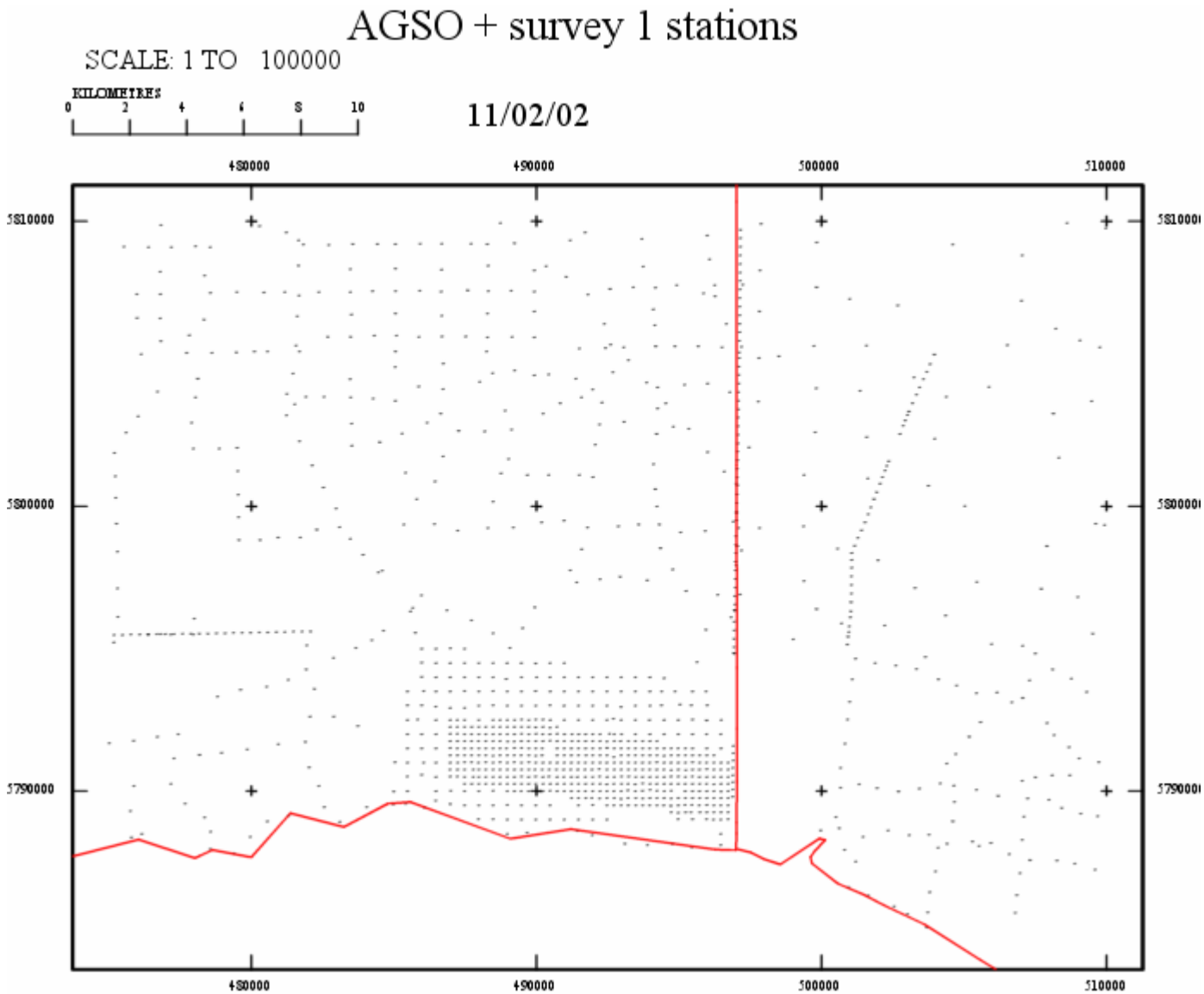

Figure 2 – Merged Regional Data and Gravity Stations from Summer Hill Phase 1

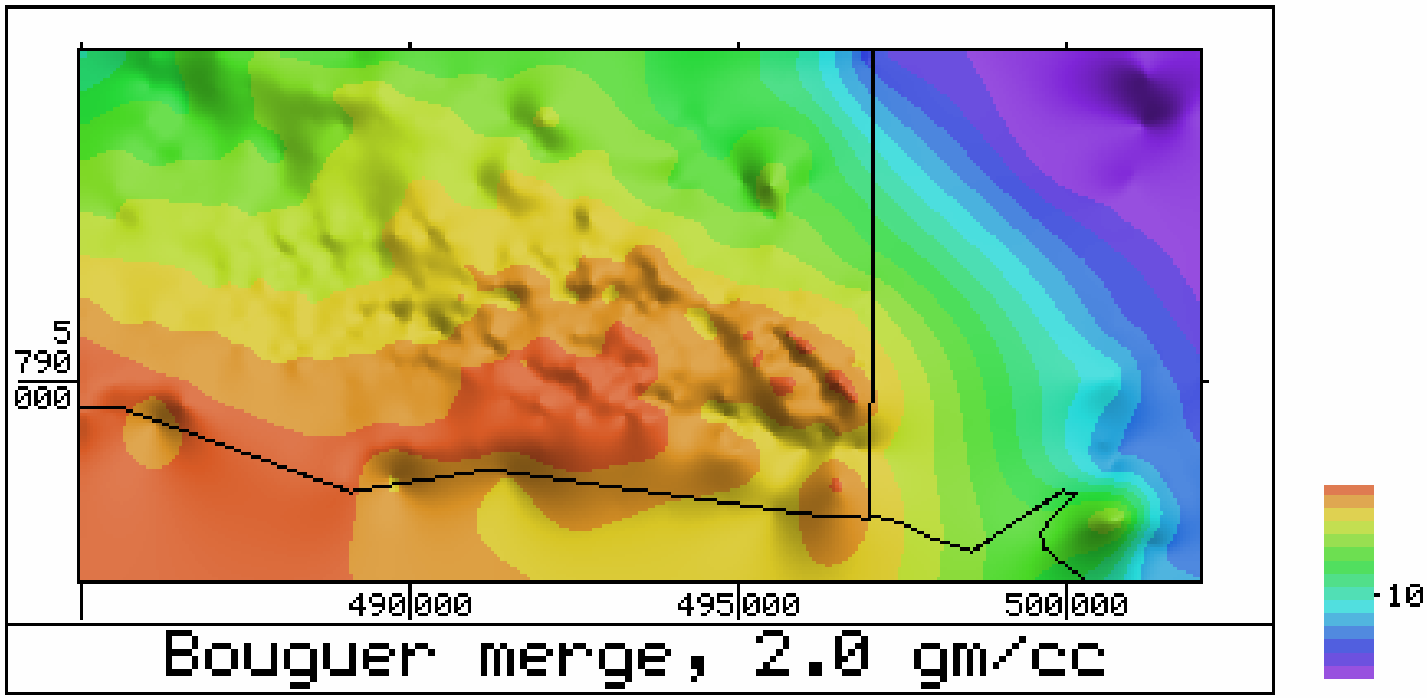

Figure 3. Bouguer gravity, first survey
Colour interval 0.4 milligal

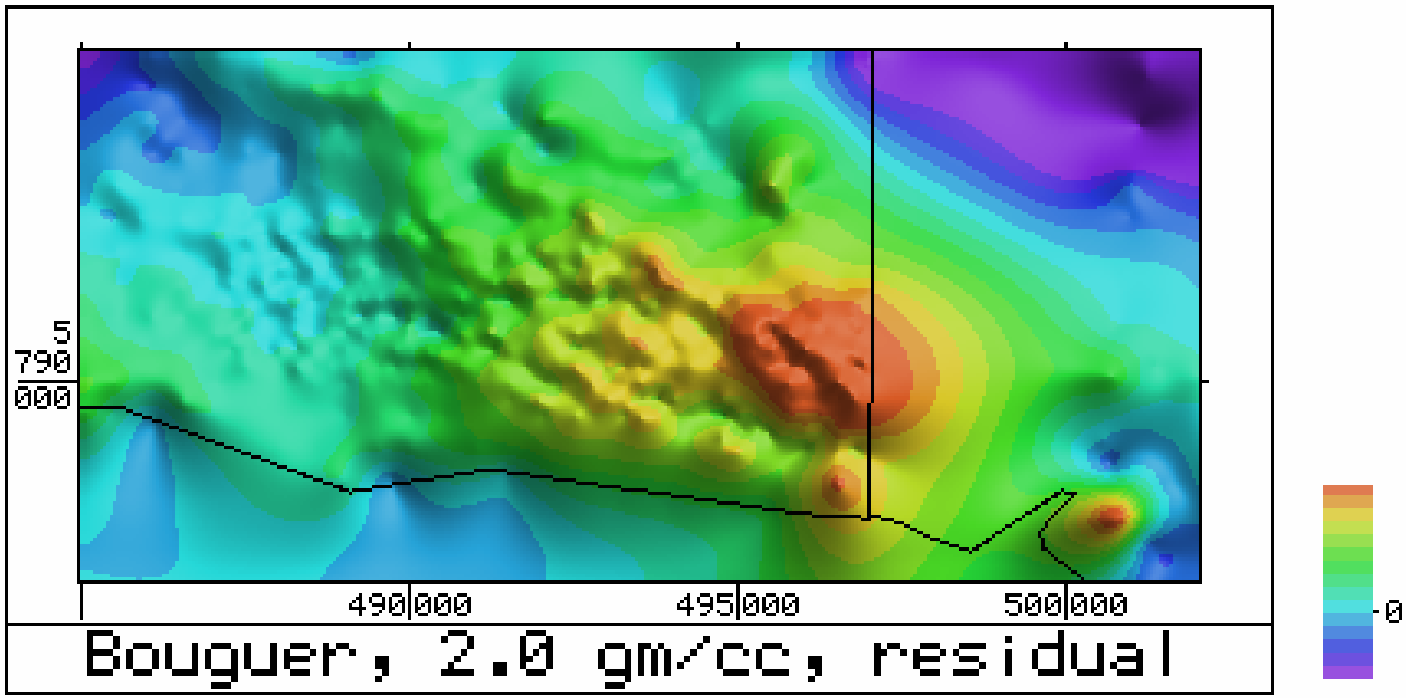

Figure 4. Bouguer gravity, first survey
Residual, colour interval 0.2 mgal

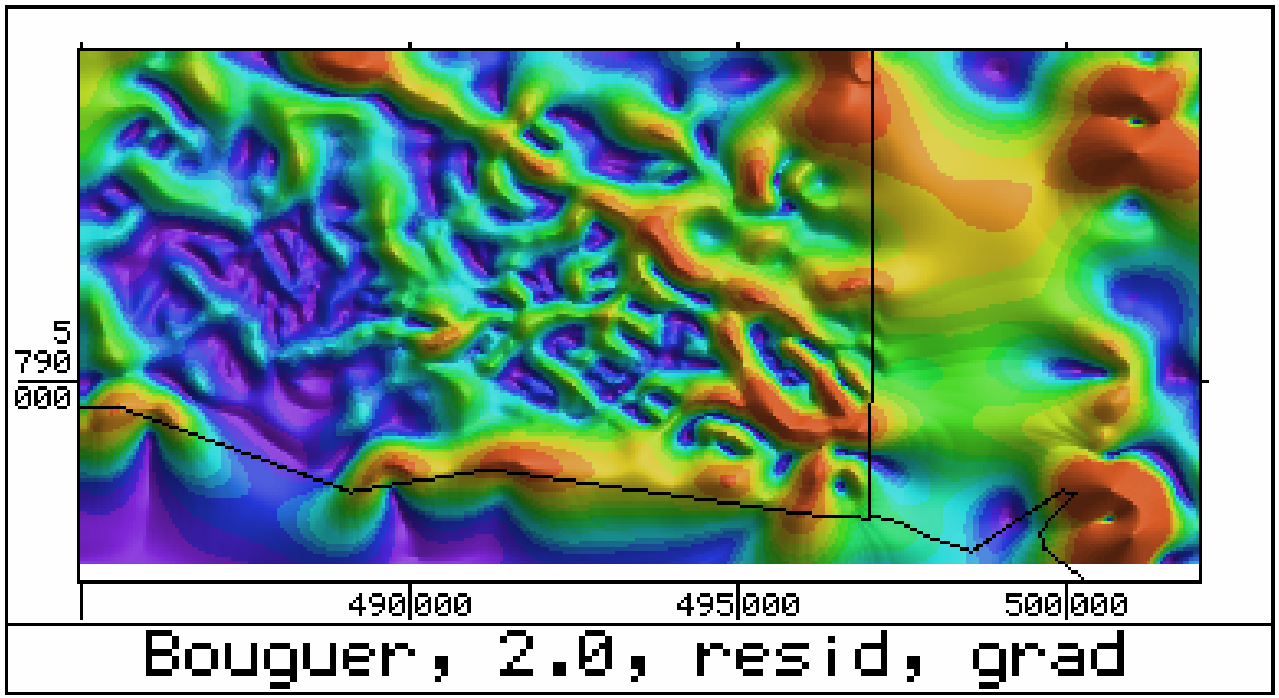

Figure 5. Bouguer gravity, first survey
Horizontal gradient

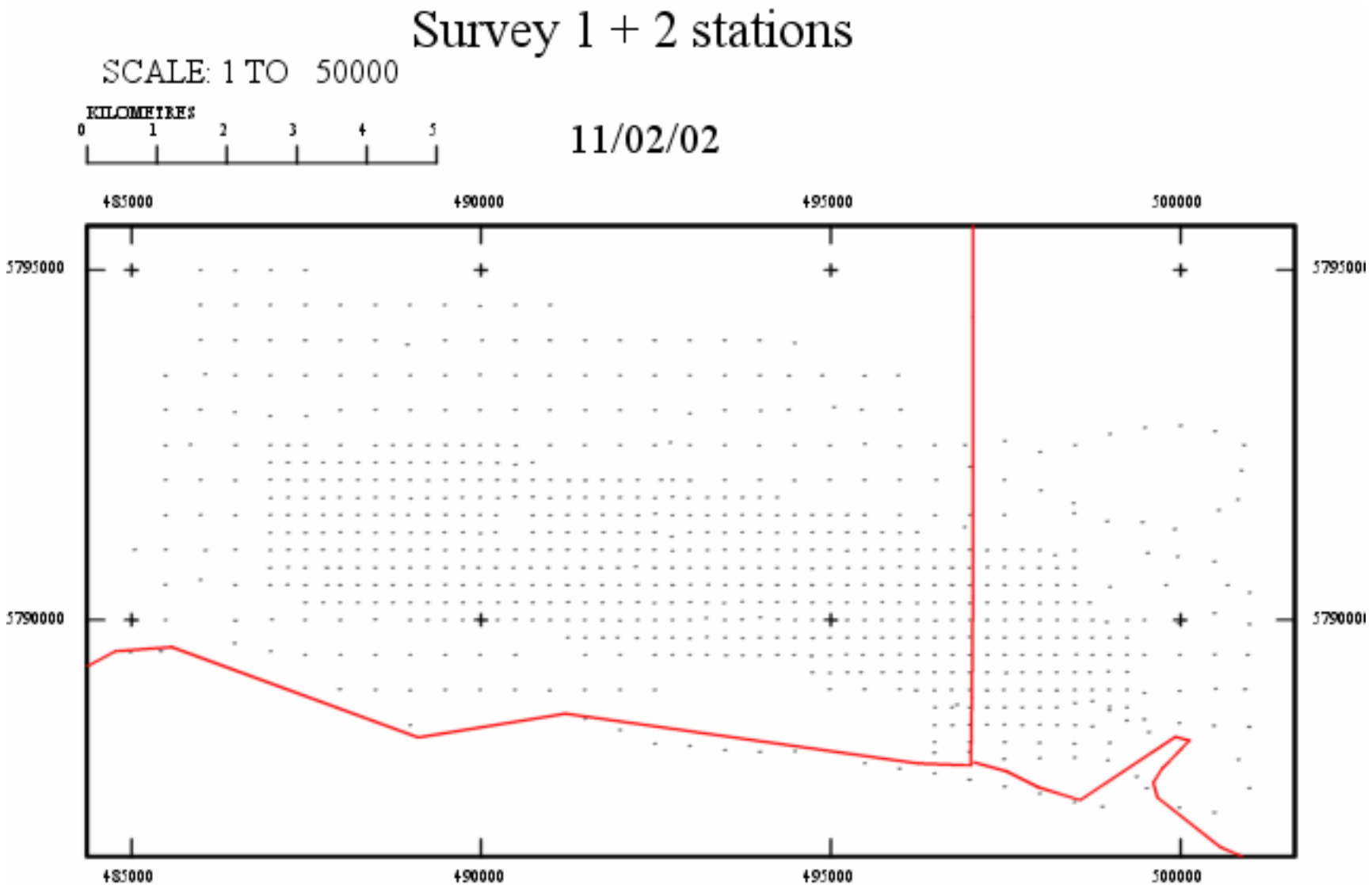

Figure 6 – Station Locations, Summer Hill Gravity Survey

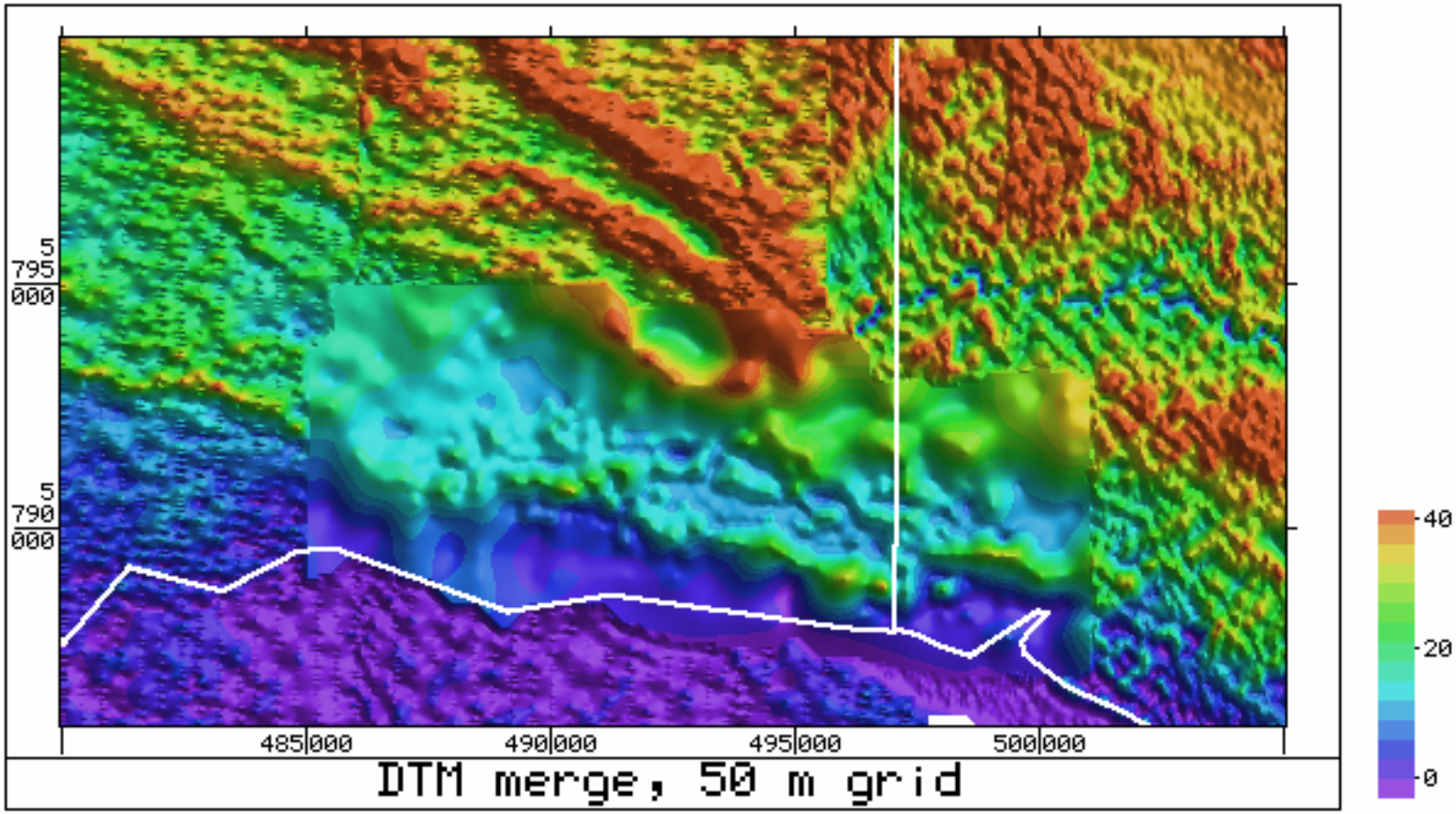

Figure 7. Digital terrain model from merged airborne and gravity station data

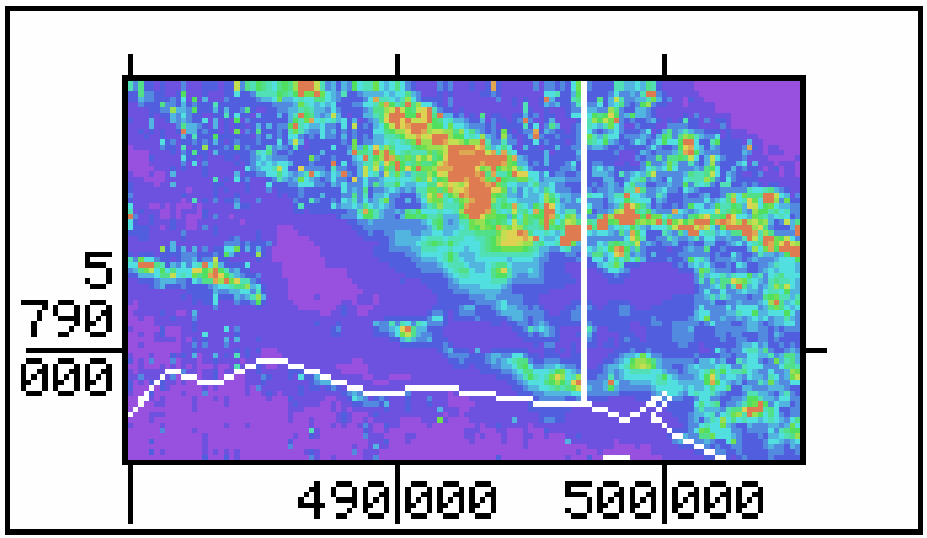

Figure 8. Terrain corrections, 2.67 gm/cc
Colour interval 0.005 milligal

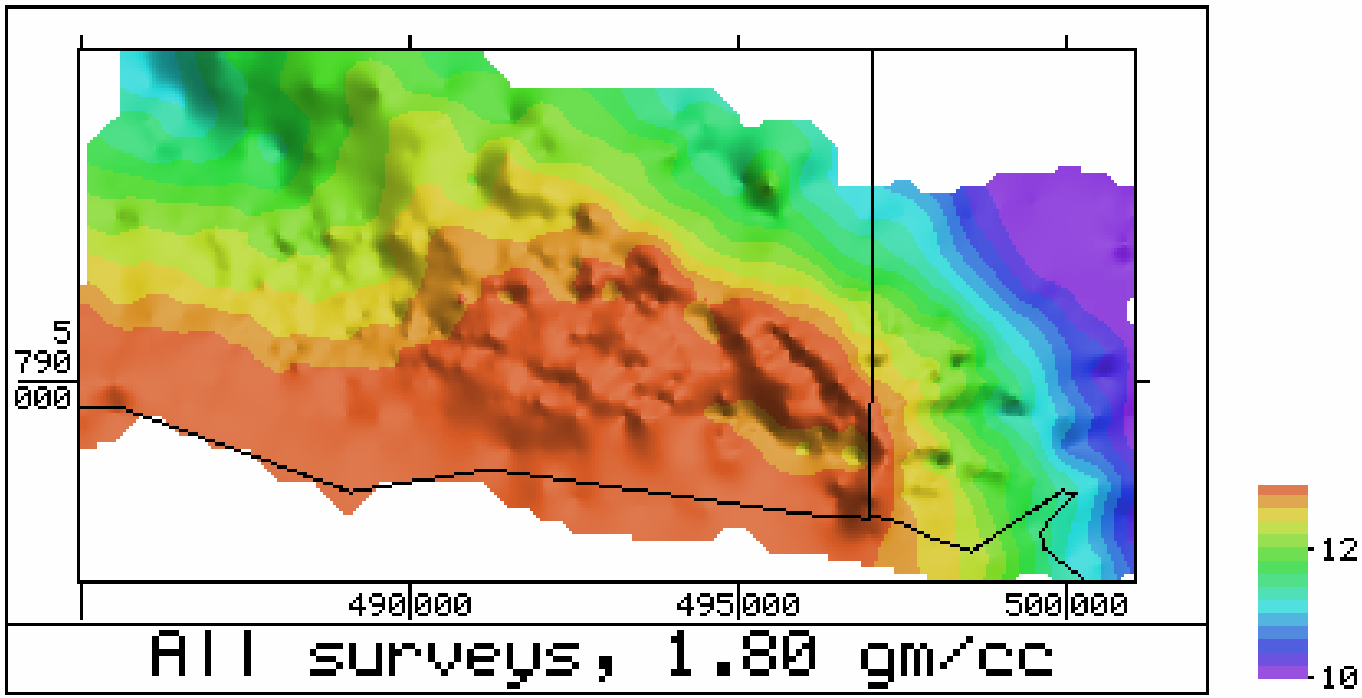

Figure 9. Bouguer gravity, 1.8 gm/cc
Data from both new surveys

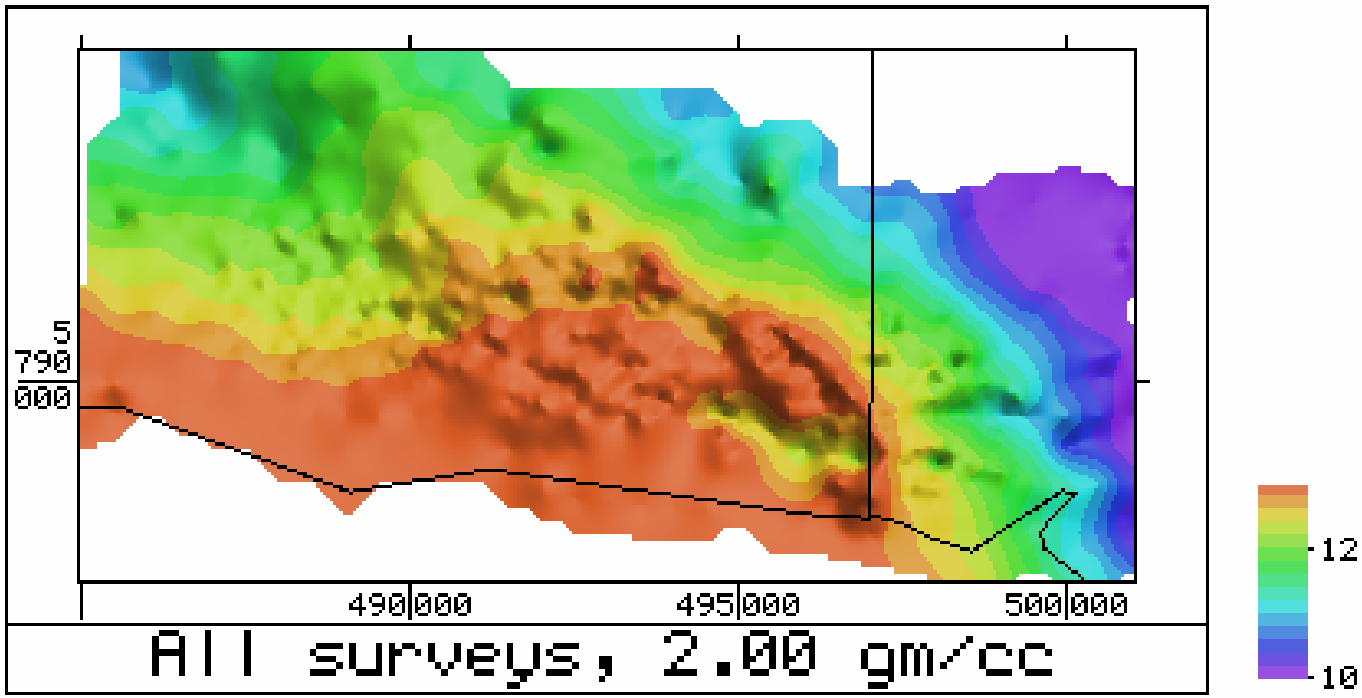

Figure 10. Bouguer gravity, 2.0 gm/cc
Data from both new surveys

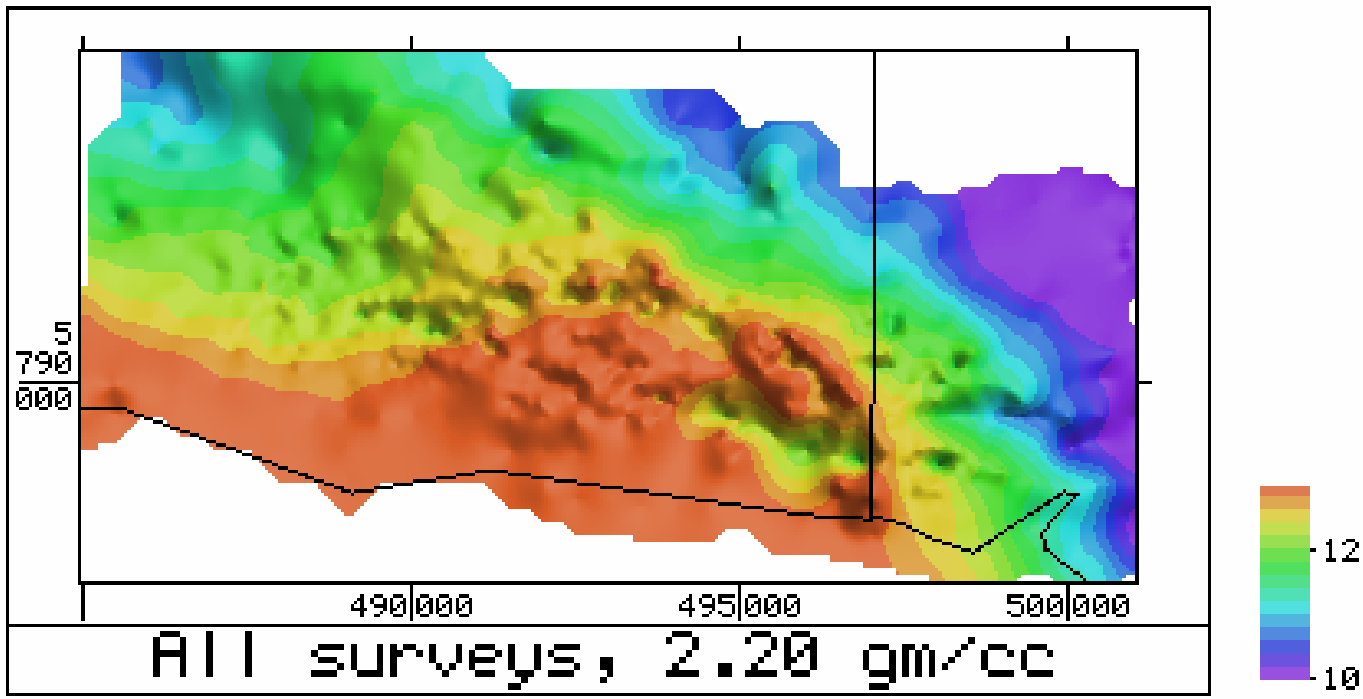

Figure 11. Bouguer gravity, 2.2 gm/cc
Data from both new surveys

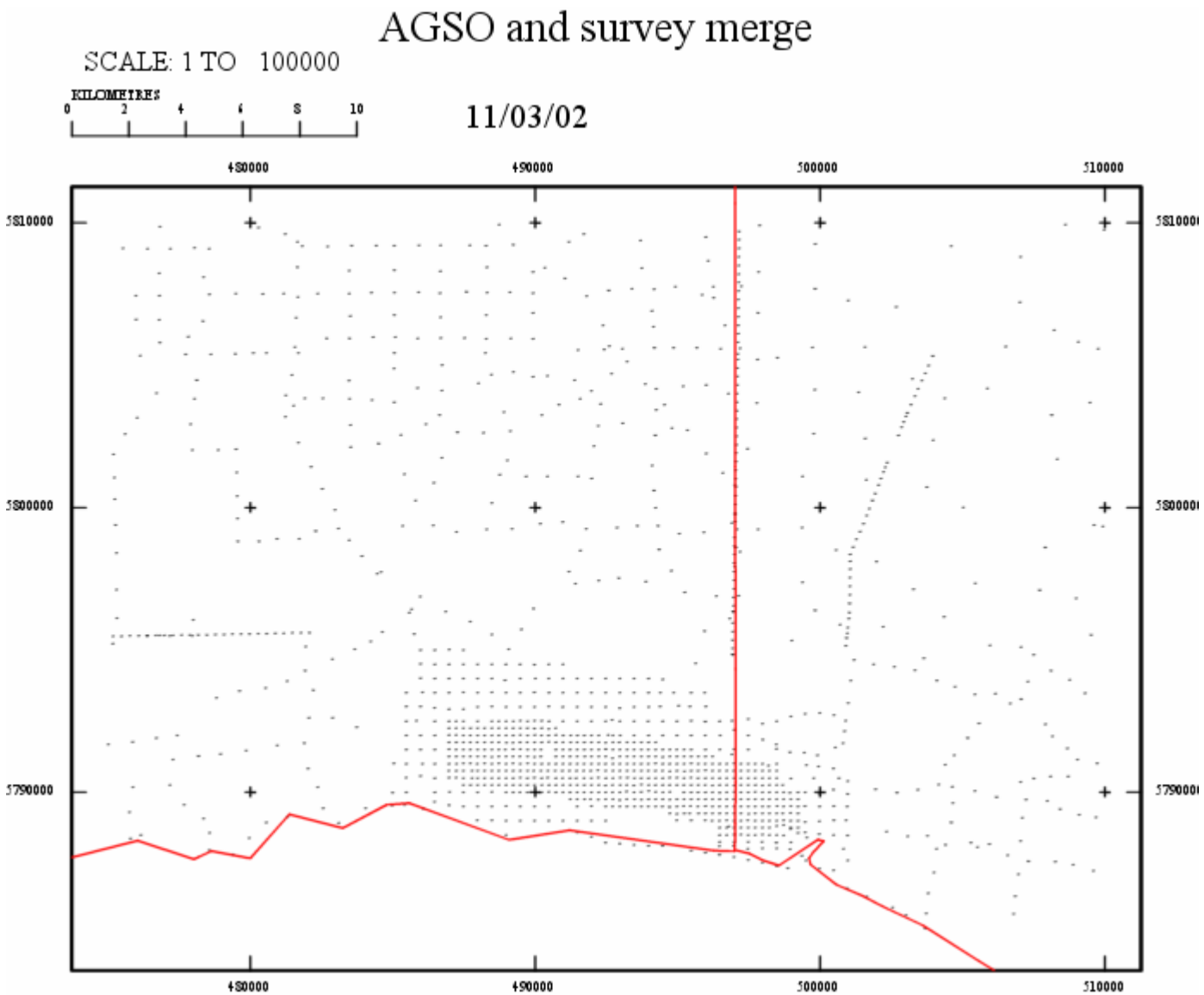

Figure 12 – Gravity Stations from Merged Regional Data & Summer Hill Survey

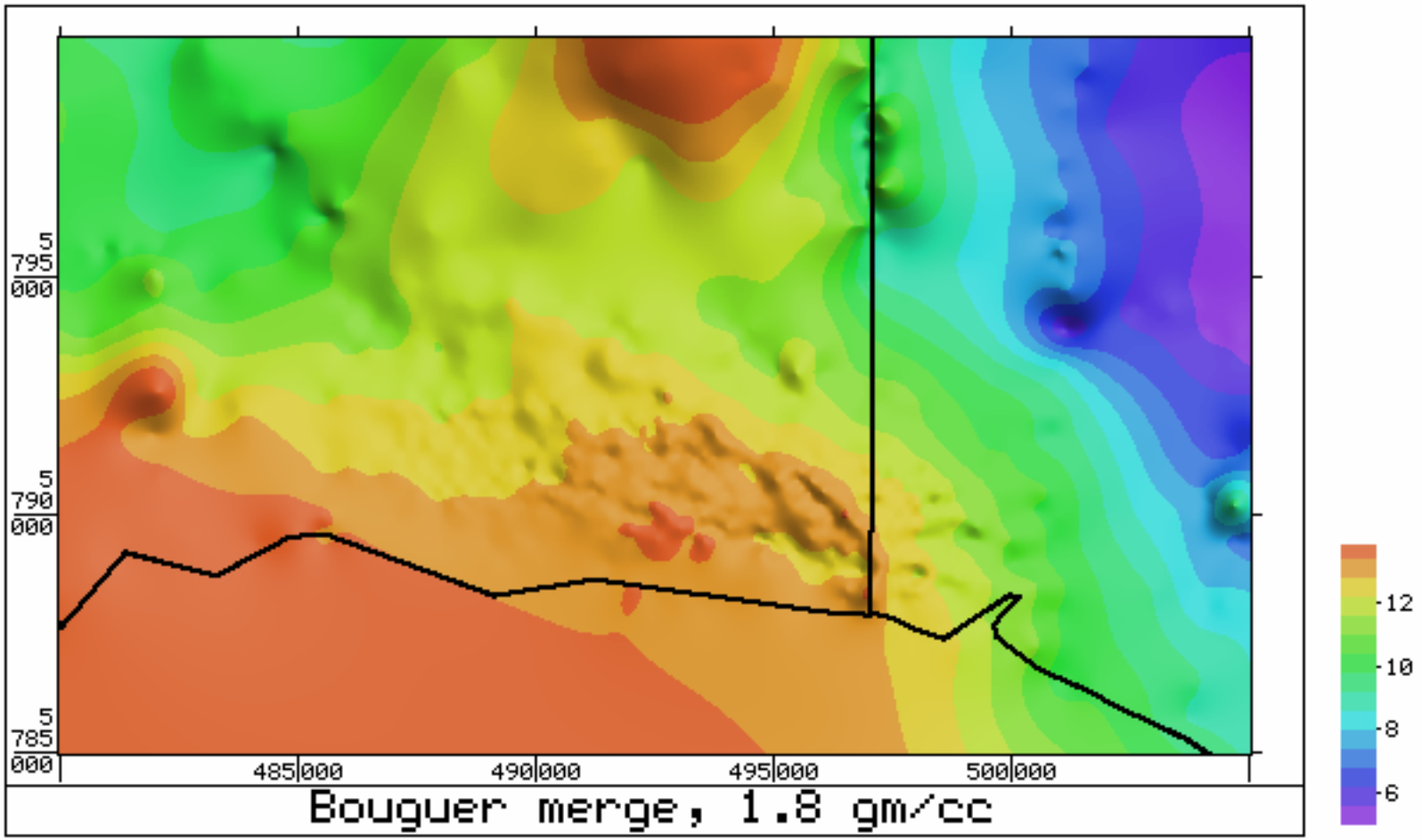

Figure 13. Merged Bouguer gravity, 1.8 gm/cc

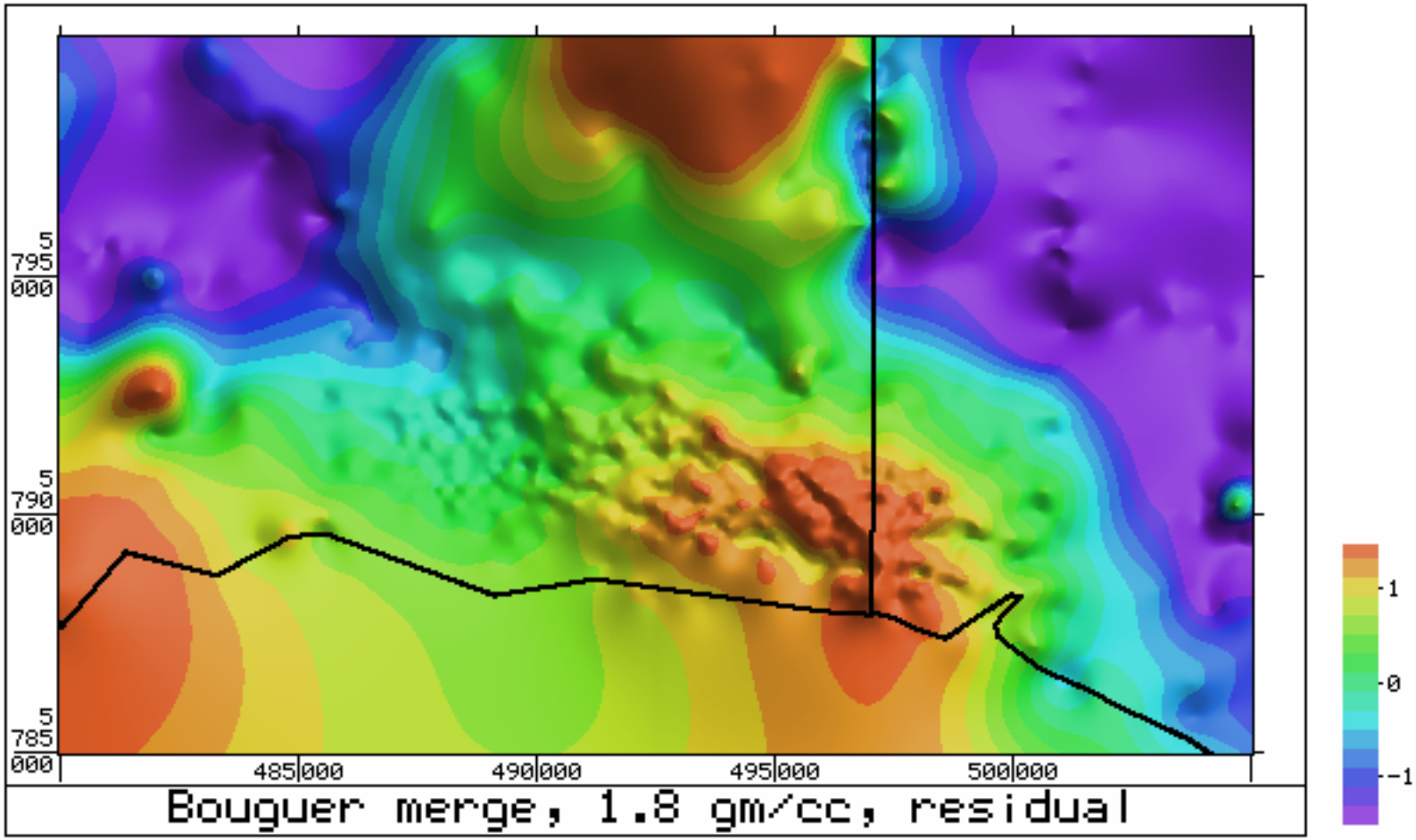

Figure 14. Merged Bouguer gravity, 1.8 gm/cc Residual, 25 km operator

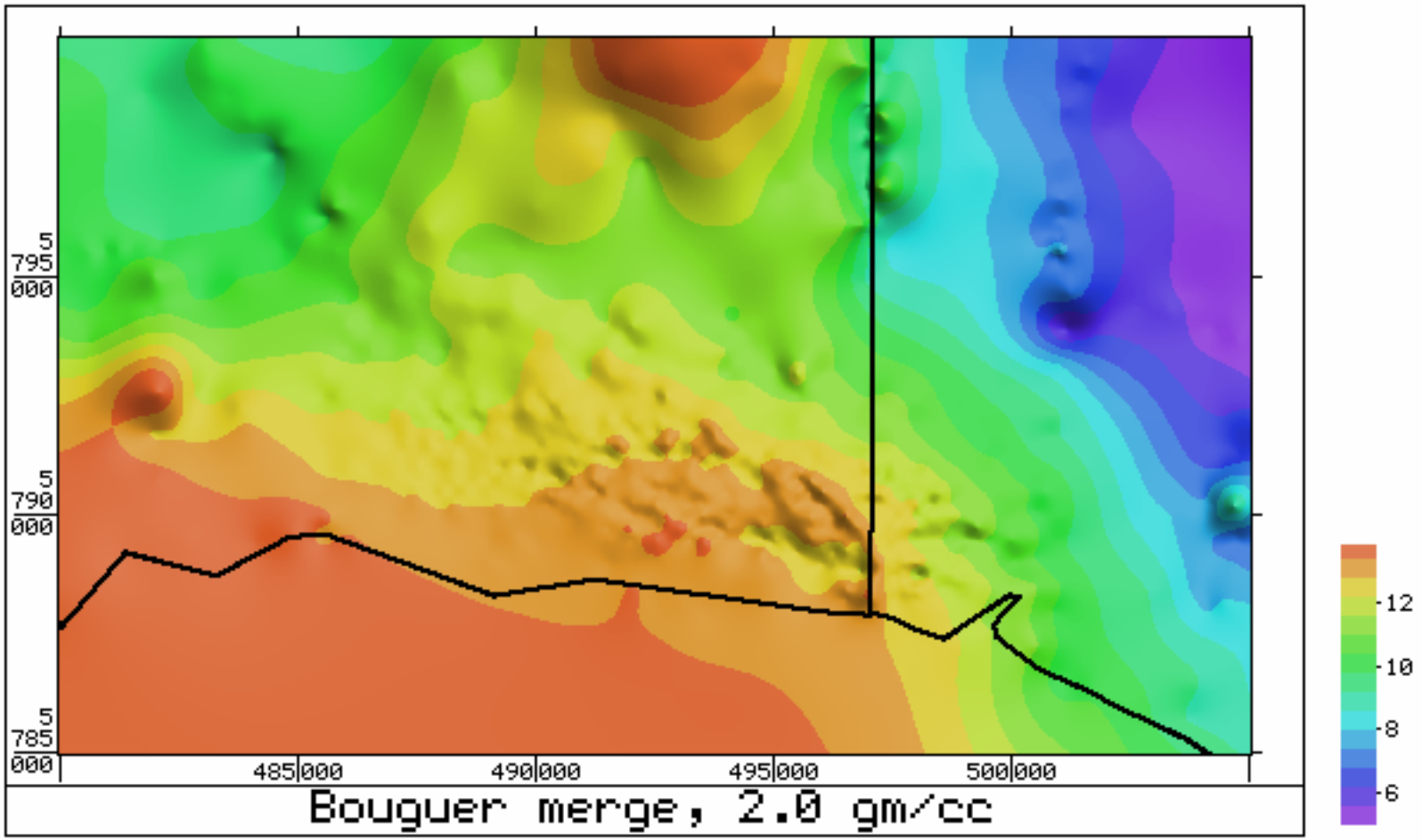

Figure 15. Merged Bouguer gravity, 2.0 gm/cc

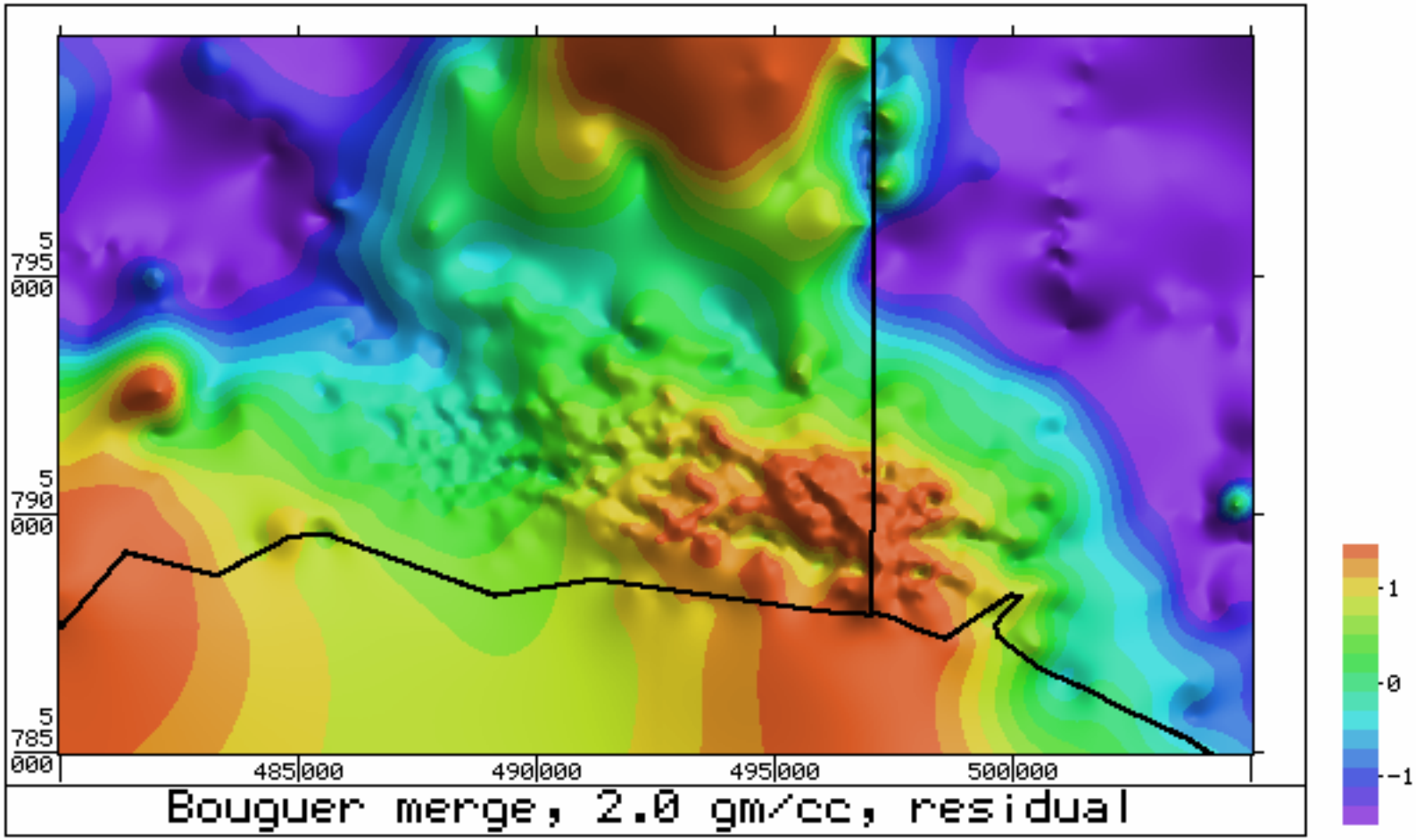

Figure 16. Merged Bouguer gravity, 2.0 gm/cc Residual, 25 km operator

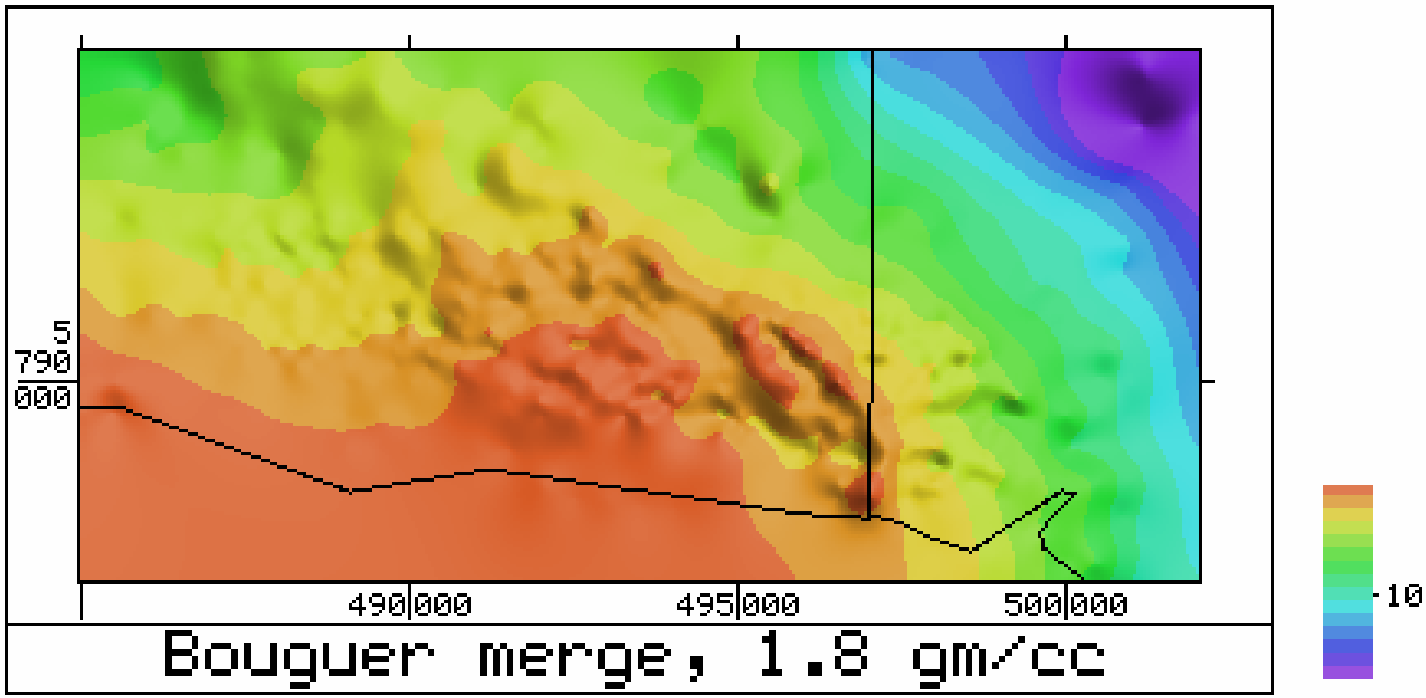

Figure 17. Bouguer gravity, 1.8 gm/cc

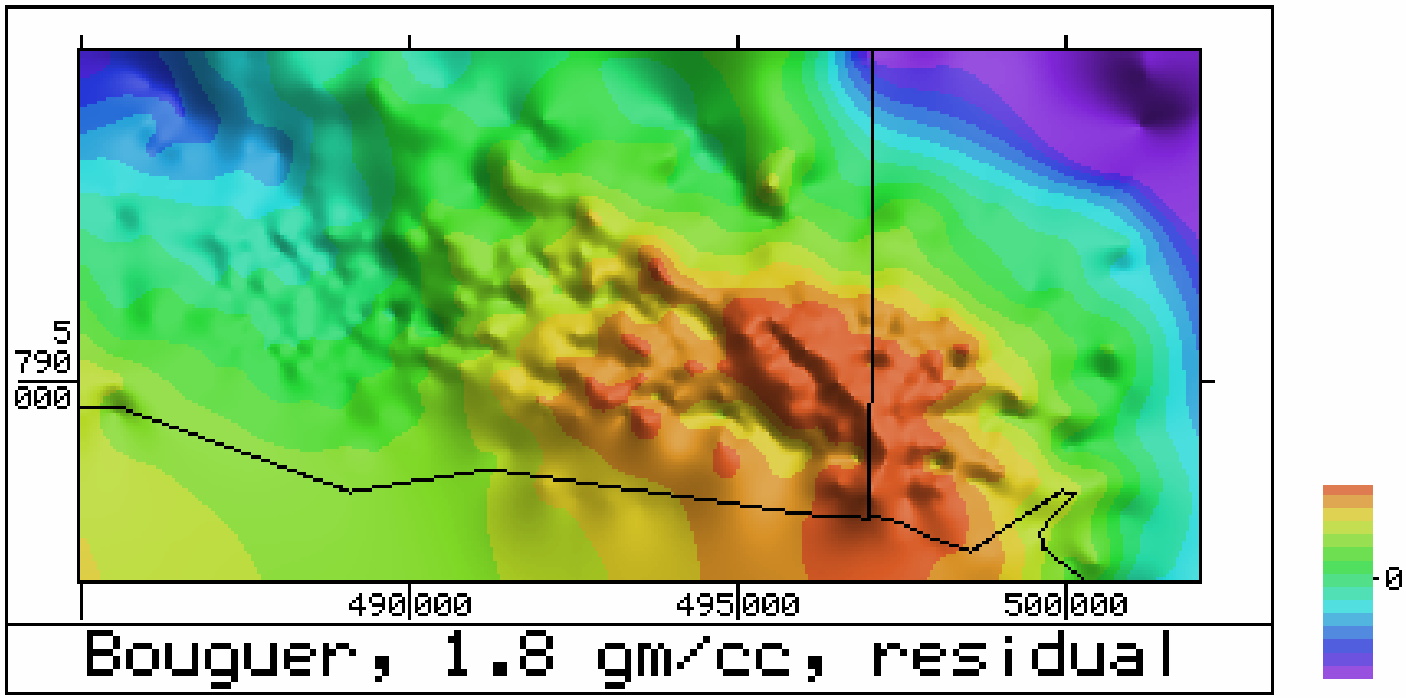

Figure 18. Residual gravity, 1.8 gm/cc
Illumination from northeast

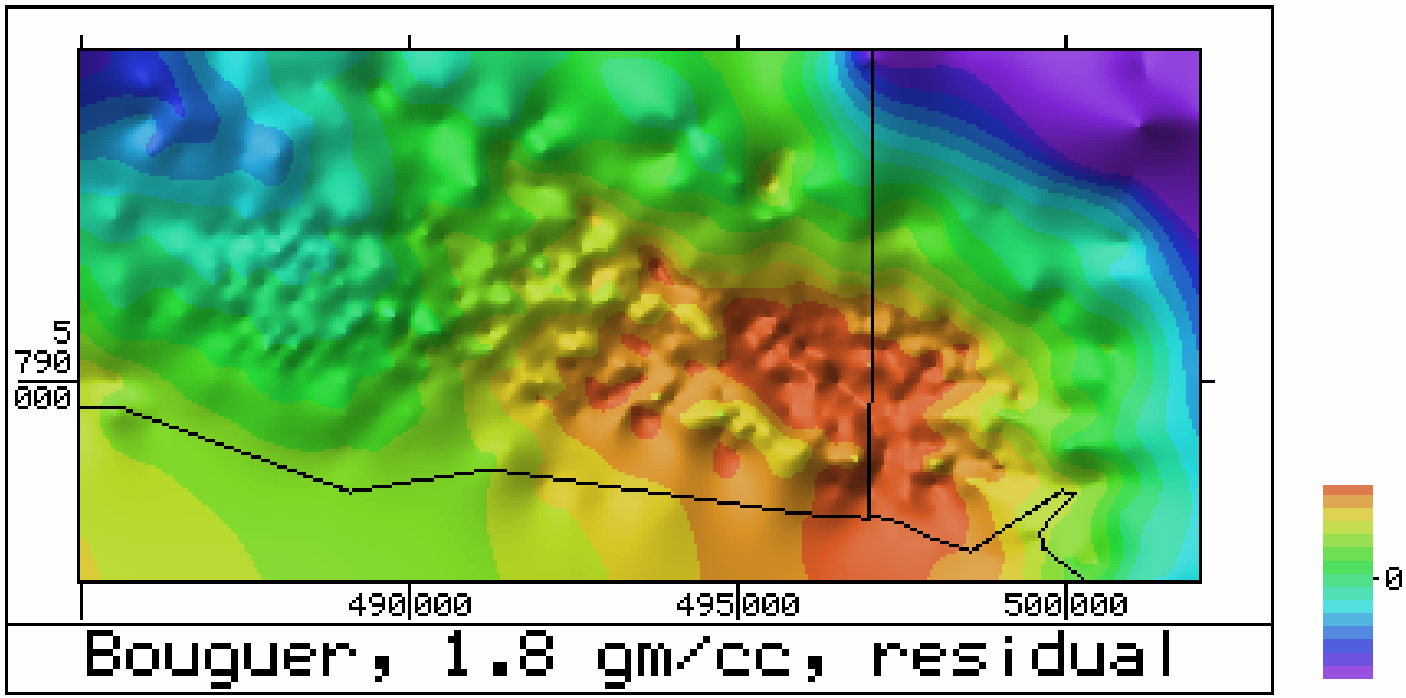

Figure 19. Residual gravity, 1.8 gm/cc
Illumination from southeast

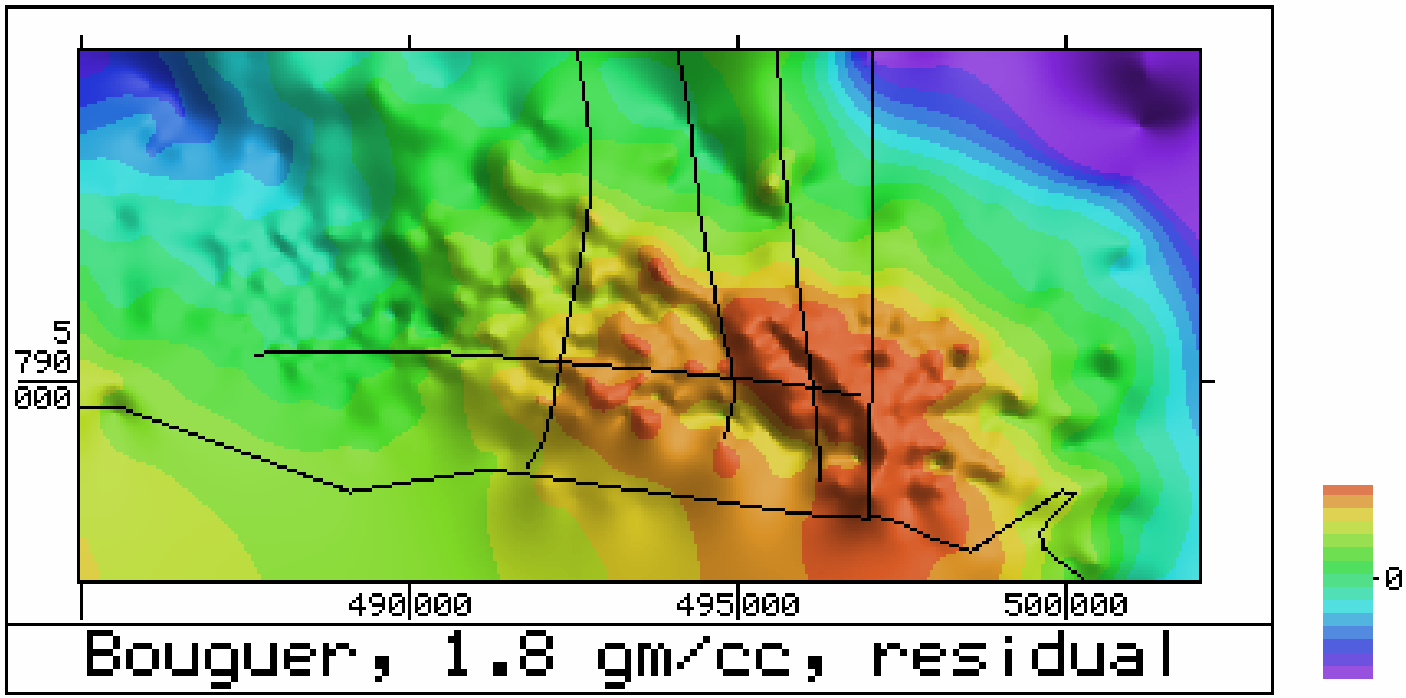

Figure 20. Residual gravity, 1.8 gm/cc
Including 4 seismic lines

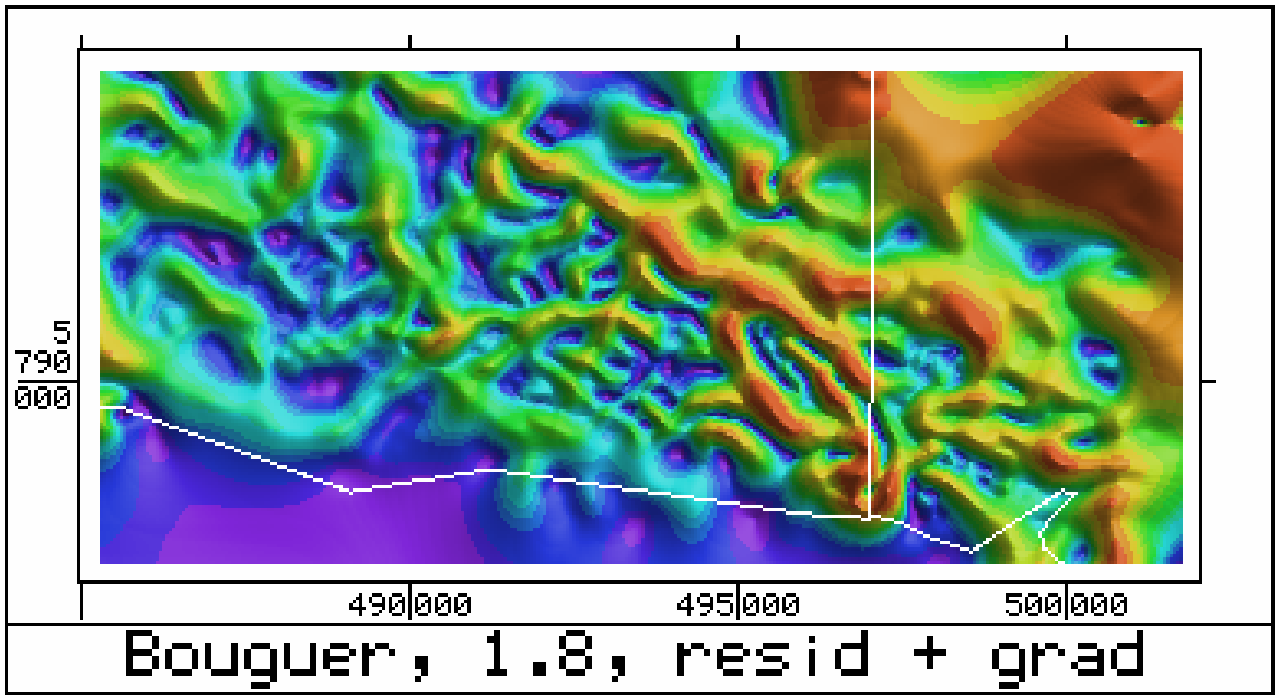

Figure 21. Horizontal gradient of residual gravity